

Lawrence Berkeley National Laboratory

Recent Work

Title

SOLUTE PARTITIONING AND MICRSTRUCTURAL DEVELOPMENT IN DUAL PHASE STEELS

Permalink

<https://escholarship.org/uc/item/6sw8z6pp>

Author

Ohmura, M.

Publication Date

1985-12-01

c.2



Lawrence Berkeley Laboratory

UNIVERSITY OF CALIFORNIA

RECEIVED
LAWRENCE
BERKELEY LABORATORY

APR 7 1986

LIBRARY AND
DOCUMENTS SECTION

Materials & Molecular Research Division

SOLUTE PARTITIONING AND MICROSTRUCTURAL
DEVELOPMENT IN DUAL PHASE STEELS

M. Ohmura
(Ph.D. Thesis)

December 1985

TWO-WEEK LOAN COPY

*This is a Library Circulating Copy
which may be borrowed for two weeks.*



LBL-20590
c.2

DISCLAIMER

This document was prepared as an account of work sponsored by the United States Government. While this document is believed to contain correct information, neither the United States Government nor any agency thereof, nor the Regents of the University of California, nor any of their employees, makes any warranty, express or implied, or assumes any legal responsibility for the accuracy, completeness, or usefulness of any information, apparatus, product, or process disclosed, or represents that its use would not infringe privately owned rights. Reference herein to any specific commercial product, process, or service by its trade name, trademark, manufacturer, or otherwise, does not necessarily constitute or imply its endorsement, recommendation, or favoring by the United States Government or any agency thereof, or the Regents of the University of California. The views and opinions of authors expressed herein do not necessarily state or reflect those of the United States Government or any agency thereof or the Regents of the University of California.

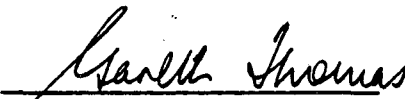
**SOLUTE PARTITIONING AND MICROSTRUCTURAL DEVELOPMENT
IN
DUAL PHASE STEELS**

**Masanori Ohmura
Ph.D. Thesis**

**Materials and Molecular Research Division
Lawrence Berkeley Laboratory
and
Department of Materials Science and Mineral Engineering
University of California
Berkeley, California 94720**

December 1985

This work was supported by the Director, Office of Energy Research, Office of Basic Energy Sciences, Division of Materials Sciences of the U.S. Department of Energy under contract number DE-AC03-76SF00098.

SOLUTE PARTITIONING AND MICROSTRUCTURAL DEVELOPMENT**IN****DUAL PHASE STEELS****Masanori Ohmura****Ph.D.****Materials Science and****Mineral Engineering****Sponsor: Nippon Kokan K. K., Japan****U. S. Department of Energy****Professor Gareth Thomas****Chairman of Committee****ABSTRACT**

A dual phase steel is one of the high strength steels characterized by a microstructure consisting of dispersed martensite in a ferrite matrix. A study of solute partitioning in a dual phase structure is of considerable importance because it controls not only the hardenability of austenite but also its growth rate during intercritical annealing. A systematic study was made of solute partitioning with particular emphasis on the relation between solute partitioning and microstructure formation for low carbon steels containing 1.5 wt% manganese, 2 wt% silicon, and 1 wt% aluminum.

Two types of heat treatments were employed to obtain dual phase structures; 1) step cooling from the austenite region, 2) reheating into the intercritical region, followed by quenching in

both cases. The volume fraction of martensite was measured as a function of intercritical annealing time. Concentration line profiles and partitioning coefficients were measured using x-ray microanalysis. These measurements enabled the effect of alloying elements and heat treatments on the growth of the transformed phase to be determined.

It was found that in the manganese steel, the growth rate of austenite in the reheating treatment was higher than that in the step cooling treatment. In the step cooling treatment, long range carbon diffusion was interrupted by the high manganese barrier, whereas in the reheating treatment, the growth of austenite was controlled by carbon diffusion in the early stage of austenite growth.

Ferrite growth in a silicon containing steel was faster than that in a manganese steel in the step cooling treatment. This fact is due to the difference of partitioning coefficients and carbon activities in austenite between silicon and manganese steels.

Finally, based on these results, optimum alloy design and heat treatments are proposed.

SOLUTE PARTITIONING AND MICROSTRUCTURAL DEVELOPMENT IN DUAL PHASE STEELS

Table of Contents		Page
1.	Introduction.....	1
1.1	Opening Remarks.....	1
1.2	Background.....	2
1.2.1	History.....	2
1.2.2	Theoretical Background of the Kinetics of Phase Transformation.....	5
1.3	Summary and Objectives.....	8
2.	Experimental Procedure.....	10
2.1	Materials.....	10
2.2	Heat Treatment.....	10
2.2.1	Reheating.....	10
2.2.2	Step Cooling.....	11
2.3	Metallography and Microscopy.....	11
2.3.1	Optical Metallography.....	11
2.3.2	Scanning Electron Microscopy.....	12
2.3.3	Transmission Electron Microscopy.....	12
2.4	Dilatometry.....	12
2.5	Analytical Electron Microscopy.....	13
2.6	Hot Stage High Voltage Electron Microscopy.....	15
3.	Results.....	17
3.1	Microstructure.....	17
3.1.1	Reheating.....	17
3.1.2	Hot Stage High Voltage Electron Microscopy.....	18
3.1.3	Step Cooling.....	19
3.1.4	Growth Rate of Transformed Phase.....	20
3.2	Isothermal Dilatometry.....	20
3.2.1	Reheating.....	21
3.2.2	Step Cooling.....	21
3.3	Partitioning.....	22
3.3.1	Line Profile.....	22
3.3.2	Partitioning Coefficient.....	24
3.3.3	Carbon Concentration Measurement.....	26
4.	Discussion.....	28
4.1	Variation of Concentration Ratio with Foil Thickness.....	28
4.2	The Correlation between Heat Treatment and Microstructure Development.....	30
4.2.1	Nucleation Stage.....	30
4.2.2	Growth Stage.....	32
4.2.3	Growth Rate of Transformed Phase.....	36
4.3	Effect of Alloying Element on Microstructure Development.....	38

4.3.1	Manganese and Silicon.....	38
4.3.2	Niobium.....	41
4.3.3	Aluminum.....	42
4.4	Summary of Microstructure Development.....	43
4.5	Optimum Alloy Design and Heat Treatment.....	44
5.	Conclusions.....	47
	Acknowledgement.....	50
	References.....	51
	Tables.....	58
	Figure Captions.....	60
	Figures.....	67

1. INTRODUCTION

1.1 Opening Remarks

Dual phase steels are an interesting, rather simple class of strong, ductile, low alloy and low carbon steels that have been developed over the last decade [1-6]. They have the attractive features of continuous yielding, high work hardening rate, high ratio of tensile to yield strength and good formability. These features indicate a great potential for cold forming applications (for example, sheets for the automobile industry).

Most of the investigations on dual phase steels have been concerned with processing, mechanical properties, and applications. The study of microstructure, morphology, and alloy design considering the favorable microstructure have not been studied extensively except in the program at U.C.B.. The recent improvements in methods of materials characterization, particularly Analytical Electron Microscopy [7,8] now allows more detailed analyses to be done of the microstructure formation.

Empirically, the properties of dual phase steels can be understood in terms of a composite of two (or more) phases, ferrite and martensite. The important parameters in controlling the properties are the volume fraction and strength of martensite, both of which are determined by the intercritical annealing temperature and the composition of the alloy; at equilibrium, these are found from the appropriate tie line construction. During intercritical annealing, alloying elements

redistribute with time to reach chemical equilibrium, and this redistribution affects not only the final hardenability of austenite in the dual phase structures, but also its growth rate during intercritical annealing. The study of partitioning of solute elements provides a useful clue to the transformation mechanism.

Hence, the current research is concerned with a detailed study of microstructure, especially as affected by solute partitioning during intercritical annealing.

1.2 Background

1.2.1 History

Two types of heat treatments have been employed to obtain dual phase structures; 1) step cooling from the austenite region, 2) reheating into the intercritical region, followed by quenching in both cases (see, Fig. 1 and Fig. 2).

1) Step Cooling

This heat treatment involves austenitizing followed by cooling to a temperature below A_{r3} . From a practical point of view, this heat treatment has been employed to produce hot rolled dual phase steels, and the processing techniques have been extensively studied [1-6].

In the fundamental aspects, there have also been a number of prior studies regarding the growth kinetics of proeutectoid ferrite. The relation between morphology and undercooling, and interface structure has been discussed by Aaronson and his

coworkers [9-13]. At small undercoolings below A_3 , ferrite nucleates on austenite grain boundaries and grows in a "blocky" manner to form grain boundary allotriomorphs. At large undercoolings, ferrite tends to grow from the grain boundaries as plates, termed Widmanstätten side-plates, which become finer with increasing undercoolings. In both cases smoothly curved, supposedly incoherent interfaces between ferrite and austenite, and faceted semicoherent interfaces exist. However, the relative rates at which semicoherent and incoherent interfaces can migrate vary with undercooling, which contribute to the different morphologies.

Aaronson and his coworkers [14-15] also studied partitioning of alloying elements between austenite and proeutectoid ferrite or bainite. However, since concentration profiles were obtained using electron microprobe analyses, the spatial resolution is too poor to perform a detailed analysis of partitioning, especially at interfaces between ferrite and austenite. The other reason that the previous results cannot be simply applied to a study of dual phase steels is that the alloy used in these studies were not representative of those of dual phase steels.

2) Reheating

This heat treatment involves reheating from the subcritical temperature (below A_{c1}) into the intercritical (ferrite and austenite) region.

Since Koo et al [16] studied partitioning in a dual phase steel by STEM-EDS (Scanning Transmission Electron Microscopy - Energy Dispersive X-ray Spectrometry), this work has become a

subject of considerable interest in recent years [17-21]. In these works, various experimental results for partitioning in dual phase structures including that by the step cooling treatment were exhibited, but the dependence of solute partitioning on the alloy composition and the intercritical annealing conditions and relation between partitioning and the kinetics of the phase transformation were not elucidated.

At the same time, the kinetics of reaustenitization during intercritical annealing has also received attention [22-28]. Speich et al. [23] discussed the microstructure formation in manganese containing dual phase steels, in which the starting microstructure was ferrite-pearlite. They concluded that austenite formation was separated into three stages: (1) very rapid growth of austenite into pearlite, (2) slower growth of austenite into ferrite controlled by carbon and manganese diffusion, (3) a very slow final equilibration stage.

Most of the researches to date concern austenite formation from a ferrite-pearlite structure, and discuss partitioning from that microstructure. Since ferrite-pearlite structures were obtained by continuous cooling from the austenite region, the substitutional elements were already partitioned to cementite in the pearlite structure. This is one of the reasons why the quantitative analyses for the results of partitioning have not been performed accurately. In order to discuss partitioning quantitatively, the preferable starting microstructure is one such as martensite in which the solute elements are homogeneously distributed within the microstructure.

1.2.2 Theoretical background of the kinetics of phase transformation

Considerable investigations have been carried out in various types of diffusion controlled phase transformations, for example, the pearlite transformation [29-33], the bainite transformation [33-35], the proeutectoid ferrite reaction [9-13, 36,37], the massive transformation [38,39], and the growth of cementite allotriomorphs [40], and have been very successful.

Local equilibrium

One of the important models is local equilibrium which applies equilibrium thermodynamics to a kinetic phenomenon. In the local equilibrium model, it is assumed that the elements of two phases in contact with each other are in chemical equilibrium at the interfaces, but the bulk composition does not attain chemical equilibrium.

Diffusion and interface controlled growth

Local equilibrium is one of the conditions which distinguishes the difference between diffusion and interface controlled growth [41, 42].

The migration rate of the interface v can be written as

$$v = M \Delta g / V_m \quad (1-1)$$

where M is the interface mobility, and Δg is the difference of chemical potential between two phases which is a positive driving force across the interface, and V_m is the molar volume of the transformed phase.

When the interface mobility M is very high, Δg can be very small. Under these conditions there is local equilibrium at the

interfaces. The interface motion is controlled by diffusion and then the growth rate can be calculated as a function of time based on the diffusion equation. On the other hand, when the interface has a lower mobility, a greater chemical potential difference Δg is required to move the interface and there is a deviation from local equilibrium conditions at the interface. In the extreme case, when the reaction step at the interface is so sluggish that the reaction does not give rise to any concentration differences, this growth condition is termed to be interface controlled growth.

In most of the cases, the interface is migrating under mixed control, and a driving force for reaction, that is, the decrease in free energy can be written as,

$$\Delta g = \Delta g^D + \Delta g^I \quad (1-2)$$

where the superscript D and I denote the diffusion and interface.

Paraequilibrium

This basic concept was proposed by Hultgren [43] and has been developed by Hillert [44], Kirkaldy [45], and Aaronson [14,15]. This model is extremely useful for ternary systems with one fast diffusing species. In this condition the substitutional elements do not contribute to the transformation except for the crystallographic change. The transformation advances only by the interstitial element diffusion, and local equilibrium of the interstitial element is attained across the interface.

Thus, in a ternary alloy such as Fe-Mn-C system, the paraequilibrium condition can be obtained as [45]

$$g_1^\alpha = g_1^\gamma \quad (1-3)$$

$$g_2^\gamma - g_2^\alpha = -(g_0^\gamma - g_0^\alpha) x_0/x_2 \quad (1-4)$$

where the superscript α and γ denote ferrite and austenite respectively, g_i is the partial molar free energy, or chemical potential of each of the three components, the subscript 0, 1, 2 denote the matrix, the interstitial solute element, and the substitutional element respectively, and x_0/x_2 is the ratio of the mole fraction between the substitutional element and the matrix.

Solute drag effect

This theory was first developed by Lücke and Detert [48] for the influence of a foreign element upon the rate of recrystallization. The Lücke-Detert theory was extended by Cahn [49] and Lücke and Stüwe [50], giving a more rigorous treatment of the diffusion of solute atoms in the potential field of a grain boundary. It was found that the drag on a grain boundary involves an impurity atmosphere which depends on the velocity of the grain boundary, the diffusivity of the impurity, and its interaction with the grain boundary. At high velocities the faster diffusing impurities have a greater drag, whereas at low velocities the slower diffusing impurities have a greater drag.

Hillert [51] also developed a similar concept based on the spike in front of the advancing interface during a phase transformation which is called the truncated spike model. This model also predicts that the free energy loss due to diffusion decreases above some critical migration rate.

Aaronson's theory is termed "Solute drag-like effect".

This has not yet been described by quantitative theory, and was evaluated experimentally only by the difference between observed kinetics and those predicted by the paraequilibrium model. When the substitutional element X reduces the activity of carbon in austenite, the driving force for growth is retarded by depressing the carbon activity in contact with the boundary. On the other hand, when X increases carbon activity, the driving force for growth will be larger, leading to an inverse "Solute drag-like effect". This effect was applied to a minimum in the parabolic rate constant for thickening at the temperature of the bay in the TTT-curve for initiation of ferrite and bainite formation in a Fe-C-Mo alloy [12].

1.3 Summary and Objectives

From the foregoing, it is clear that a study of solute partitioning in dual phase structures is of considerable importance because it controls not only the hardenability of austenite but also its growth rate and mechanism during intercritical annealing. Very little data is available in this field, and a systematic study of this subject with particular emphasis on the relation between solute partitioning and microstructure formation has not yet been made.

Regarding the theoretical work in this subject, no detailed discussion based on the transformation model described in the previous section, except the latest paper by Hillert [53] has been published.

Thus the aim of this research is:

- 1) to investigate solute atom partitioning as a function of starting microstructure, alloy composition, and intercritical annealing conditions.
- 2) to discuss microstructure formation based on the various transformation models in light of the data obtained by 1).
- 3) to present basic information for optimum alloy design and heat treatment cycles.

2. Experimental Procedures

2.1 Materials

The investigation is performed on low carbon steels, which have a wide range of the intercritical (ferrite and austenite) region. They were supplied by Nippon Kokan K. K.. They were vacuum induction melted in 150 kg ingots and cast in vacuum. They were homogenized at 1250°C for 3 hrs and hot rolled to 2.4 inch thick plates. Rectangular bar 2.4 inch wide were cut from these plates and hot forged to 0.6 inch rods. These bars were then hot rolled and cold forged into 0.3 inch rods. The chemical compositions of the 0.6 inch hot forged rods are shown in Table 1.

2.2 Heat Treatment

2.2.1 Reheating

The rods with 0.3 inch in diameter and 2.5 inch length were heat treated in a vertical tube furnace under flowing argon atmosphere. Two heat treatments were used as shown in Fig. 1. The first heat treatment involves austenitization at 1200°C for 2 hrs, followed by water quenching, which results in 100% lath martensite structure. The austenitization at high temperature was employed to reduce segregation and chemical concentration gradients that are produced by ingot solidification. The two phase annealing was done in the temperature range 730°C to 800°C

for manganese containing steels and 800°C to 930°C for silicon and aluminum containing steels. The quenching after both austenitization and intercritical annealing must be fast enough to avoid decomposition of austenite into other products (ferrite, pearlite, bainite etc.), and thus the rods were quenched into agitated iced brine, giving quench rates of more than 50°C/sec.

2.2.2 Step cooling

The rods were austenitized at 1200°C for 2 hrs, followed by cooling to the two phase regions as shown in Fig. 2. The two phase annealing was done for 10 minutes to 32 hrs at 700°C to 800°C for manganese containing steels and at 850°C for silicon containing steels. For manganese, M1, and manganese-niobium, M2, steels, isothermal holding for 30 minutes at 900°C was conducted just before the intercritical annealing in order to refine the austenite grain size.

2.3 Metallography and Microscopy

2.3.1 Optical Metallography

Specimens for optical metallography were prepared by grinding on wet silicon carbide paper up to 600 grit and polishing on 1 µm diamond paste. A 2% Nital solution was used to etch the specimen. The microstructures were observed with a Zeiss Ultraphot 2 metallograph. The volume fraction of martensite was determined by the line intercept method.

2.3.2 Scanning Electron Microscopy (SEM)

Using the same methods for sample preparation as for light microscopy, samples were examined in an ISI DS-130 scanning electron microscope operated at 20 KV.

2.3.3 Transmission Electron Microscopy (TEM)

Thin foils suitable for TEM were obtained from the same heat treated rods used for the preparation of optical metallography and scanning electron microscopy. Thin slices of about 20 mils thick were cut from the rods. The slices were then chemically thinned to about 4 mils in a solution of 5% HF in H₂O₂. Discs of 3 mm in diameter were punched from these slices, followed by grinding on wet 600 grit silicon paper. The thin discs were electropolished in a twin jet electropolishing apparatus at room temperature using a solution of 75 grams Chromium Trioxide, 400 ml Acetic Acid, and 20 ml distilled water.

Thin foils were then examined with Philips EM301 and Philips EM400 transmission electron microscopes at an accelerating voltage of 100 KV. Bright field (BF), dark field (DF), microdiffraction and x-ray energy dispersive analytical methods (see section 2.5) were utilized.

2.4 Dilatometry

A Theta Dilatronic II R dilatometer was employed to investigate the kinetics of reaustenitization and ferrite formation during the intercritical annealing. Specimens for

dilatometry were machined from the 0.3 inch diameter rods which had microstructures of lath martensite and ferrite-pearlite, giving cylindrical specimens with 0.188 inch in diameter and 0.394 inch in length.

Fig. 3 and Fig. 4 show the schematic diagrams of isothermal dilatometry in both the reheating and the step cooling treatments. The change of length during isothermal annealing can be monitored as a function of time as shown in Fig. 3(a) and Fig. 4(a). During isothermal annealing, the change of length ΔL decreases in the reheating treatment and increases in the step cooling treatment in order to reach thermal equilibrium, which was indicated by the dashed curves as shown in Fig. 3(b) and Fig. 4(b).

The specimens of lath martensite structure were heated to the intercritical region; 750°C and 800°C and isothermally annealed. The specimen for which the starting microstructure was ferrite-pearlite was austenitized at 900°C for 30 minutes, followed by cooling to the two phase temperature range of 700°C to 800°C.

2.5 Analytical Electron Microscopy

Microanalysis was accomplished using the Philips EM400 electron microscope interfaced with a Kevex 7000 system and the JEOL 200AEM electron microscope interfaced with a Kevex 8000 system. Microdiffraction was performed using the Philips EM400 electron microscope in the TEM mode.

Microanalysis was done by energy dispersive analysis (EDXS) of the X-rays generated by the interaction of the electron probe with the specimen, giving rise to through thickness composition. Line profiles of concentrations of substitutional alloying elements across the ferrite and martensite phases were measured. An electron probe of 40 nm nominal size was formed on the specimen by the condenser lens system and the spatial resolution was estimated to be 60 nm to 70 nm due to beam broadening [8]. The average concentrations of substitutional alloying elements in both ferrite and martensite regions were measured using a larger probe size, viz. 100 nm as a function of total iron x-ray counts. The foil used in this study is mostly composed of a single component, that is, iron (see Table 1) and the same electron probe diameter was employed in each measurement. Thus, the total x-ray counts can be considered to be proportional to the electron beam-specimen interaction volume. This volume, therefore, depends on the thickness when the above-mentioned conditions are satisfied. Counting times for x-ray acquisition were 300 seconds, which was determined by accounting for the statistical error in countings.

To obtain quantitative concentration profiles, analyses were performed on a thin region of a foil. However, since for some alloy systems, such as Fe-Si and Fe-Al, due to the large differences in atomic number of the components, the foil thickness satisfying the thin film criterion is less than 250 Å, for which appropriate x-ray counting with a reasonable statistical error can not be obtained (due to the small electron

beam-specimen interaction volume), the quantification for these alloy systems must require the absorption corrections. Thus in this research, for Fe-Si and Fe-Al systems, the concentration ratio between alloying elements and iron matrix was obtained at various points in the foil with the same thickness in both ferrite and martensite phases, whereas in the Fe-Mn system, the problem of thickness variation is negligible due to the small absorption effect.

The precision of the measurements was taken to be twice the standard deviation of the number of counts corresponding to the substitutional alloying elements after the background is subtracted. The error bars in Figures 20-41 correspond to this precision.

The concentration was calibrated against a standard specimen which was the fully martensitic structure in each alloy system. In the fully martensitic structures, the concentration of substitutional elements is known from the bulk composition shown in Table 1, hence the concentration of solute elements in ferrite and martensite in dual phase structures could be calibrated based on the number of x-ray counts measured from the standard (fully martensitic structure).

Since carbon is not detectable by EDXS and it is not amenable to analysis in EELS due to the contamination problem, only indirect methods are applicable for carbon measurement. Convergent Beam Electron Diffraction (CBED) was employed in attempts to determine the local carbon concentration in the martensite region by measuring the lattice parameter [54]. The

accurate measurement can be made by changes of lattice parameter with respect to a known standard with the same crystal structure. The ferrite region of the same specimen can be standard for this experiment, because the carbon content in ferrite is extremely low. The limit to the accuracy with which lattice parameter changes is considered to be 2/10,000 [7]. This method is indirect and can be compared to the lattice image method which allows estimates of composition to be made at very high spatial resolutions (<10 Å) [2]. Previous work indicates carbon level is rapidly attained to those predicted by tie line intercepts at the intercritical temperature with the A_3 temperature.

2.6 Hot stage high voltage electron microscopy

The Kratos EM1500 microscope equipped with a double tilt furnace type specimen stage was employed to study the in-situ phase transformation. Specimens from the M1 steel (see Table 1) having fully martensitic structure and prepared by the same jet polishing method described in section 2-3-3 were used. The specimens were heated by increasing a current controlled by a current stabilized power supply and cooled by reducing or switching off the heating current. Isothermal annealing at 730°C was conducted in this experiment.

3. RESULTS

3.1 Microstructure

3.1.1 Reheating

The starting microstructure of the alloy M1 before intercritical annealing is shown by the electron microscopy in Fig. 5. The microstructure is typically lath martensite with retained austenite films along the lath boundaries [2,55,56]. Fig. 6 shows a transmission electron micrograph of the alloy M1 intercritically annealed for 10 min. at 730°C. It shows highly dislocated structure with cementite particles along prior lath boundaries which is often observed in tempered martensite structures. Figures. 7-9 are SEM examples of the dual phase structures in the alloys M1, M2, and S1 intercritically annealed at 730°C (for M1 and M2) and at 850°C (for S1). These sequences of scanning electron micrographs demonstrate microstructure formation as a function of intercritical annealing time. The gray regions correspond to the martensite phase and the darker background to the ferrite phase. The feature of the microstructure is a fine fibrous distribution of extremely narrow martensite laths within prior austenite grains. The volume fraction of martensite increases with increasing the intercritical annealing time.

The microstructure intercritically annealed for 10 min. shown in Fig. 7 (a), Fig. 8 (a), and Fig. 9 (a) which correspond to the microstructure shown in Fig. 6 is a tempered martensite

structure rather than a dual phase structure, because the recrystallization of lath martensite prior to austenite nucleation is in progress.

Fig. 10 shows scanning electron micrograph of the alloy M1 intercritically annealed for 10 min. and 2 hrs at 800°C. The distinctive feature of the dual phase structure was observed even for a short intercritical annealing time, that is, 10 min. This indicates that lath martensite recrystallizes in a shorter time at a higher annealing temperature.

3.1.2 Hot stage high voltage electron microscopy

Fig. 11 reveals a sequence of transmission electron micrographs showing the microstructure change in the heating and isothermal annealing stage of the alloy M1. The heating time to reach the intercritical annealing temperature, 730°C is about 20 minutes. The fastest heating by this hot stage specimen holder was employed to simulate the actual heat treatment. The phase transformation may depend on the heating rate, because recrystallization and grain growth occur at lower temperature with decreasing the heating rate.

The starting microstructure is lath martensite as shown in Fig. 11 (a). No noticeable microstructural change was observed in the specimen at 650°C as shown in Fig. 11 (b) except that lath boundaries with narrow lath width disappear. At a higher temperature, 710°C, most of the lath boundaries disappear and each lath was gradually replaced by more equiaxed ferrite grains. Fig. 11 (d) shows the microstructure at 730°C, and Fig. 11 (e)

and (f) reveal the isothermal annealing stages for 5 min. and 60 min. The recovery and recrystallization of martensite were clearly observed and grain growth occurred in the 60 minutes isothermal annealing shown in Fig. 11 (f).

Fig. 12 (a) and (b) show the initial microstructure and microstructure intercritically annealed for 60 minutes at 730°C of the manganese-niobium containing steel. In this alloy, recrystallization of lath martensite was not observed even for the 60 minutes intercritical annealing at 730°C.

3.1.3 Step cooling

Figures 13-15 show optical micrographs of dual phase structures of the alloy M1, M2, and S1 after being intercritically annealed at 730°C (for M1 and M2) and at 850°C (for S1) in the step cooling treatment. In these optical micrographs, black areas correspond to the martensite phase and white areas to the ferrite phase. Ferrite nucleates on austenite grain boundaries and grows in a block shape typical of proeutectoid ferrite with small undercoolings below A_{r3} .

The growth rate of ferrite is strongly dependent on the alloying elements. In the silicon containing steel, ferrite grows in less than 5 minutes and the growth is saturated in 30 minutes. On the other hand, in the manganese containing steel nucleation and growth of ferrite was considerably retarded. The reaction rate of the manganese-niobium containing steel is slower than that of the plain manganese containing steel, even though the prior austenite grain size is finer, as shown in Fig.

14 and therefore has more nucleation sites for ferrite. However, niobium is known to form carbides and nitrides which pin the structure and so retards the transformation.

3.1.4 Growth rate of transformed phase

The growth rate of the transformed phase, austenite in the reheating treatment and ferrite in the step cooling treatment, was investigated by measuring the volume fraction of transformed phase as a function of intercritical annealing time as shown in Fig. 16. The following observations can be drawn from this figure.

- (1) The growth rate of transformed phase in the reheating treatment is faster than that in the step cooling treatment, especially in the early stage of the intercritical annealing.
- (2) The growth rate of transformed phase in the silicon containing steel is faster than that in the manganese containing steel in both heat treatments.
- (3) The growth rate of ferrite in the manganese-niobium containing steel, M2, is almost identical to that in the plain manganese containing steel, M1. However, the incubation time to form ferrite is longer in alloy M2 than that in alloy M1.

3.2 Isothermal Dilatometry

3.2.1 Reheating

Isothermal dilatometry was employed at 750°C and 800°C for the manganese containing steel, M1, as shown in Fig. 17. In both cases, the transformations were characterized by a rapid initial reaction followed by a much slower reaction. The rate of length change increases with increasing the intercritical annealing temperature, which indicates as expected that the growth rate of austenite increases with increasing the annealing temperature.

3.2.2 Step cooling

The isothermal dilatation curves for the manganese steel intercritically annealed for 700°C, 730°C, and 800°C in the step cooling treatment are shown Fig. 18. These temperature and dilatation curves have different features from those in the reheating treatment.

- (1) The isothermal dilatation curves can be approximately expressed by a single equation.
- (2) The rates of length change increase with decreasing the intercritical annealing temperature, which is opposite to that in the reheating treatment.

These tendencies suggest that different transformation mechanisms are working in each case, that is, the austenite growth in the reheating treatment and the ferrite growth in the step cooling treatment.

3.3 Partitioning

Figures 19 (a), (b), and (c) show TEM micrographs of the dual phase structures intercritically annealed for 2 hrs at 800°C for the alloy M1, and at 850°C for the alloy S1 and A in the reheating treatment. Figures 19 (d) and (e) show dual phase structures of the alloy M1 and S1 intercritically annealed for 2 hrs at 730°C and 850°C in the step cooling treatment.

For these specimens, two different methods were employed to study partitioning of the substitutional alloying elements.

- (1) to measure line concentration profiles across ferrite and martensite in order to discuss the interface migration mechanism.
- (2) to measure solute element concentration in both martensite and ferrite by a relatively large probe size in order to obtain the ratio of solute element concentrations between ferrite and martensite.

3.3.1 Line profiles

(a) Reheating

Concentration profiles of manganese and silicon were measured as a function of intercritical annealing temperature and time. The profiles shown in Fig. 20 and Fig. 21 were obtained for the alloy M1 intercritically annealed at 730°C for 2 hrs and 32 hrs. Figures 22-24 show the profiles for the same alloy intercritically annealed at 800°C for 10 min., 2 hrs, and 32 hrs. These manganese profiles were characterized by a flat shape in

the ferrite phase and a shallow spike shape in the martensite phase. With increasing intercritical annealing time, the average manganese concentration increases in martensite and decreases in ferrite, which suggests that partitioning is more pronounced with increasing intercritical annealing time.

A similar concentration profile measurement was employed for the alloy M2 intercritically annealed for 2 hrs at 800°C as shown in Fig. 25. In this intercritical annealing condition, less partitioning of manganese in austenite was observed than that found in the alloy M1.

Figures 26 and 27 show silicon concentration profiles for the alloy S1 intercritically annealed at 850°C for 30 min. and 32 hrs. The feature of this composition profile is that there is more partitioning of silicon in the ferrite phase and it has flat shapes in both ferrite and martensite phases. This indicates that the equilibrium state may be attained in less than 30 min..

(b) Step cooling

The manganese concentration profile of the alloy M1 intercritically annealed for 2 hrs at 730°C in the step cooling treatment is shown in Fig. 28. There is a slight tendency for interface segregation to occur between ferrite and martensite. The actual manganese concentration at the interface may be higher because the spatial resolution is not adequate to measure interface segregation directly due to beam broadening in the foil [8].

Fig. 29 shows a concentration profile of the same alloy intercritically annealed at 730°C for 32 hrs. This profile

reveals a remarkable spike shape in martensite (prior austenite) adjacent to the interface. The concentration of manganese in the ferrite region and the austenite region a little away from the interface is almost unaltered from that in the initial bulk alloy.

The manganese concentration profile of the alloy M2 intercritically annealed for 2 hrs at 730°C was determined as shown in Fig. 30. A similar tendency to that found in Fig. 28 was observed, implying that manganese segregation occurs at the interface.

A silicon concentration profile of the alloy S1 intercritically annealed for 2 hrs at 850°C was measured across the interface between ferrite and martensite phase as shown in Fig. 31. The silicon concentration remained constant except that there was a very slight, but noticeable spike effect at the interface.

3.3.2 Partitioning coefficient

In EDS measurements, the concentration of substitutional alloying elements depends on thickness of a foil due to the mass absorption and the fluorescence effects [8].

Figures 32-41 show the variation of the x-ray intensity ratios between substitutional alloying element and iron with total Fe x-ray counts. The total Fe x-ray counts approximately correspond to the foil thickness as described in the previous section. The intensity ratio between manganese and iron is independent of the total x-ray counts as shown in Fig. 32, while

those of silicon and aluminum are strongly dependent on the total Fe x-ray counts as can be seen from Figures 33-41. These features were attributed to the absorption effect of silicon and aluminum x-rays in the iron matrix.

The partitioning coefficient was defined as the ratio of x-ray intensities of the substitutional alloying elements between martensite and ferrite. These ratios were calculated from the experimental results obtained in the range of Fe x-ray counts 500 to 1500 cts/sec.

In Fig. 42, the relation between partitioning coefficients of manganese and silicon and intercritical annealing times is shown. The intercritical annealing temperatures are 730°C and 800°C for the alloy M1 and 850°C for the alloy S1. The partitioning coefficient of manganese at 730°C in the equilibrium obtained from the tie line construction in the ternary phase diagram [47] was indicated as "x" in the top right corner of this figure. The partitioning coefficients of manganese increase with increasing the intercritical annealing time, whereas that of silicon remains constant in the range of 30 min. to 32 hrs.

A similar tendency was found in the relation between partitioning coefficients and intercritical annealing temperature as shown Fig. 43. In the manganese containing alloy, M1, the partitioning coefficient decreases with increasing the intercritical annealing temperature, while in the silicon and aluminum steels the dependence of partitioning coefficients on the intercritical annealing temperature is not significantly strong.

Fig. 44 shows the variation of partitioning coefficients with the bulk carbon contents of silicon containing steels. It was found that partitioning coefficients are more dependent on the intercritical annealing temperature than the carbon contents of these steels.

3.3.3 Carbon concentration measurement

Measurements of carbon concentration in the martensite phase was attempted by the Convergent Beam Electron Diffraction method. Since carbon concentration is measured by the shift of the holz line from that in the standard material which is caused by the changes in the lattice parameter, the holz line must be as sharp as possible. The (210) orientation was chosen because this allows the fine structure of holz lines to be obtained [57]. Fig. 45 (a) and (b) show the zero order Laue zone around zero order disc in the (210) orientation of the ferrite and the martensite region. The holz lines were clearly resolved in the ferrite phase but not in the martensite phase. As is known, and as can be seen from Fig. 5, martensite is highly distorted due to the high dislocation density resulting from the shear transformation from austenite. Even though the beam probe size was 200 Å, the holz lines are too diffuse to permit measurement. Thus CBED is not very promising for carbon analysis. As was discussed earlier, carbon is not detected spectroscopically by EDXS analysis nor by EELS. However previous work by Koo et al. [2] using high resolution lattice imaging showed that the carbon values quickly reached equilibrium levels. Thus, for the

temperature and alloys used, the expected carbon levels are as follows [46].

	730°C	800°C
paraequilibrium	0.58 wt%	0.23 wt%
full equilibrium	0.52 wt%	0.21 wt%

4. DISCUSSION

4.1 Variation of the Concentration Ratio with Foil Thickness

The concentration of each element is generally assumed to be constant throughout the thin foil, and so absorption can be neglected. However, this approximation is only valid under certain conditions, for example, "the thin film criterion" [58]. As shown from Figures 33-41, the x-ray intensity ratio between substitutional elements, i.e. silicon and aluminum, and iron was substantially dependent on the total iron x-ray counts which correspond to the thickness of the foil. On the other hand, the x-ray intensity ratio between manganese and iron does not depend on foil thickness as seen from Fig. 32.

The absorption limitation of "the thin film criterion" has been considered by Tixer and Philibert [58]. They proposed that if

$$C_A \csc \theta \rho t < 0.1 \quad (4-1)$$

where C_A = mass absorption coefficient.

θ = the take off angle between the specimen and x-ray detector.

ρ = the density of the element in the foil.

t = the thickness of the foil.

is satisfied, no absorption correction is necessary.

The critical thickness for Fe-Mn, Fe-Si, and Fe-Al can be calculated from Eq. (4-1). The mass absorption coefficients of iron are shown in Fig. 46 [59, 60].

For Fe-Mn system, $t < 7950 \text{ \AA}$

For Fe-Si system, $t < 254 \text{ \AA}$

For Fe-Al system, $t < 165 \text{ \AA}$

In general, x-ray measurements are performed for foil thicknesses in the range of 500 \AA to 1500 \AA in order to account for statistical errors in counting. Hence, the absorption correction is necessary except for the Fe-Mn system, which is consistent with the experimental results.

Another requirement is the fluorescence correction. This occurs when the absorption edge for the appropriate x-ray from element A must be just below the x-ray energy from matrix element B. Since the wavelength of Fe- K_{α} is 1.94 \AA and the absorption edges for Mn- K_{α} , Si- K_{α} , and Al- K_{α} are about 1.8 \AA , 6.5 \AA , and 7.5 \AA , this effect can be neglected.

As can be seen from Figures 33-41, the dependence of x-ray intensity ratio on thickness in the Fe-Si system is more significant than that in the Fe-Al system. This cannot be explained only by the absorption correction, because the mass absorption coefficient in the Fe-Si system is smaller than that in the Fe-Al system. A plausible explanation is due to artefacts from the specimen preparation procedures. Fig. 47 shows the EDS spectra taken from an aluminum containing steel with a dual phase structure which was prepared by electropolishing at the same time as a silicon containing steel was prepared. A silicon x-ray spectrum was observed even though no silicon was contained in this alloy. This shows that silicon is easily redeposited on the foil surface during

electropolishing. This could account for the fact that the silicon concentration is higher in the thin range of foil thickness than that corrected by the absorption effect.

4.2 The Correlation between Heat Treatment and Microstructure Development

In this section, the correlation between heat treatment and microstructure formation will be discussed only for the manganese steel. The effect of alloying elements will be discussed in the next section.

4.2.1 Nucleation stage

A significant amount of research has been done on the tempering process of martensite in various steels and this is one of the oldest and most popular topics to be reported [61-62]. However, most of the investigations are concerned with tempering below A_{c1} temperature and very little data on the tempering, recrystallization, and austenite formation at higher tempering temperatures are available. Austenite growth from lath martensite is one of the tempering processes of martensite.

When the specimen with lath martensite structure was heated to the intercritical (ferrite and austenite) annealing region, several stages were observed.

- (1) Recrystallization starts at lath boundaries.
- (2) Cementite precipitates along lath boundaries which can be considered to result from the decomposition of the retained austenite films.

(3) Recrystallization is completed associated with grain growth of ferrite.

(4) Austenite nucleates and grows.

The nucleation of austenite was not directly observed by hot stage experiment due to the rapid reaction. However, it is speculated that the nucleation sites of austenite were cementite particles, suggesting a high carbon content in the nuclei of austenite; such high carbon contents have in fact been measured by Sarikaya et al. [54]. The hypothesis is confirmed by the experimental result that the cementite particles precipitated along lath boundaries and austenite nucleated in the same direction. In addition, based on the previous work [54] it can be suggested that the concentration of manganese in the austenite adjacent to the interface may be low.

It should be noted that there may be another mechanism of austenite growth, although this was not observed in the present study. The retained austenite films could grow without decomposing to bainitic ferrite and cementite, especially if rapid heating is employed. However, even though this mechanism works, the above-mentioned statement that the carbon concentration of austenite in the early stages of intercritical annealing is high is not invalidated.

In the step cooling treatment, the nucleation of ferrite from austenite is that of proeutectoid ferrite formation at small undercoolings. As can be seen from Figures 13 and 14, the nucleation sites are prior austenite grain boundaries. Precipitation occurs as grain-boundary allotriomorphs. The

carbon concentration data for proeutectoid ferrite and austenite is not available because of the difficulty of carbon measurement in extremely small region. However, it can be considered that the carbon content in the austenite may be the same as that in the bulk material in the early stage of ferrite formation because of the high diffusivity of carbon, and the small volume fraction of ferrite. This hypothesis suggests that the concentration of manganese in the austenite adjacent to the interface is high, assuming equilibrium conditions at the interface. This is confirmed by present experimental result as shown in Fig. 28 and Fig. 29.

4.2.2 Growth stage

(a) Reheating

As Speich et al. [23] discussed for austenite formation in which the starting microstructure is ferrite-pearlite, in the early stage, growth of austenite is controlled by carbon diffusion due to the low diffusivity of substitutional alloying elements. This is the case to which the paraequilibrium model can be applied. The manganese concentration profile for 10 min. at 800°C shown in Fig. 22, indicates no significant manganese partitioning between ferrite and martensite, and this is consistent with this concept. In the later stage, growth of austenite is controlled by both substitutional alloying elements and carbon.

In general, the reaction rate depends on the nucleation rate, growth rate, the density and distribution of nucleation sites,

the overlap of diffusion fields from adjacent transformed volumes, and impingement of adjacent transformed volumes. In the reheating treatment, the reaction rate depends on the number of nucleation sites and the growth rates; in the step cooling treatment, the reaction rate depends on the nucleation rate and growth rate.

One of the transformation models which can be applied in this reheating treatment is that of diffusion controlled growth, with attaining local equilibrium at the interface. The following conditions of manganese diffusion must be satisfied.

(1) Local equilibrium condition:

Since under this condition the chemical potential in the two phases is equal for each element, the concentration of the substitutional element at the interface between ferrite and austenite can be determined by the tie line construction of the ternary phase diagram as shown in figures 48 and 49 [46,64,65].

(2) Diffusion equation:

In both austenite and ferrite the concentration of manganese satisfies the one dimensional diffusion equation.

$$\frac{\partial C}{\partial t} = \frac{\partial}{\partial x} (D \frac{\partial C}{\partial x}) \quad (4-2)$$

where C is the concentration of manganese, D is the diffusivity of manganese, and x is the distance.

The initial condition is given by

$$C(x, 0) = C_0$$

and the boundary conditions based on the local equilibrium are given by

$$C^a(X(t), t) = C^a_E$$

$$C^f(X(t), t) = C_E^f$$

where $X(t)$ is the interface position, and a , f , and E denote austenite, ferrite, and equilibrium, respectively.

(3) A mass balance condition:

A mass balance condition can be obtained from

$$\int_{x=-d^a/2}^{X(t)} (C^a(x) - C_o) dx = \int_{X(t)}^{x=d^f/2} (C_o - C^f(x)) dx \quad (4-3)$$

where d^a and d^f are the width of austenite and ferrite phase.

The diffusion equation which satisfies both the mass balance and local equilibrium conditions cannot be solved. Since the mass balance condition must be required, the local equilibrium condition is not fulfilled if these diffusion equations are applied for both ferrite and austenite phases. However, if the equilibrium condition at the interface is assumed only in the austenite phase, then the concentration can be obtained as

$$C(x,t) = C_o + (C_E^a - C_o) \times \operatorname{erfc}(x/2\sqrt{Dt}) / \operatorname{erfc}(X(t)/2\sqrt{Dt}) \quad (4-4)$$

Fig. 50 shows the calculated concentration profiles in which the intercritical annealing conditions are chosen as 730°C for 2 hrs and 32 hrs and 800°C for 2 hrs. Solid lines show calculated concentration profiles when the interface is static, that is, $X(t)=0$, and dashed lines are calculated concentration profiles when the interface is moving; here the initial interface width

was assumed to be half of the final width. This result indicates that when the interface migration rate is higher and the concentration at the interface is higher, such as in the case of the 730°C for 2 hrs treatment, the concentration profile in a static boundary is likely to deviate more from that in a moving boundary. Consequently, it can be suggested that the local equilibrium at the interface is attained when the interface migration rate is slow and the concentration at the interface is low.

In Fig. 51, the calculated concentration profiles in a static boundary and a moving boundary are plotted with the actual concentration profiles already shown in Figures 20-24. Considering the interface migration rate in this study, the condition of a moving interface was approximately followed by Fig. 50 (a) in the case of the 730°C intercritical annealing and Fig. 50 (c) in the case of the 800°C intercritical annealing. The calculated concentration profile at 800°C for 2 hrs is in good agreement with the experimental profile. This fact is consistent with the previous discussion about the limitation of the local equilibrium model in a moving interface.

(b) Step cooling

In the early stage of ferrite formation manganese segregation at the interface is too localized to be detected as demonstrated in Fig. 28. The phenomenon of sluggish ferrite growth can be explained by interface controlled growth such that only short range order diffusion occurs across the interface.

Carbon diffusion in the long range order may be interrupted by the highly localized manganese barrier.

In general, the Avrami rate equation can be written as

$$f = 1 - \exp(-kt^n) \quad (4-5)$$

where f is a unit volume of transformed phase, k is the rate constant which depends on the nucleation and growth rate, and n is a numerical exponent whose value can vary from 0.5 to 4.

Fig. 52 shows the calculated growth curves based on equation (4-5) as a function of n and the experimental curve at 700°C. The calculated dilatation curve for the case that n equals unity is in good agreement with the experimental dilatation curve. This is the case for grain boundary nucleation after site saturation in interface controlled growth [42]. The interpretation for ferrite growth in the early stage is consistent with the previous discussion that carbon diffusion occurs only over a short range near the interface due to the high manganese barrier.

In the later stage of intercritical annealing, the growth rate of ferrite decreases with annealing time. This stage may be growth of ferrite with impingement after the nucleation stage was completed. The width of the spike in Fig. 29 is consistent with the calculated value based on the diffusion equation.

$$\sqrt{Dt} = \sqrt{4.7 \times 10^{-15} \times 32 \times 3600} = 2300 \text{ \AA}$$

This indicates that manganese diffusion controls the rate of the phase transformation in this stage.

4.2.3 The growth rate of the transformed phase

The nucleation and growth models have been discussed, but

the difference between the growth rate for reheating and step cooling treatments has not been elucidated. These transformation steps are summarized in Fig. 53 and Fig. 54. Since the growth rate is different especially in the early stage of intercritical annealing of the manganese containing steel, the distinctive mechanism is attributed to the nucleation stage.

As discussed in the previous section, the sluggish growth of ferrite is considered to result from a high manganese interfacial barrier. This can be explained quantitatively by the solute drag effect. The solute drag effect is strongly dependent on the concentration of the segregated atoms. The total drag force exerted by all the segregated atoms on the grain boundary is given by [49].

$$P_d = -N_v \int_{-\infty}^{\infty} (C - C_0) dE/dx dx \quad (4-6)$$

where N_v is the number of atoms per unit volume, C_0 is the bulk concentration, C is the concentration of segregated atoms, and E is the interaction energy between solute atoms and the grain boundary. Since the concentration of the segregated atoms is substantially localized, Eq. (4-6) can be rewritten as

$$P_d = -N_v [C(0) - C_0] E'(0) \quad (4-7)$$

where $E'(0)$ is the derivative of the interaction energy at the interface. This indicates that the interface migration rate decreases with increasing concentration of substitutional alloying element at the interface due to the drag force.

On the other hand, in the early stage of the reheating

treatment, the manganese concentration of austenite is low because of the high carbon content in austenite nuclei. This leads to a high growth rate of austenite due to the low manganese barrier.

Another possible idea, which may account for this difference is the concept of diffusion and interface controlled growth. This model, which is generally applied for a binary system, such as Fe-C, Fe-Ni [63] can be modified, considering carbon as the diffusion species. As already discussed in the previous section, in the step cooling treatment, long range carbon diffusion was interrupted by a high manganese barrier at the austenite and ferrite interface. Hence, this situation must be interface controlled growth. In the reheating treatment, carbon diffusion controls the growth of austenite, in which paraequilibrium condition was attained.

4.3 Effect of Alloying Elements on Microstructure Development

4.3.1 Effect of manganese and silicon

(a) Reheating

As discussed in the previous section, growth of austenite in the later stage was controlled by substitutional alloying element diffusion. A schematic drawing of austenite formation is shown in Fig. 53. The reason why the growth rate of austenite in a silicon containing steel is higher than that in a manganese steel can be explained by the fact that the diffusivity of silicon in iron is two orders of magnitude larger than that of manganese.

The nucleation rate of austenite in the silicon containing steel is also higher than that in the manganese containing steel as can be seen in Fig. 16. The effect of alloying elements on the tempering of as-quenched martensite has been extensively studied [62,63]. It is known that the tetragonality of martensite disappears by 300°C in plain carbon steels, whereas in steels containing some alloying elements, such as Cr, Mo, W, V, Ti, Si, the tetragonal lattice is still observed after tempering at 450°C and even as high as 500°C. This fact indicates that these alloying elements increase the stability of the supersaturated iron-carbon solid solution. On the other hand, manganese and nickel decrease this stability. Manganese is a weak carbide former, found in solid solution in cementite as the form of $(Fe\ Mn)_3C$ which has more stabilization than cementite, whereas silicon has a very low solubility in cementite. These distinctive features leads to different rates of austenite formation. In the silicon containing steel, recrystallization of martensite may be more sluggish, but austenite formation from cementite is faster than that of the manganese containing steel. Thus, a higher growth rate of austenite can be attained.

(b) Step cooling

In the step cooling treatment, the growth rate of ferrite in the manganese containing steel is slower than that in the silicon containing steel as shown in Fig. 16. This experimental result can be qualitatively explained by the solute drag-like effect proposed by Aaronson [12]. Since manganese reduces the carbon

activity in austenite, the driving force for the ferrite growth is retarded by depressing the carbon activity at the interface [64]. On the other hand, since silicon increases the carbon activity in austenite, the driving force for ferrite growth is larger [66]. Table 2 shows the influence of manganese, silicon, and aluminum on carbon activity [64, 66, 74, 75].

A general quantitative formula regarding the calculation of the carbon activity was derived by Hillert [67], assuming that the growing A phase inherits the initial alloy content of the B phase u_M .

$$\ln (a_c / a_c^0) = (1-K_M) u_M / (u_c^B - u_c^A) \quad (4-8)$$

where a_c = the carbon activity at an arbitrary point on the phase boundary.

a_c^0 = the carbon activity of the unique A+B equilibrium in the binary Fe-C system.

K_M = the distribution coefficient of M between the B and A phases, i.e. the partitioning coefficient in this study.

$$u_c^A = x_c^A / (1-x_c^A)$$

$$u_c^B = x_c^B / (1-x_c^B)$$

where x_c^A and x_c^B are usual carbon mole fraction of the A and B phases.

In the step cooling treatment, A and B phases correspond to ferrite and austenite (martensite), resulting in u_c^B being larger than u_c^A . In a manganese containing steel, the partitioning

coefficient of manganese is more than unity which corresponds to $K_M > 1$. From Eq. (4-8), when K_M is more than unity, we can obtain

$$\ln(a_C/a_C^0) < 0$$

This result suggests a decrease of carbon activity. The same discussion can be applied for a silicon containing steel and the calculated result, that is, $a_C > a_C^0$ can be obtained. These values are consistent with the above mentioned solute drag-like effect.

The other fact which supports the difference in ferrite growth rates between manganese and silicon containing steels is the magnitude of the partitioning coefficient shown in Fig. 42. As can be seen from Eq. (4-7), a larger concentration difference at the interface between ferrite and martensite is attributed to a larger solute drag effect, which leads to the slower growth rate of ferrite in the manganese steel.

In the previous discussion, the comparison of the ferrite growth rate was presented between the silicon steel at 850°C and the manganese steel at 730°C. These intercritical annealing temperatures were chosen to yield the same amount of undercooling for these steels, because the amount of undercooling is more sensitive to the phase transformation than the actual annealing temperature. However, the effect of the intercritical annealing temperature on the growth rate of ferrite must be discussed. According to the TTT diagram of the alloys with similar alloy composition [68,69], the growth rate of ferrite in a silicon steel is faster at 730°C than that at 850°C. This indicates that the difference of the growth rate of ferrite

between silicon and manganese steels becomes more pronounced at the same intercritical annealing temperature, 730°C.

4.3.2 Effect of niobium

In recent years a niobium microalloyed dual phase steel has attracted attention, because this alloy exhibits the variation of strength with volume fraction of martensite [70-72].

In this research the following features of microstructure formation of a niobium-manganese containing steel were obtained .

- (1) Recrystallization of lath martensite is retarded.
- (2) The ferrite growth rate of this alloy is slower than that in the plain manganese alloy.
- (3) Partitioning of manganese is less significant than that in the plain manganese alloy.

The effect of alloying elements on tempering of martensite has been extensively investigated [62,63]. It was demonstrated that alloying elements have a substantial effect in lowering M_s temperature and affect the kinetics of the basic reactions and the products of the reactions, for example, alloy carbides replace cementite. The carbide former elements, such as V, Ti, Mo, Nb, tend to decrease the carbon activity, resulting in inhibiting long range carbon diffusion. It can be suggested that retardation of recrystallization of martensite is attributed to the stability of niobium carbide and its pinning the substructure and grain boundaries.

The second and third features of microstructure formation indicates that the interface motion was changed by adding

niobium. It can be explained that the precipitate particles, i.e. NbC, pin the ferrite/austenite interface [73].

4.3.3 Effect of aluminium

No significant distinction of phase transformation between the silicon and aluminum containing steels was noted except that there is a slight difference in the dependence of partitioning coefficients on the annealing temperature. This is consistent with the similarity of the ternary phase diagrams between Fe-Si-C and Fe-Al-C [74]. However, as shown in Table 2, the influence of carbon activity in austenite and ferrite is different [75,76]. Silicon increases the carbon activity of austenite, while aluminum decreases it. It may be that a different transformation mechanism works in the step cooling treatment. However, this was not studied in this research.

4.4 Summary of Microstructure Development

In this section, a summary of the heat treatments and alloying elements on microstructure development is given.

Fig. 53 shows a schematic diagram of microstructure development in Fe-Mn-C and Fe-Si-C systems in the reheating treatment. The starting microstructure before the intercritical annealing is lath martensite with retained austenite films along the lath boundaries. In the early stage of intercritical annealing, recrystallization starts at the lath boundaries and cementite precipitates along the lath boundaries

where the carbon is concentrated. Subsequently, austenite nucleation occurs on the carbide. During the intermediate stage, austenite growth occurs simultaneously with the grain growth of ferrite, as can be seen in the in-situ HVEM results. The austenite in these stage is clearly controlled by carbon diffusion for which paraequilibrium model can be applied. In the final stage, the growth of austenite is controlled by substitutional alloying element diffusion to reach chemical equilibrium. In the Fe-Si-C system, the final equilibrium can be attained in a shorter time than that in the Fe-Mn-C system due to the higher diffusivity of silicon than manganese in the iron matrix.

Fig. 54 shows a schematic diagram of the microstructure development in the Fe-Mn-C and the Fe-Si-C systems in the step cooling treatment. In this treatment, the formation of ferrite occurs by proeutectoid decomposition at small undercoolings. The growth of ferrite is controlled by both carbon and substitutional alloying element diffusion which can be classified by an interface controlled growth model. In the Fe-Mn-C system, interface controlled growth dominates and this is attributed to the high manganese barrier at the interface between ferrite and austenite.

4.5 Optimum Alloy Design and Heat Treatment

It was known that a silicon containing steel has a better combination of strength and elongation than that in a manganese

containing steel [77-80]. From this work, one of the reasons for this fact can be derived. In experimental results of substitutional alloying element partitioning, it was found that manganese partitions more in the austenite region, especially adjacent to the interface, than that in the ferrite region, whereas silicon partitions more in the ferrite region than that in the austenite region. Some of the research to date has been concerned with the difference of hardness between ferrite and martensite and discussed the relation between mechanical properties and the hardness of each phase [79]. However, in the aspect of microscopic fracture mechanics, the hardness near the interface is more considerable than the average hardness of each phase. In the manganese containing steel, the hardness of martensite adjacent to the interface is enhanced due to the highly segregated manganese elements while that of ferrite is reduced. This may induce microcracks at the interface between ferrite and martensite at a relatively lower strain in the manganese steel. However, the silicon steel shows an opposite tendency to that of the manganese steel; the difference of the hardness between ferrite and martensite is much lower. Therefore, it can be suggested that a silicon containing steel has a better strength-elongation combination.

Nevertheless, silicon increases the A_{c1} temperature and this is not favorable in the aspect of energy cost of in the reheating treatment. Consequently, alloying elements which decreases A_{c1} temperature, such as manganese, is indispensable in this alloy to reduce the total processing cost. In addition, another

favorable feature of manganese is to increase the hardenability of austenite.

One of the heat treatments suggested based on this work is rapid heating, because it increases the nucleation sites of austenite which is attributed to shorten the diffusion path of manganese in austenite, resulting in increasing hardenability of austenite.

In the step cooling treatment, the following points are considered to obtain the dual phase structure most effectively.

- (1) Flexibility in heat treatment, for example, easy temperature control to obtain a given volume fraction of martensite.
- (2) hardenability of austenite.

Silicon is known as an element which broadens the dual phase temperature range which contributes to increase flexibility in heat treatment as been documented by Koo and Thomas [77]. Additionally, silicon increases the rate of ferrite formation, resulting in increase of hardenability of austenite.

In conclusion, an Fe-Si-Mn-C system is a desirable alloy for both heat treatments, in which the contents of carbon, manganese and silicon must be designed based on the processing condition, such as cooling rate, heat treatment cycles, on-line rolling processing etc..

5. CONCLUSIONS

The relation between solute partitioning and microstructure formation was investigated and has resulted in the following conclusions.

(1) In the AEM study of partitioning of substitutional solute alloying elements, the intensity ratio between manganese and iron was independent of foil thickness, whereas those between aluminum, silicon and iron decrease substantially with increasing foil thickness. This effect was due to absorption and requires the approximate corrections for the silicon and aluminum alloys.

(2) In the reheating experiment, including the in-situ experiment, lath martensite recrystallized and interlath carbide precipitated prior to austenite nucleation on these carbides. Finally, recrystallization was completed prior to or simultaneously with the ferrite grain growth and austenite nucleation. However, in bulk samples especially with rapid heating, the retained austenite could actually grow without a nucleation requirement. Although this was not observed in-situ in the TEM, this process cannot be ruled out. Growth of austenite was controlled by carbon diffusion in the early stage during intercritical annealing and in the later stage by substitutional element diffusion as described by Speich et al. [22], in the case of a ferrite-pearlite starting microstructure. The manganese concentration profile in the manganese steel was

analyzed by the one dimensional diffusion equation assuming local equilibrium at the interface. This equation can be applied in the case of low interface migration rates and small partitioning coefficient.

(3) In the step cooling treatment ferrite nucleation occurs along prior austenite boundaries to form grain boundary allotriomorphs. Assuming equilibrium conditions at the interface, a high manganese barrier may be present due to the low carbon concentration in austenite. Such was confirmed by the experimental line profiles of manganese concentration across the ferrite-martensite interface. The slower ferrite growth rate in the step cooling treatment than that of the reheating treatment is attributed to this high manganese barrier.

(4) The ferrite growth rate in the silicon containing steel was faster than that in the manganese containing steel. This result was explained by the respective partitioning coefficients and the effect of substitutional element on carbon activity in austenite. In the manganese containing steel, the partitioning coefficient of manganese substantially depends on the intercritical annealing conditions and was larger than those of silicon and aluminum. This high partitioning coefficient decreases the growth rate of the transformed phase. This result supports the solute drag effect theory. Manganese reduces the activity of carbon in austenite, resulting in a decrease of the driving force for ferrite growth. On the other

hand, silicon increases the carbon activity in austenite, so supporting a higher ferrite growth rate.

(5) In the niobium-manganese bearing steel, it was found that recrystallization of martensite was more sluggish and the growth rate was slower than that of the manganese bearing steel. A possible explanation for this is that niobium carbide is much more stable than cementite and hence inhibits the reaction by pinning the moving ferrite/austenite interface.

ACKNOWLEDGEMENT

The author would like to express his deepest appreciation to Professor Gareth Thomas for his guidance, encouragement, and supervision of this work. He also extends his sincere appreciation to Professor Didier de Fontaine for his valuable discussion and advice. He wishes to acknowledge Professors Hans-Rudolf Wenk and Didier de Fontaine for their review of this manuscript.

The assistance provided by the staff of the Materials and Molecular Research Division of the Lawrence Berkeley Laboratory is acknowledged. Thanks are also due to Dr. T. Dinger for his technical instruction and assistance.

The author acknowledges Nippon Kokan K. K., Japan for financial support and alloy preparation for this study. Special thanks are extended to Dr. k. Nakaoka, Technical Research Center and the staff at Education Department, Nippon Kokan K. K. for their help and encouragement.

He would like to thank all the graduate students and research fellows in the Department of Materials Science and Mineral Engineering for the friendship and assistance.

Finally, he is grateful for his family, especially his wife, Chizuko, who showed her love and endurance during his graduate study.

This work was supported by the Director, Office of Energy Research, Office of Basic Energy Science, Division of Materials Science of the U. S. Department of Energy under Contract No.

DE-AC03-76SF00098.

REFERENCES

1. S. Hayami and T. Furukawa : Microalloying 75, Union Carbide Corp., New York, 1975, P. 311.
2. J.Y. Koo and G. Thomas: Mat. Sci. Eng., 1976, vol. 24, p. 187.
3. A.T. Davenport eds.: "Formable HSLA and Dual-Phase Steels," TMS-AIME, Warrendale, PA, 1977.
4. R.A. Knot and J.W. Morris eds.: "Structure and Properties of Dual-Phase Steels", TMS-AIME, Warrendale, PA, 1979.
5. R.A. Knot and B.L. Bramfitt eds.: "Fundamentals of Dual-Phase Steels", TMS-AIME, Warrendale, PA, 1981.
6. B.L. Bramfitt and P.L. Maganon eds.: "Metallurgy of Continuous Annealed Sheet Steels", TMS-AIME, Warrendale, PA, 1982.
7. J.J. Hren, J.I. Goldstein and D.C. Joy eds.: "Introduction to Analytical Electron Microscopy", Plenum Press, New York, 1979.
8. D.B. Williams eds.: "Practical Analytical Electron Microscopy in Materials Science", Philips, 1984.
9. H.I. Aaronson: "Decomposition of Austenite by Diffusional Process", V. Zackay and H.I. Aaronson eds., Interscience Publisher Inc., New York, 1962, p. 387.
10. J.B. Bradley, J.M. Rigsbee, and H.I. Aaronson: Metall. Trans., 1977, vol. 8A, p. 323.
11. J.B. Bradley and H.I. Aaronson: Metall. Trans., 1981, vol. 12A, p. 1729.

12. W.T. Reynolds, Jr., M. Enomoto and H.I. Aaronson:
"Proceedings of International Conference on Phase Transformations in Ferrous Alloys", A.R. Marder and J.I. Goldstein eds., AIME, Warrendale, PA, 1983, p. 155.
13. T. Abe, H.I. Aaronson and G.J. Shiflet: Metall. Trans., 1985, vol. 16A, p. 521.
14. H.I. Aaronson, H.A. Domian, and G.M. Pound: Trans. AIME, 1966, vol. 236, p. 768.
15. H.I. Aaronson and H.A. Domian, Trans. AIME, 1966, vol. 236, p. 781
16. J.Y. Koo, M. Raghavan, and G. Thomas: Metall. Trans., 1980, vol. 11A, p. 351.
17. P.A. Wycliff, G.R. Purdy, and J.D. Embury: Can. Metall. Q., 1981, vol. 20, p. 339.
18. P.A. Wycliff, G.R. Purdy, and J.D. Embury: "Fundamentals of Dual Phase Steels", R.A. Kot and B.L. Bramfitt eds., TMS-AIME, Warrendale, PA, 1981, p. 59.
19. N. Pussegoda, W.R. Tyson, P. Wycliff, and G.R. Purdy: Metall. Trans., 1984, vol. 15A, p. 1499.
20. Xue-Ling Cai, A.J. Garratt-Read, and W.S. Owen: Metall. Trans., 1985, vol. 16A, p. 543.
21. A.D. Romig, Jr. and R. Saltzbrener: Scripta. Met., vol. 16, p. 33.
22. C.I. Garcia and A.J. Deardo: Metall. Trans., 1981, vol. 12A, p. 521.
23. G.R. Speich, V.A. Demarest, and R.L. Miller: Metall. Trans., 1981, vol. 12A, p. 1419.

24. M.M. Souza, J.R.C. Guimaraes, and K.K. Chawla: Metall. Trans., 1982, vol. 13A, p. 575.
25. E. Navara and R. Harrysson: Scripta. Met., 1984, vol. 18, p. 605.
26. J.J. Yi, I.S. Kim, and H.S. Choi: Metall. Trans., 1985, Vol. 16A, p. 1237.
27. D.Z. Yang, E.L. Brown, D.K. Matlock, and G. Krauss: Metall. Trans., vol. 16A, p. 1385.
28. D.Z. Yang, E.L. Brown, D.K. Matlock, and G. Krauss: Metall. Trans., vol. 16A, p. 1523.
29. R.C. Sharma, G.R. Purdy, and G.R. Kirkaldy: Metall. Trans., 1979, vol. 10A, p. 1129.
30. S.A. Al-Salman, G.W. Lorimer, and N. Ridley, Metall. Trans., 1979, vol. 10A, p. 1703.
31. M. Hillert: "Proceedings of an International Conference on Solid-Solid Phase Transformations", AIME, Warrendale, PA, 1981, p. 789.
32. N. Ridley: "Proceedings of an International Conference on Phase Transformations in Ferrous Alloys", AIME, Warrendale, Pa, 1983, p. 201.
33. O. Dairiki: "Synthesis of S-Shaped Temperature-Time-Transformation Diagrams", M.S. Thesis, University of California, Berkeley, 1983.
34. G.R. Purdy and M. Hillert: Acta. Met., 1984, vol. 32, p. 823.
35. J.W. Christian and D.V. Edmonds: "Proceedings of an International Conference on Phase Transformations in

- Ferrous Alloys", A.R. Marder and J.I. Goldstein eds.,
AIME, Warrendale, PA, 1983, p. 293.
36. H.I. Aaronson, H.A. Domian, and G.M. Pound: Trans. AIME,
1966, vol. 236, p. 753.
37. H.I. Aaronson and H.A. Domian: Trans. AIME, 1966, vol. 236,
p. 781.
38. M. Hillert: Metall. Trans., 1984, vol. 15A, p. 411.
39. M.R. Plichta, W.A.T. Clark and H.I. Aaronson: Metall. Trans.,
1984, vol. 15A, p. 427.
40. T. Ando and G. Krauss: Metall. Trans., 1982, vol. 14A,
p. 1261.
41. M. Hillert: Suppl. Trans. ISIJ, Proceedings ICSTIS, 1971,
vol. 11, p. 1153.
42. J.W. Christian: "The Theory of Transformations in Metals
and Alloys", Pergamon Press, New York, 1965.
43. A. Hultgren: Trans. ASM, 1947, vol. 39, p. 915.
44. M. Hillert: "Paraequilibrium and Other Restricted
Equilibria", In Alloy Phase Diagram, L.H. Mennett,
T.B. Massalski, and B.C. Gibson eds., MRS Symposia, vol. 19,
North-Holland, New York, 1983.
45. G.R. Purdy, D.H. Weichert, and J.S. Kirkaldy: Trans. AIME,
1964, vol. 230, p. 1025.
46. J.S. Gilmour, G.R. Purdy, and J.S. Kirkaldy: Metall. Trans.,
1972, vol. 3, p. 1455.
47. J.S. Gilmour, G.R. Purdy, and J.S. Kirkaldy: Metall. Trans.,
1972, vol. 3, p. 3213.
48. K. Lücke and K. Detert: Acta. Met., 1957, vol. 5, p. 628.

49. J.W. Cahn: *Acta. Met.*, 1962, vol. 10, p. 789.
50. K. Lücke and H. Stüwe: "Recovery and Recrystallization of Metals", Interscience, New York, 1963.
51. M. Hillert: "The Mechanism of Phase Transformations in Crystalline Solids", Institute Metals, London, 1969, p. 231.
52. K.R. Kinsman and H.I. Aaronson: "Transformation and Hardenability in Steels", Climax Molybdenum Co., Ann Arbor, MI, 1967, p. 39.
53. M. Hillert and J. Agren: *Metall. Trans.*, 1985, vol. 16A, p. 1609.
54. M. Sarikaya, G. Thomas, and J.W. Steeds: "Proceedings of an International Conference on Solid-Solid Phase Transformations", H.I. Aaronson, D.E. Laughlin, R.F. Sekerka, and C.M. Wayman eds., AIME, Warrendale, PA, 1981, p. 1421.
55. G. Thomas: *Metall. Trans.*, 1978, vol. 9A, p. 439.
56. B.V.N. Rao and G. Thomas: *Metall. Trans.*, 1980, vol. 11A, p. 441.
57. J. Mansfield: "Convergent Beam Electron Diffraction of Alloy Phases", The Bristol Group, Adam Hilger Ltd., Bristol and Boston, 1984.
58. R. Tixier and J. Philibert: "Proceedings of 5th International Congress on X-ray Optics and Microanalysis", G. Mollenstedt and K.H. Ganklen, Springer-Verlag, Berlin, 1969.
59. J.I. Goldstein, D.E. Newbury, P. Echlin, D.C. Joy, C. Fiori, and E. Lifshin : "Scanning Electron Microscopy and X-ray Microanalysis", Plenum Press, 1981.

60. International Tables for X-ray Crystallography, Birmingham, England, Kynoch Press, Vol. 3.
61. R.W.K. Honeycombe: "Steels—Microstructure and Properties", Amer. Soc. for Metals, Metals Park, Ohio, 1982.
62. G. Krauss: "Principals of Heat Treatment of Steel", Amer. Soc. for Metals, Metals Park, Ohio, 1980.
63. M. Hillert: Metall. Trans., 1975, vol. 6A, p. 5.
64. B. Uhrenius: "Proceedings of Hardenability Concepts with Application to Steels", D.V. Doane and J.S. Kirkaldy eds., AIME, Warrendale, 1978, p. 28.
65. A. Kritz and F. Polonil: J. Iron Steel Inst., 1932, vol. 126, p. 323.
66. R.D. Smith: J. Amer. Chem. Soc., 1948, vol. 70, p. 2724.
67. M. Hillert: Acta. Met., 1955, vol. 3, p. 34.
68. K.R. Kinsman and H.I. Aaronson: Metall. Trans., 1973, vol. 4, p. 959.
69. "Atlas of Isothermal Transformation and Cooling Transformation Diagrams", ASM, Metals Park, Ohio, 1977.
70. M.D. Gaib, D.K. Matlock, and G. Krauss: Metall. Trans., 1980, vol. 11A, p. 1983.
71. R.H. Hoel and G. Thomas: Scripta Met., 1981, vol. 15, p. 867.
72. J.S. Gau and G. Thomas: "Metallurgy of Continuous Annealed Sheet Steels", B.L. Bramfitt and P.L. Maganon eds., TMS-AIME, Warrendale, PA, 1982.
73. P.G. Shewmon: Trans. AIME, 1965, vol. 223, p. 736.
74. F.R. Monal: J. Iron and Steel Inst., 1934, vol. 130, p. 419.
75. W.C. Leslie and G.C. Rauch: Metall. Trans., 1978, vol. 9A,

- p. 343.
76. H. Schenck and H. Kaiser: Arch. Eisenhüttenw., 1960, vol. 31,
p. 227.
77. J.Y. Koo and G. Thomas: Metall. Trans., 1977, vol. 8A,
p. 525.
78. N. Nakaoka, K. Araki, and K. Kurihara: "Formable HSLA and
Dual Phase Steels". A.T. Davenport eds., TMS-AIME,
Warrendale, PA, 1977, p. 128.
79. N. Nakaoka, Y. Hosoya, M. Ohmura, and A. Nishimoto:
"Structure and Properties of Dual Phase Steels", R.A. Kot and
J.W. Morris eds., TMS-AIME, Warrendale, PA, 1979, p. 330.
80. R.G. Davies: Metall. Trans., 1979, vol. 10A, p. 113.

Table I
Alloy Compositions (wt. %)

Alloy Designation	Fe	C	Si	Mn	P	S	Sol. Al	N	Nb
M 1	bal.	0.095	—	1.53	0.004	0.002	0.018	0.001	—
M 2	bal.	0.094	—	1.51	0.004	0.002	0.023	0.001	0.110
S 1	bal.	0.105	2.16	0.39	0.004	0.002	0.031	0.001	—
S 2	bal.	0.053	2.06	0.28	0.005	0.005	0.034	0.002	—
S 3	bal.	0.215	2.09	0.28	0.005	0.006	0.034	0.003	—
A	bal.	0.098	—	0.38	0.005	0.002	1.070	0.001	—

XBL 8510-6636A

Table 2
Influence of Substitutional Solutes on Carbon Activity

Solute	Mn	Si	Al
Carbon Activity in Austenite	decrease	increase	decrease
Carbon Activity in Ferrite	decrease	increase	decrease
Carbon Activity in Cementite	decrease	increase	increase

Figure Captions

- Fig. 1. Schematic of heat treatment of the reheating treatment.
- Fig. 2. Schematic of heat treatment of the step cooling treatment.
- Fig. 3. Schematic drawing of isothermal dilatometry in the reheating treatment. (a) heat cycle and variation of length with isothermal annealing time, (b) variation of length with isothermal annealing temperature.
- Fig. 4. Schematic drawing of isothermal dilatometry in the step cooling treatment. (a) heat cycle and variation of length with isothermal annealing time, (b) variation of length with isothermal annealing temperature.
- Fig. 5. Transmission electron micrographs of the starting microstructure before intercritical annealing of the alloy M1 showing lath martensite structure. (a) bright field, (b) dark field from $(002)_{\gamma}$ reflection, (c) SAD pattern, (d) analyzed pattern.
- Fig. 6. Transmission electron micrographs showing the microstructure of the alloy M1 in the very early stage of the intercritical annealing. (a) bright field, (b) dark field.
- Fig. 7. Scanning electron micrographs showing the change in microstructure of the alloy M1 after isothermal annealing at 730°C in the reheating treatment. (a) 10 min., (b) 30 min., (c) 2 hrs, (d) 8 hrs, (e) 32 hrs; Specimens water quenched from 730°C .

Fig. 8. Scanning electron micrographs showing the change in microstructure of the alloy M2 after isothermal annealing at 730°C in the reheating treatment. (a) 10 min., (b) 30 min., (c) 2 hrs, (d) 8 hrs, (e) 32 hrs; Specimens water quenched from 730°C.

Fig. 9. Scanning electron micrographs showing the change in microstructure of the alloy S1 after isothermal annealing at 850°C in the reheating treatment. (a) 10 min., (b) 30 min., (c) 2 hrs, (d) 8 hrs, (e) 32 hrs; Specimens water quenched from 850°C.

Fig. 10. Scanning electron micrographs showing the change in microstructure of the alloy M1 after isothermal annealing at 800°C in the reheating treatment. (a) 10 min., (b) 2 hrs; Specimens water quenched from 800°C.

Fig. 11. A sequence of TEM micrographs showing in situ phase transformation of the alloy M1 by the hot stage high voltage microscope operated at 1500 kV. (a) starting microstructure at room temperature, (b) 650°C, (c) 710°C, (d) 730°C, (e) 5 min., at 730°C, (f) 60 min. at 730°C.

Fig. 12. Transmission electron micrographs of alloy M2 by the hot stage high voltage microscope operated at 1500 kV. (a) starting microstructure at room temperature, (b) 60 minutes isothermal annealing at 730°C.

Fig. 13. Optical micrographs showing the change in microstructure of the alloy M1 after isothermal

annealing at 730°C in the step cooling treatment.
(a) 10 min., (b) 30 min., (c) 2 hrs, (d) 8 hrs,
(e) 32 hrs; Specimens water quenched from 730°C.

Fig. 14. Optical micrographs showing the change in microstructure of the alloy M2 after isothermal annealing at 730°C in the step cooling treatment.
(a) 10 min., (b) 30 min., (c) 2 hrs, (d) 8 hrs,
(e) 32 hrs; Specimens water quenched from 730°C.

Fig. 15. Optical micrographs showing the change in microstructure of the alloy S1 after isothermal annealing at 850°C in the step cooling treatment.
(a) 10 min., (b) 30 min., (c) 2 hrs, (d) 8 hrs;
Specimens water quenched from 850°C.

Fig. 16. Variation of the volume fraction of martensite with the isothermal annealing time.

Fig. 17. Dilatation curves for the alloy M1 in the reheating treatment.

Fig. 18. Dilatation curves for the alloy M1 in the step cooling treatment.

Fig. 19. Transmission electron micrographs of dual phase structure.

(a) manganese containing steel, M1, intercritically annealed for 2 hrs at 800°C in the reheating treatment.

(b) silicon containing steel, S1, intercritically annealed for 2 hrs at 850°C in the reheating treatment.

- (c) aluminum containing steel, A, intercritically annealed for 2 hrs at 850°C in the reheating treatment.
- (d) manganese containing steel, M1, intercritically annealed for 2 hrs at 730°C in the step cooling treatment.
- (e) silicon containing steel, S1, intercritically annealed for 2 hrs at 850°C in the step cooling treatment.

Fig. 20. Manganese concentration profile of the alloy M1 intercritically annealed for 2 hrs at 730°C in the reheating treatment.

Fig. 21. Manganese concentration profile of the alloy M1 intercritically annealed for 2 hrs at 730°C in the reheating treatment.

Fig. 22. Manganese concentration profile of the alloy M1 intercritically annealed for 10 min. at 800°C in the reheating treatment.

Fig. 23. Manganese concentration profile of the alloy M1 intercritically annealed for 2 hrs at 800°C in the reheating treatment.

Fig. 24. Manganese concentration profile of the alloy M1 intercritically annealed for 32 hrs at 800°C in the reheating treatment.

Fig. 25. Manganese concentration profile of the alloy M2 intercritically annealed for 2 hrs at 800°C in the reheating treatment.

- Fig. 26. Silicon concentration profile of the alloy S1 intercritically annealed for 30 min. at 850°C in the reheating treatment.
- Fig. 27. Silicon concentration profile of the alloy S1 intercritically annealed for 32hrs at 850°C in the reheating treatment.
- Fig. 28. Manganese concentration profile of the alloy M1 intercritically annealed for 2 hrs at 730°C in the step cooling treatment.
- Fig. 29. Manganese concentration profile of the alloy M1 intercritically annealed for 32 hrs at 730°C in the step cooling treatment.
- Fig. 30. Manganese concentration profile of the alloy M2 intercritically annealed for 2 hrs at 730°C in the step cooling treatment.
- Fig. 31. Silicon concentration profile of the alloy S1 intercritically annealed for 2 hrs at 850°C in the step cooling treatment.
- Fig. 32. Variation of Mn/Fe intensity ratio with the Fe x-ray counts of the alloy M1 intercritically annealed for 32 hrs at 800°C in the reheating treatment.
- Fig. 33. Variation of Si/Fe intensity ratio with the Fe x-ray counts of the alloy S1 intercritically annealed for 2 hrs at 800°C in the reheating treatment.
- Fig. 34. Variation of Si/Fe intensity ratio with the Fe x-ray counts of the alloy S1 intercritically annealed for 30 min. at 850°C in the reheating treatment.

- Fig. 35. Variation of Si/Fe intensity ratio with the Fe x-ray counts of the alloy S1 intercritically annealed for 2 hrs at 850°C in the reheating treatment.
- Fig. 36. Variation of Si/Fe intensity ratio with the Fe x-ray counts of the alloy S1 intercritically annealed for 2 hrs at 930°C in the reheating treatment.
- Fig. 37. Variation of Si/Fe intensity ratio with the Fe x-ray counts of the alloy S3 intercritically annealed for 2 hrs at 850°C in the reheating treatment.
- Fig. 38. Variation of Si/Fe intensity ratio with the Fe x-ray counts of the alloy S2 intercritically annealed for 2 hrs at 930°C in the reheating treatment.
- Fig. 39. Variation of Al/Fe intensity ratio with the Fe x-ray counts of the alloy A intercritically annealed for 2 hrs at 800°C in the reheating treatment.
- Fig. 40. Variation of Al/Fe intensity ratio with the Fe x-ray counts of the alloy A intercritically annealed for 2 hrs at 850°C in the reheating treatment.
- Fig. 41. Variation of Al/Fe intensity ratio with the Fe x-ray counts of the alloy A intercritically annealed for 2 hrs at 930°C in the reheating treatment.
- Fig. 42. Variation of partitioning coefficients with the intercritical annealing times.
- Fig. 43. Variation of partitioning coefficients with the intercritical annealing temperatures.
- Fig. 44. Variation of partitioning coefficients with the carbon contents of silicon containing steels.

- Fig. 45. Convergent Beam Electron Diffraction patterns from the alloy M1 in (210) orientation. (a) ferrite, (b) martensite.
- Fig. 46. Absorption coefficients of iron showing iron K absorption edge and $K\alpha$ x-ray of manganese, silicon, and aluminum.
- Fig. 47. EDS spectra taken from the alloy A.
- Fig. 48. Isothermal phase diagram of the Fe-Mn-C system at 730°C.
- Fig. 49. Isothermal phase diagram of the Fe-Si-C system at 850°C.
- Fig. 50. Calculated manganese concentration profile in both static and moving boundaries.
- Fig. 51. Manganese concentration profiles and calculated profiles.
(a) 730°C x 2 hrs, (b) 730°C x 32 hrs,
(c) 800°C x 2 hrs, (d) 800°C x 32 hrs.
- Fig. 52. An isothermal dilatation curve for the alloy M1 at 700°C and calculated dilatation curve based on the Avrami rate equation.
- Fig. 53. Schematic drawing of the microstructure formation of the manganese and silicon containing steels in the reheating treatment.
- Fig. 54. Schematic drawing of the microstructure formation of the manganese and silicon containing steels in the reheating treatment.

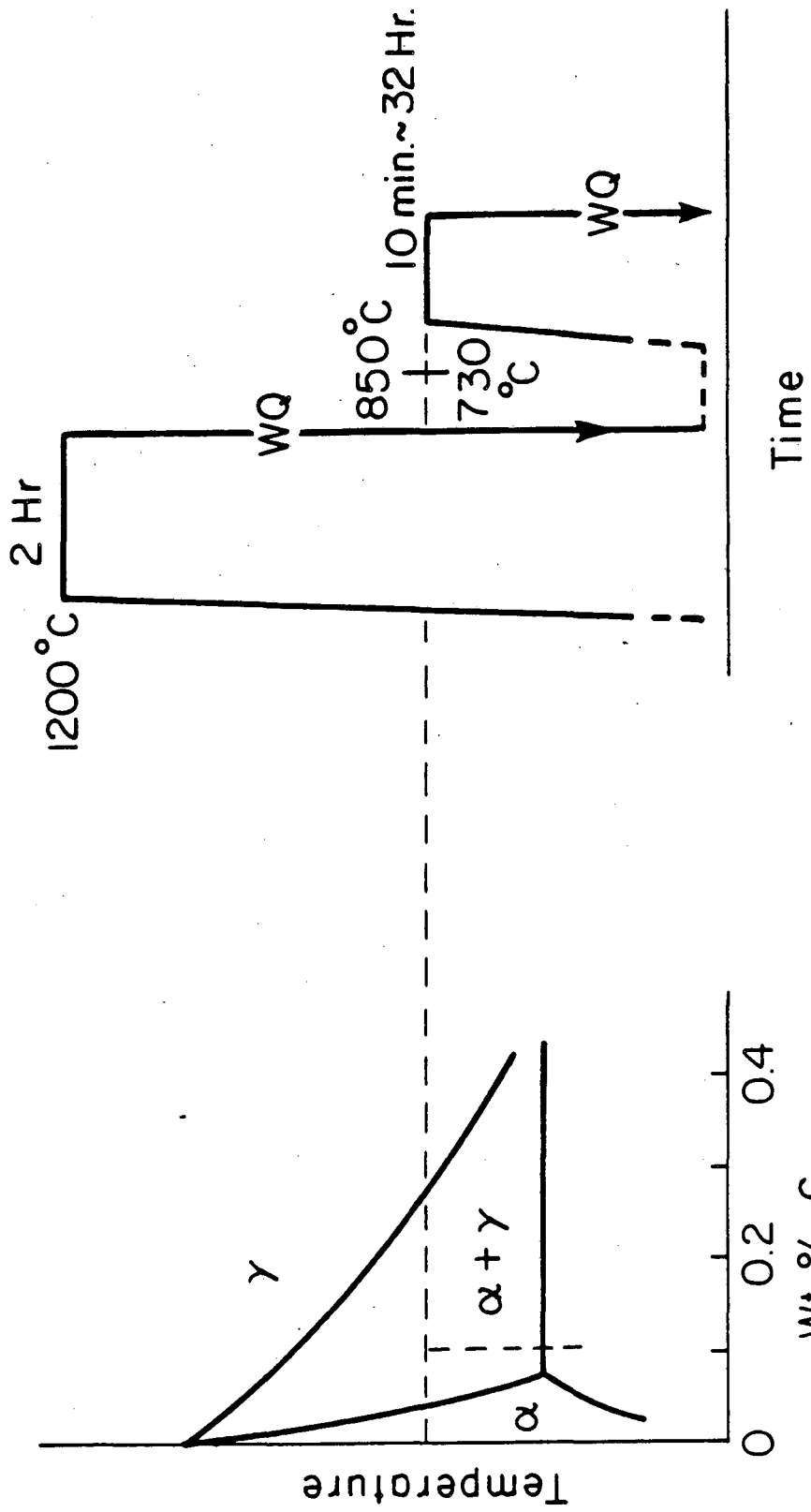
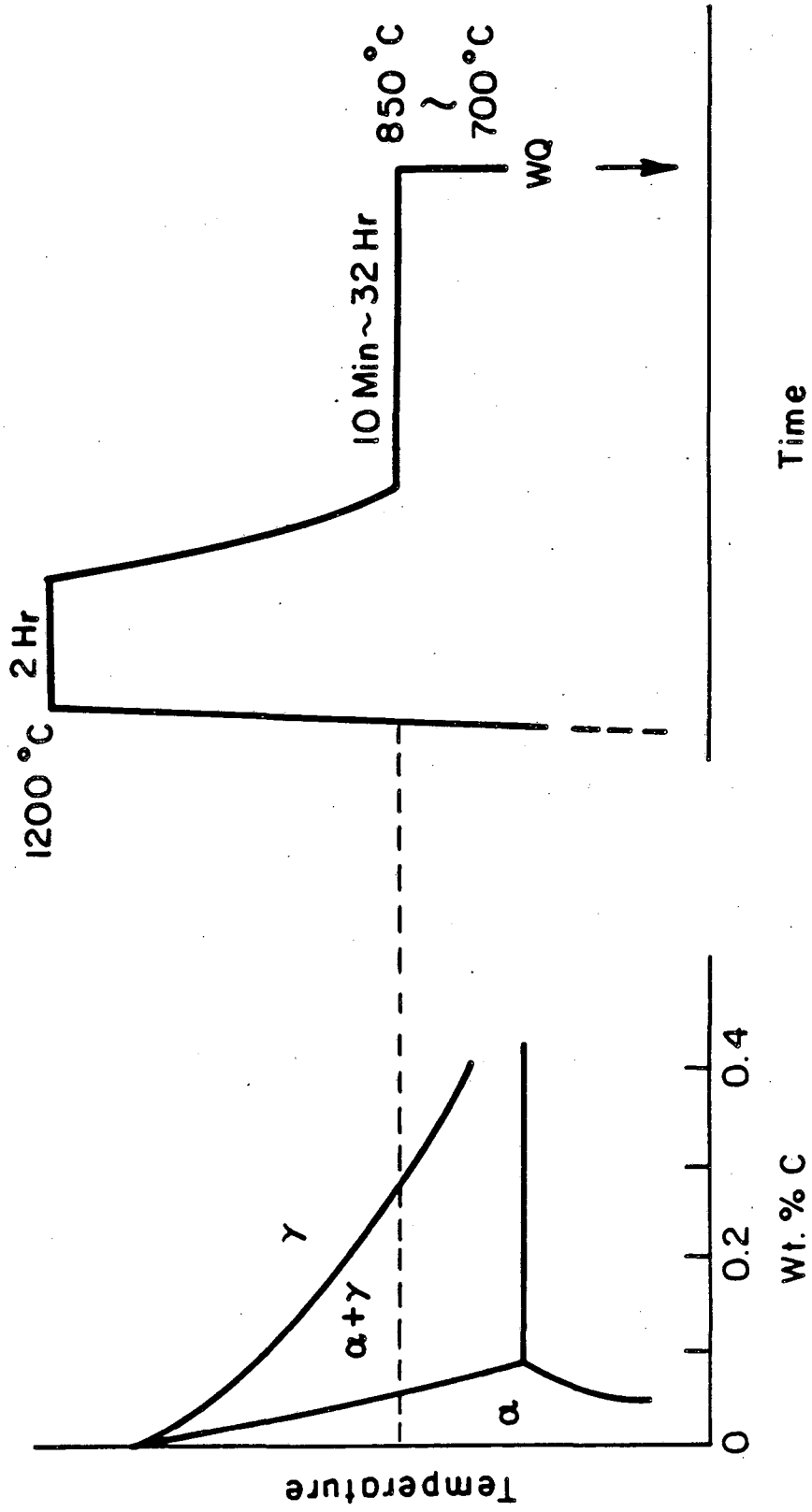


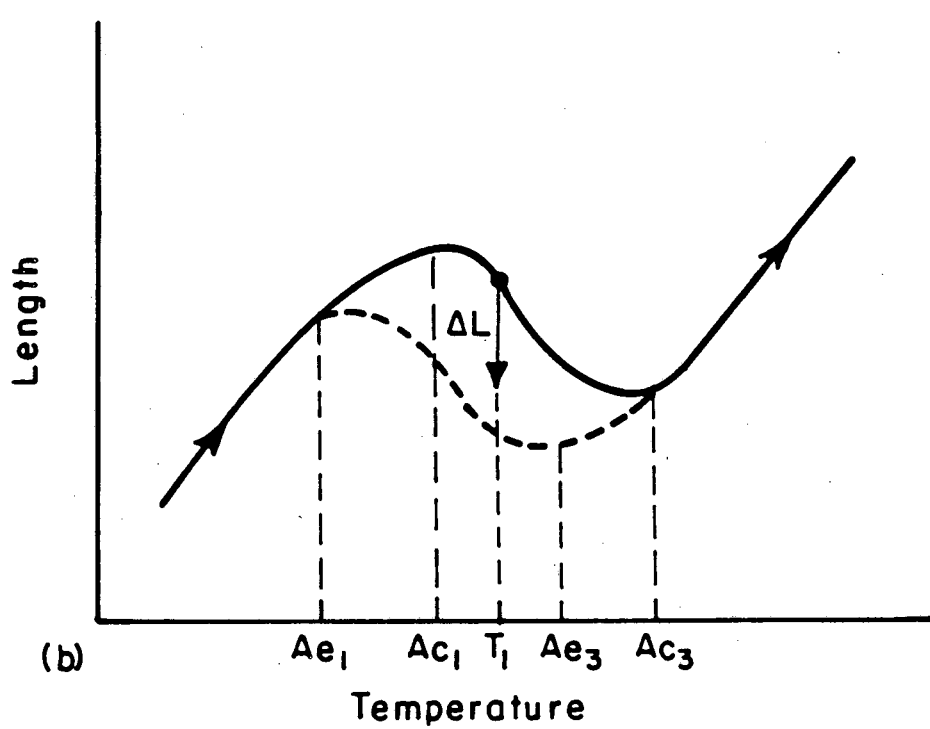
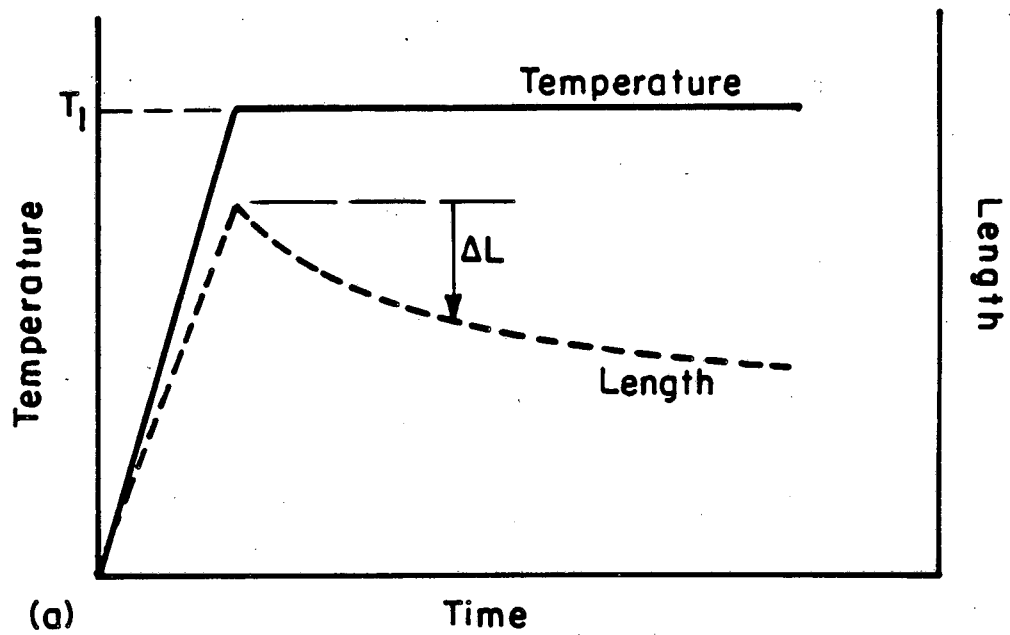
Fig. 1

XBL 85I-5804A



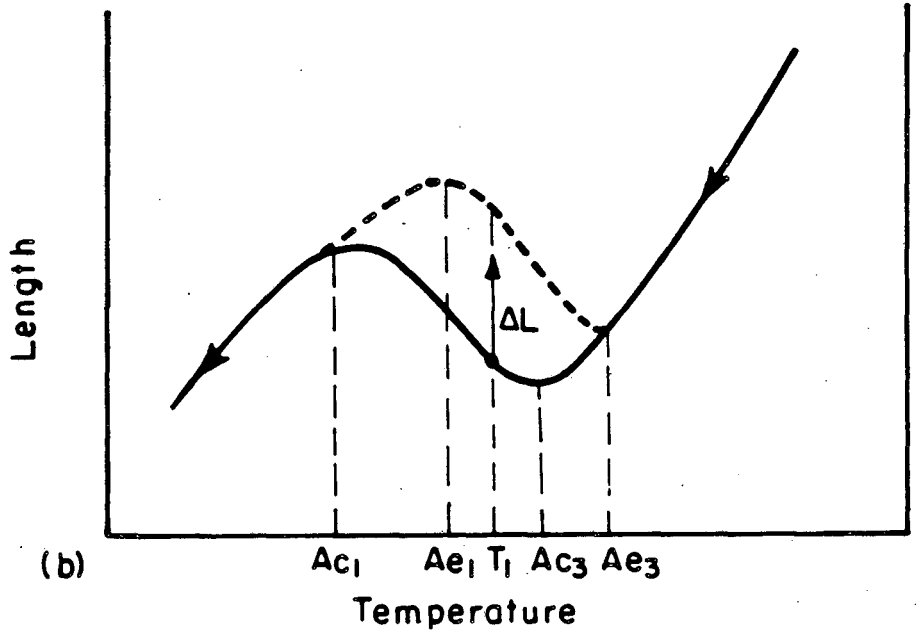
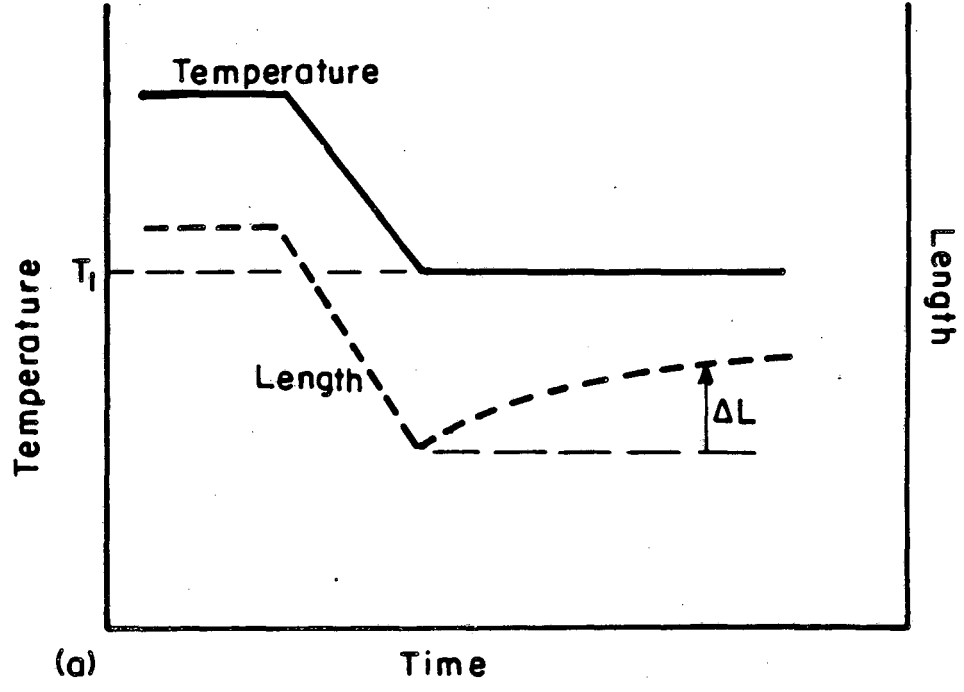
XBL8510-6634

Fig. 2



XBL8510-6718

Fig. 3



XBL 8510-6719

Fig. 4

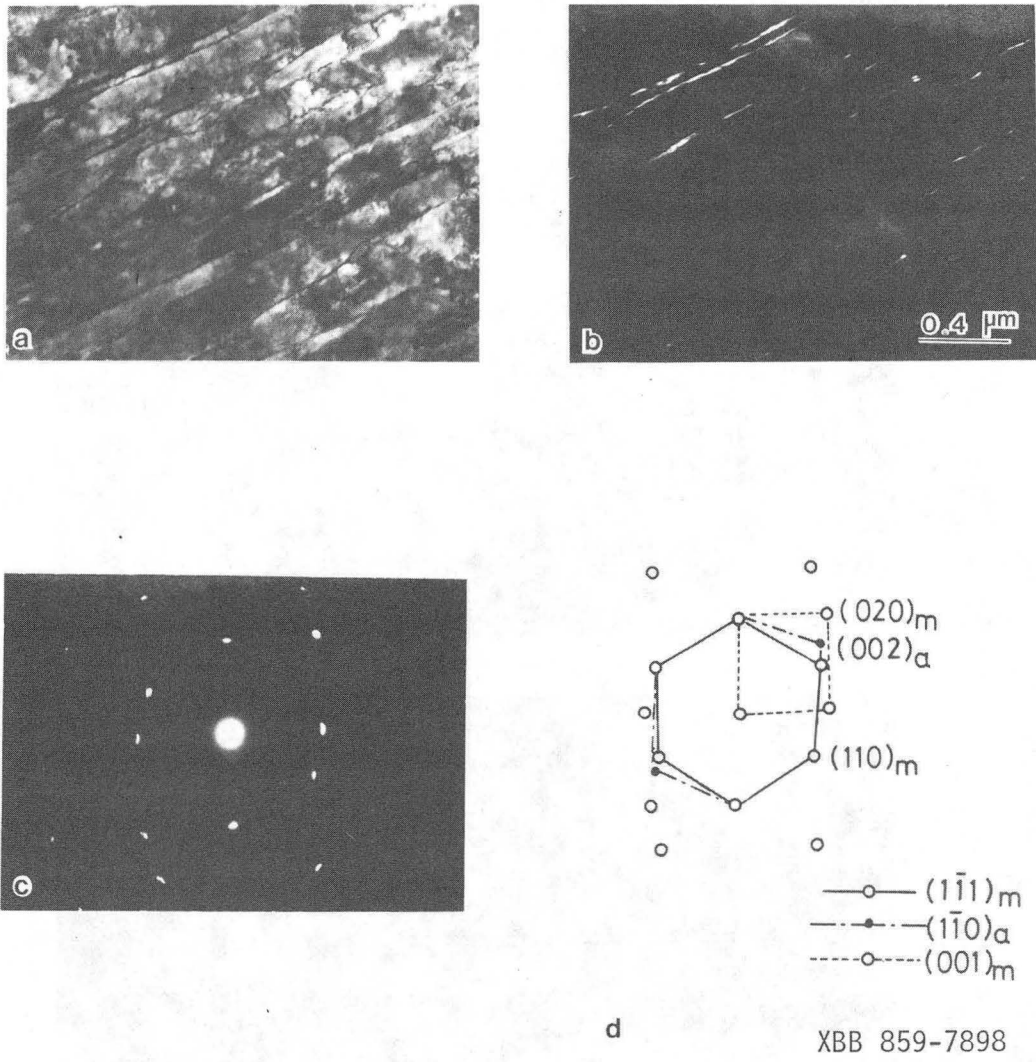
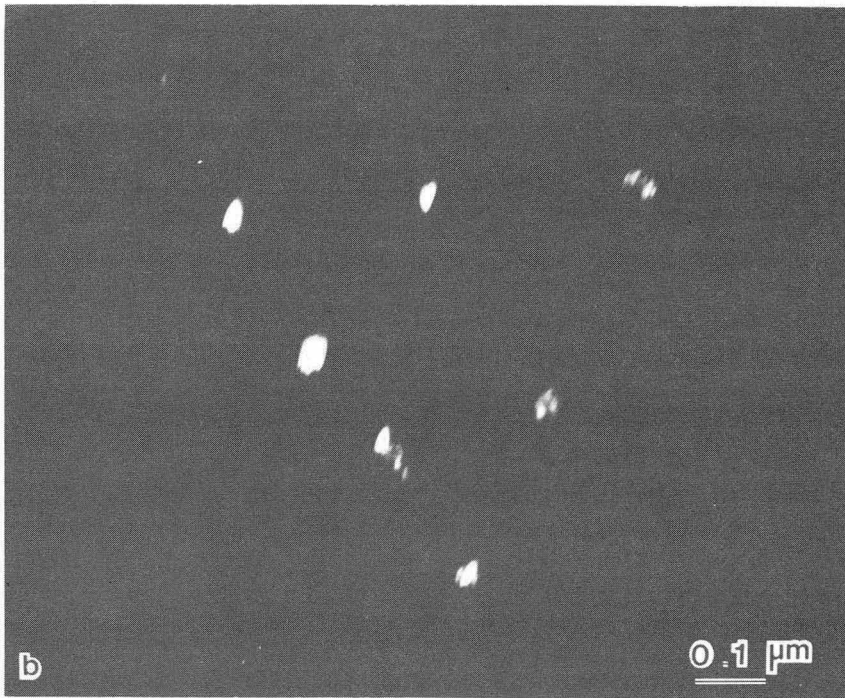
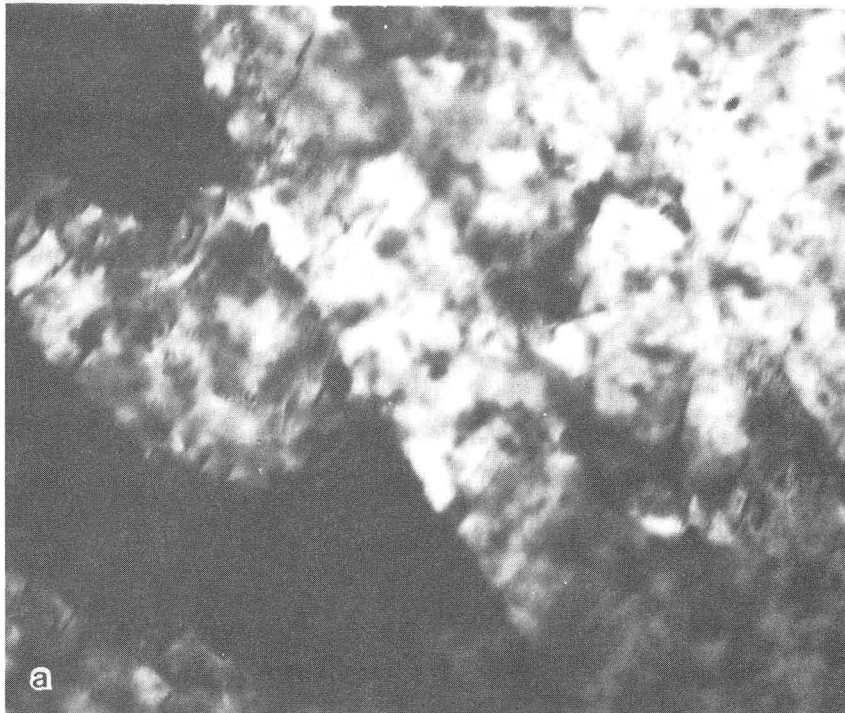
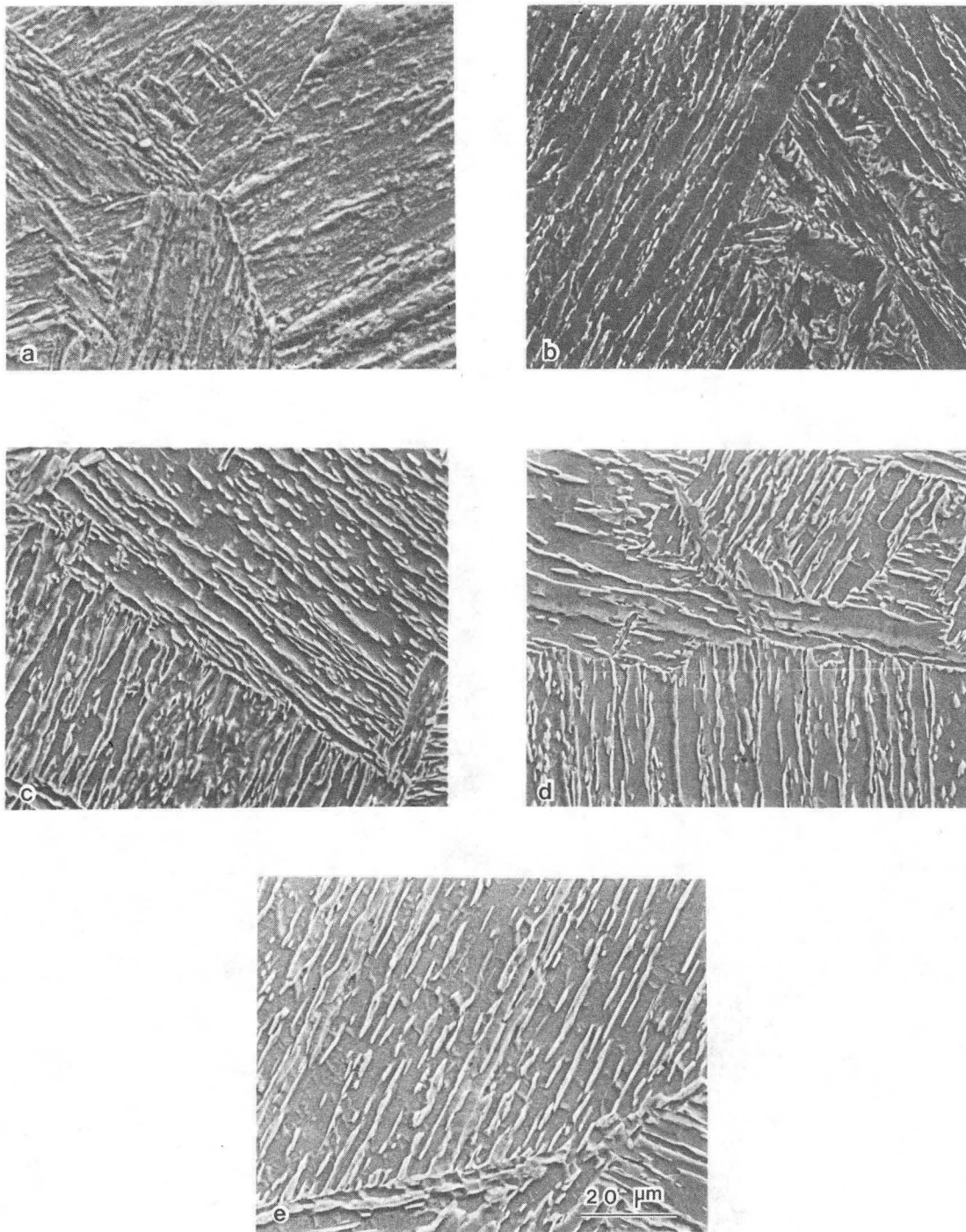


Fig. 5



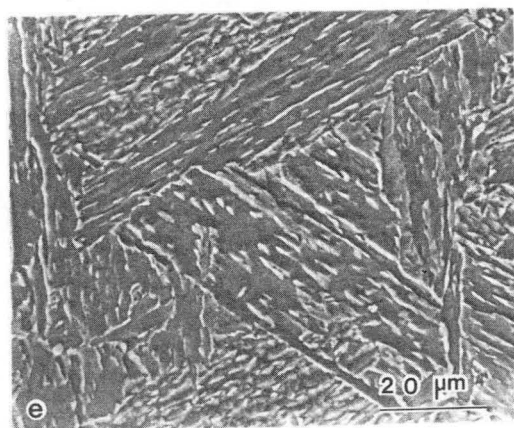
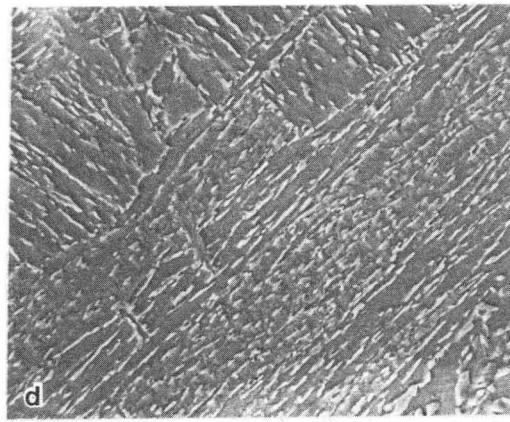
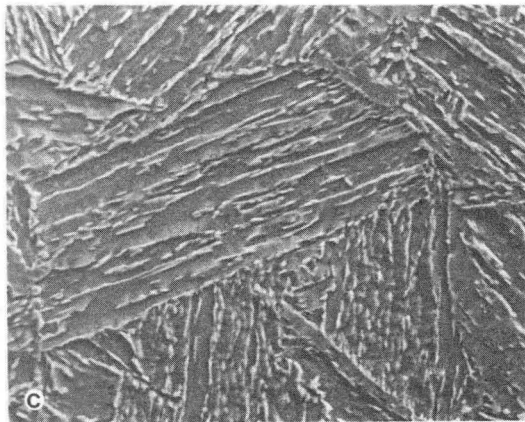
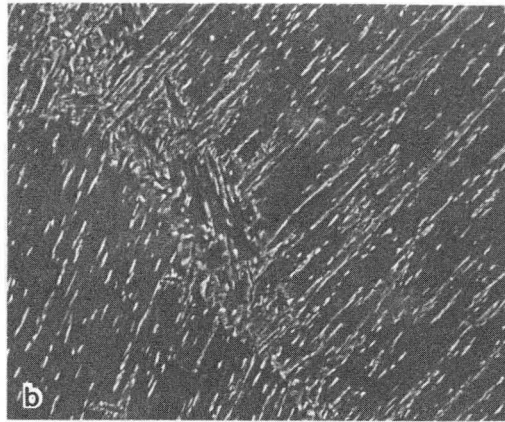
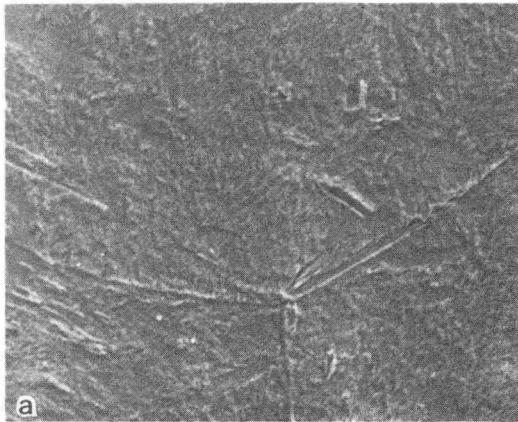
XBB 850-8248

Fig. 6



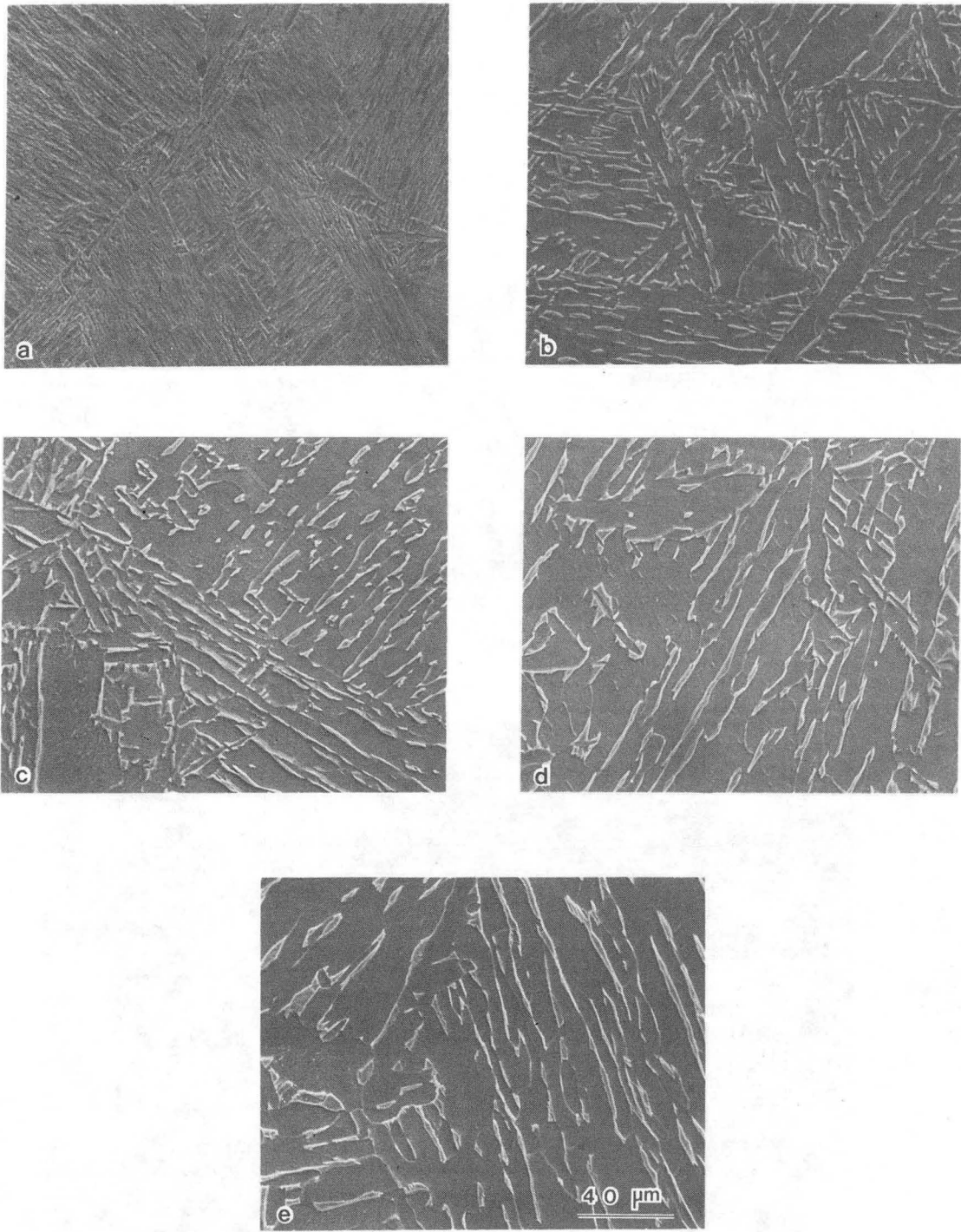
XBB 859-7895

Fig. 7



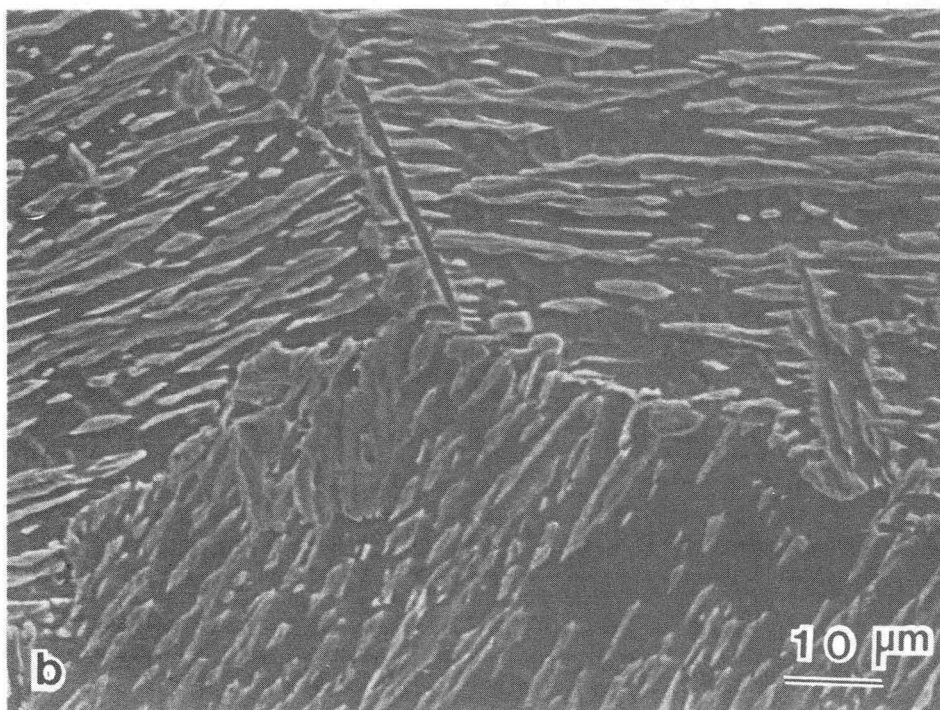
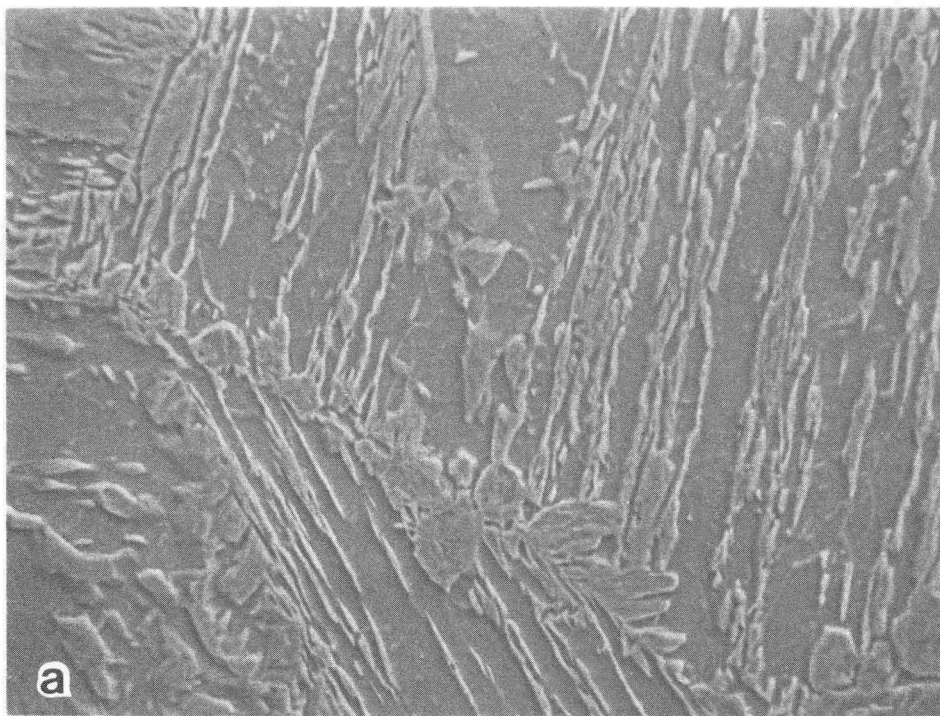
XBB 859-7896

Fig. 8



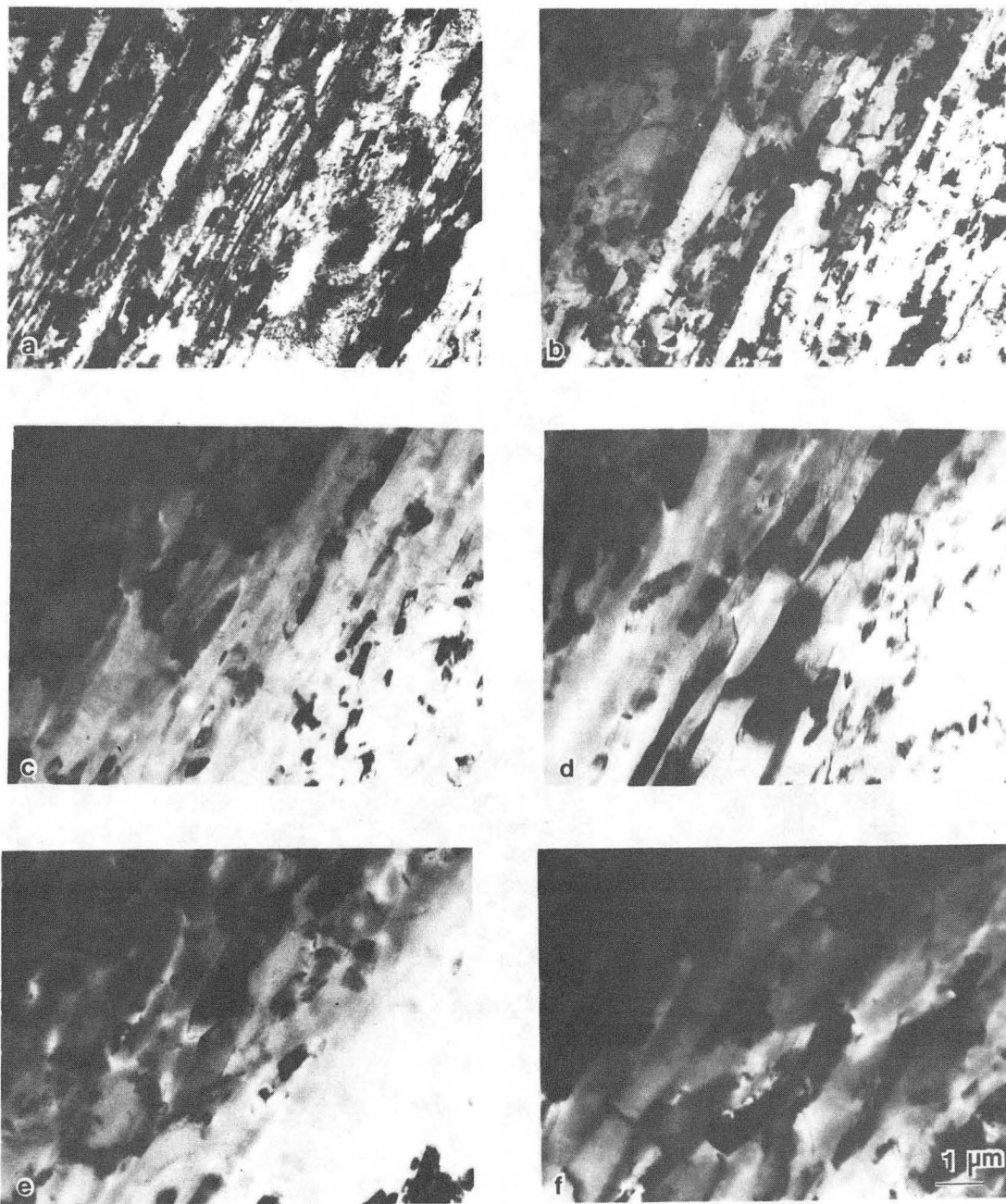
XBB 859-7897

Fig. 9



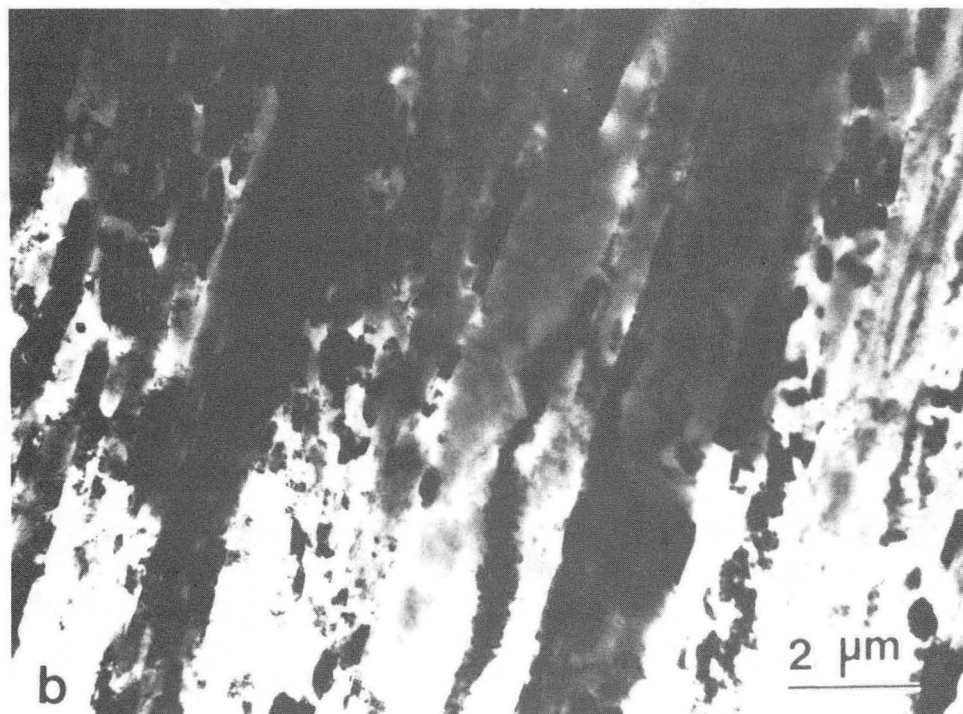
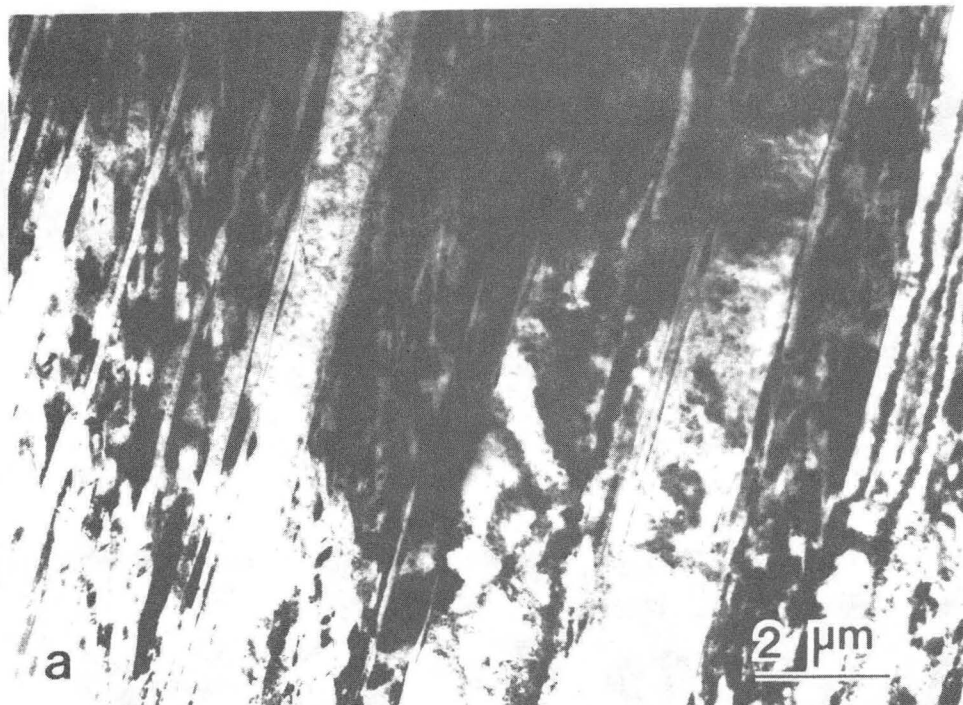
XBB 850-9222

Fig. 10



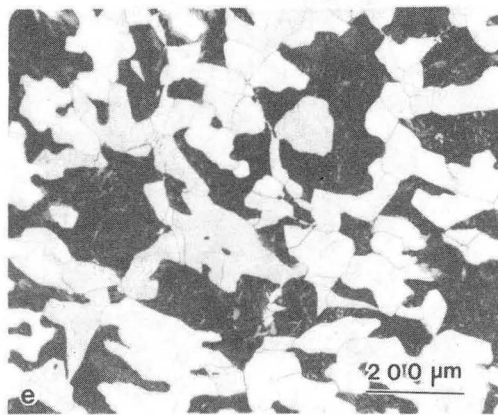
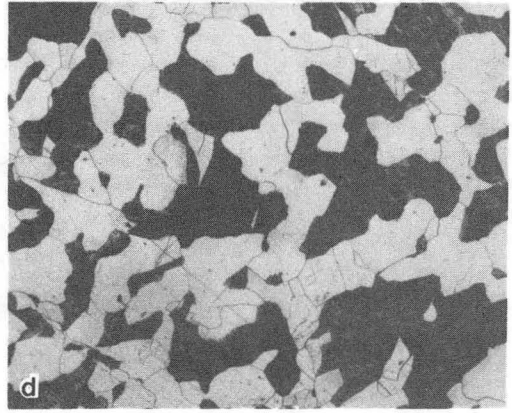
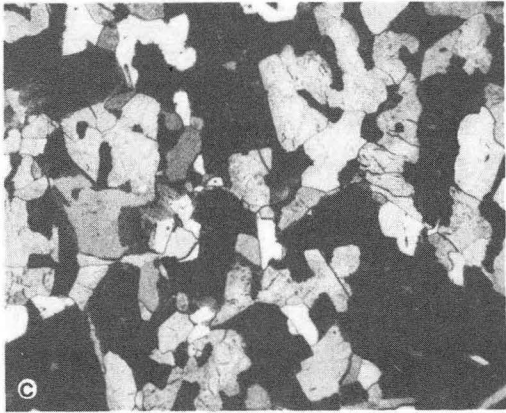
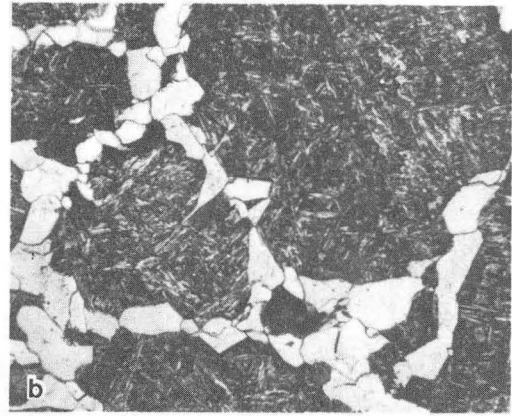
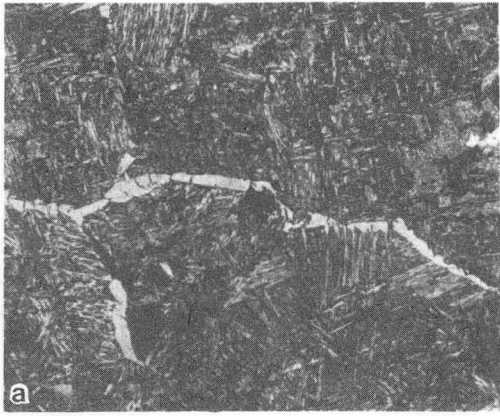
XBB 850-9422

Fig. 11



XBB 851-911

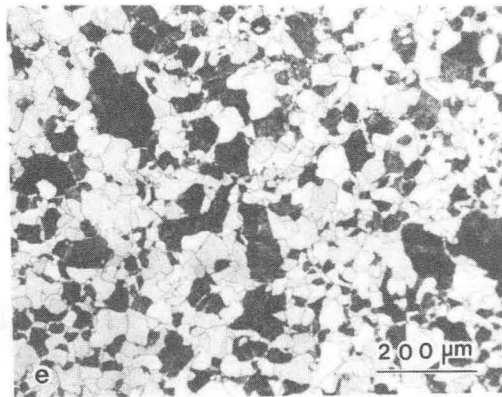
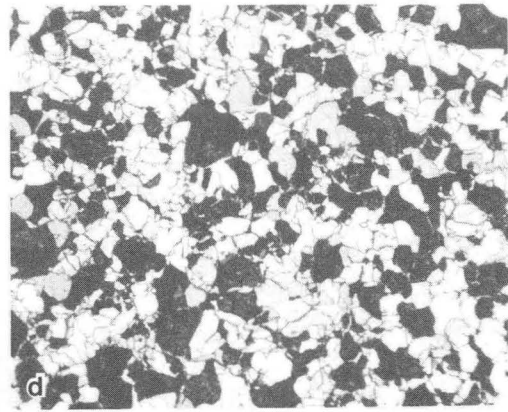
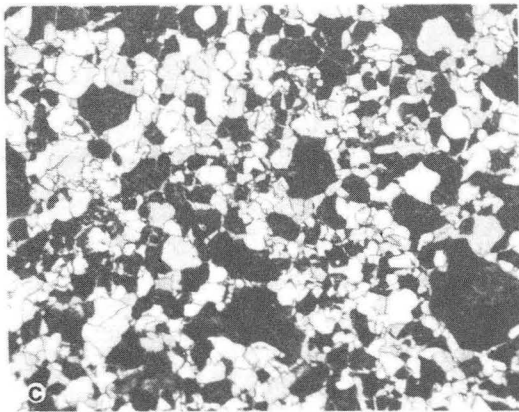
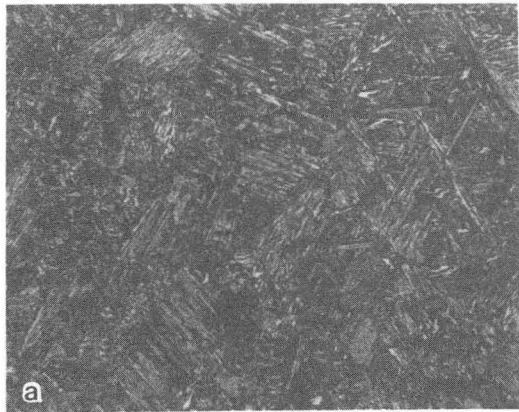
Fig. 12



200 μm

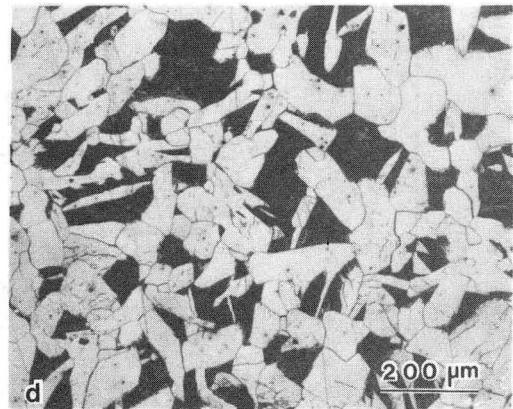
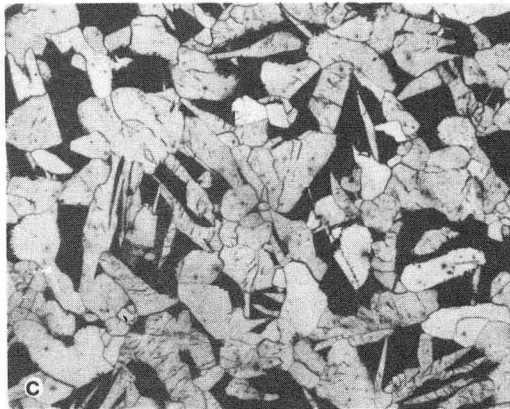
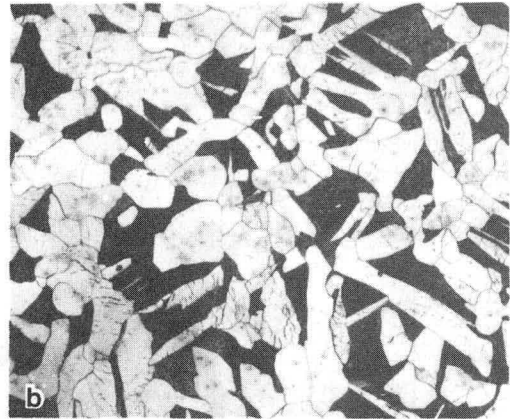
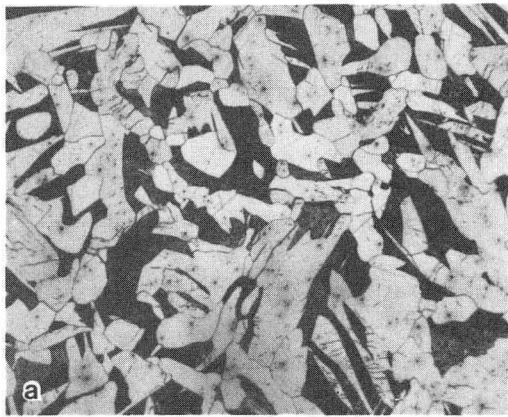
XBB 859-7892

Fig. 13



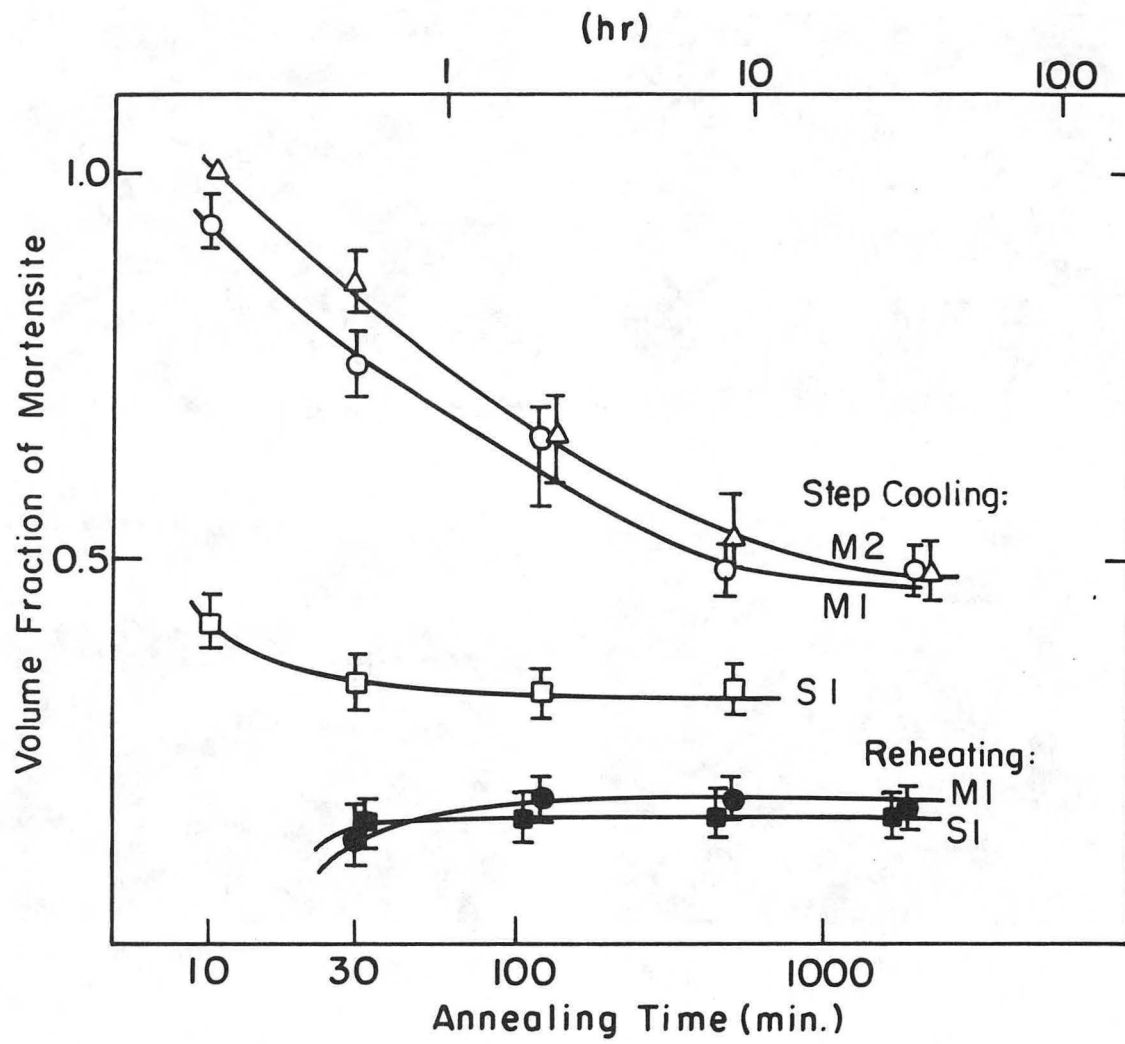
XBB 859-7894

Fig. 14



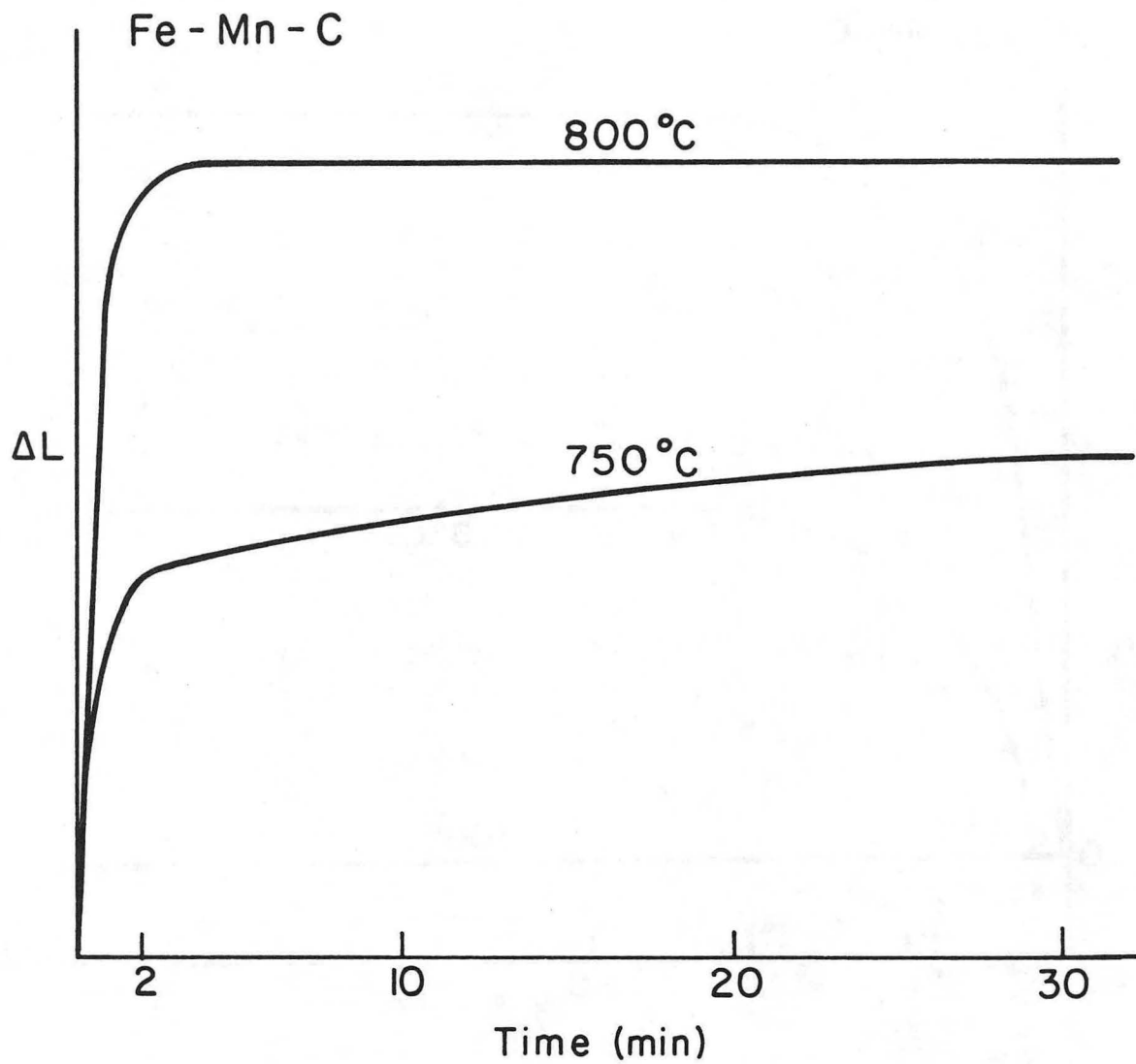
XBB 859-7893

Fig. 15



XBL 8510-6650

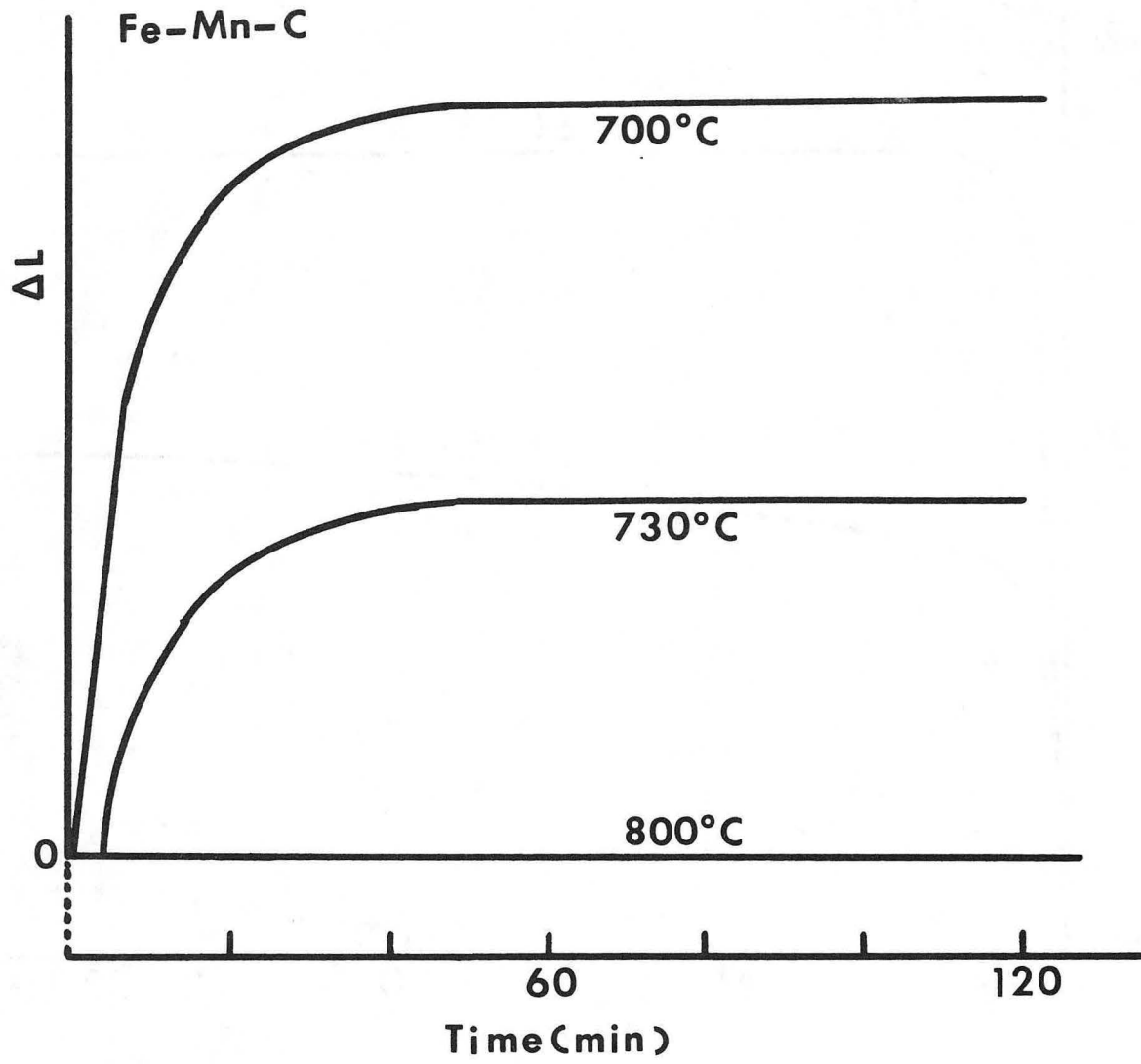
Fig. 16



Dilatation Temperature Curves

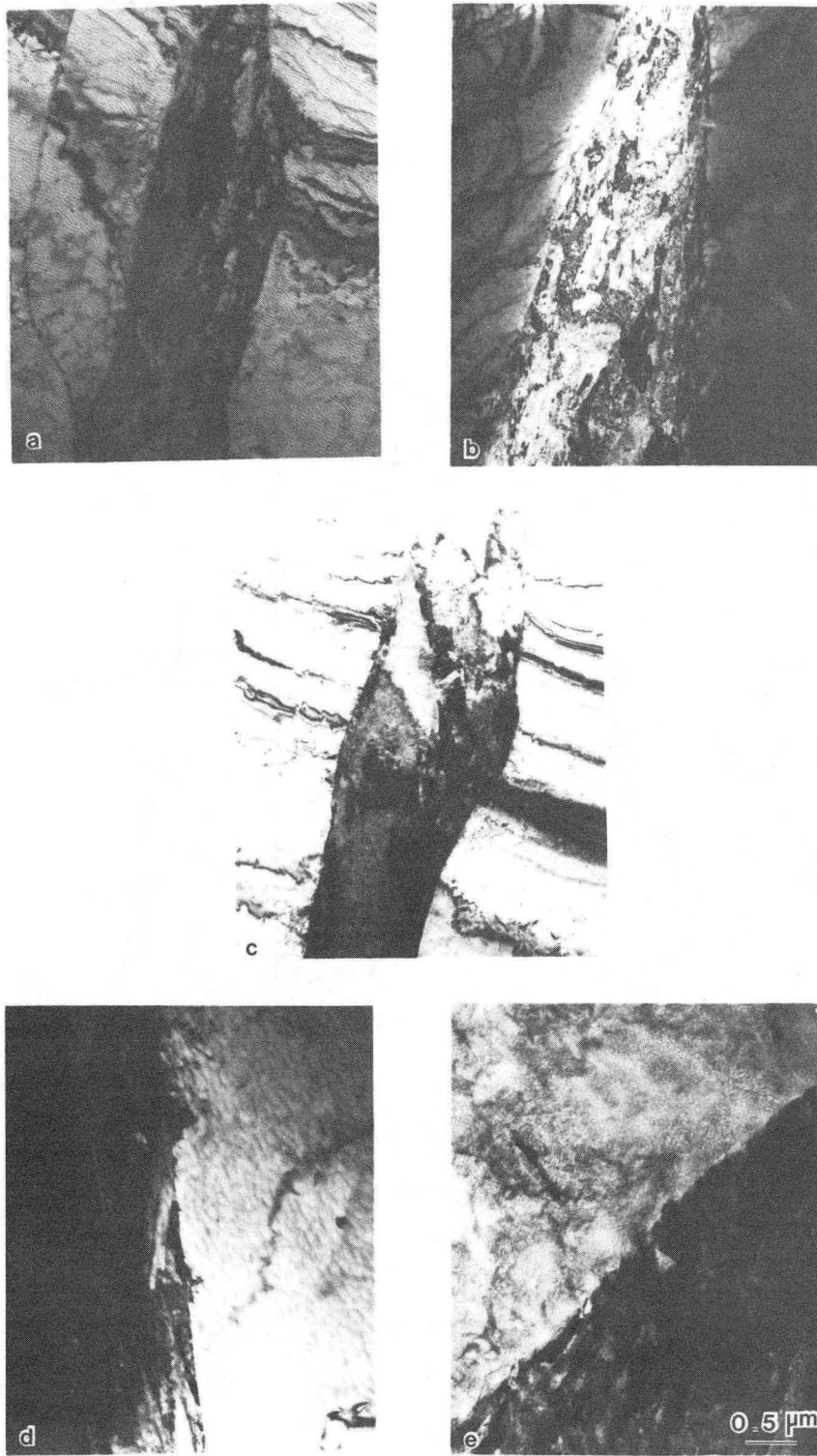
XBL 853 - 5926

Fig. 17



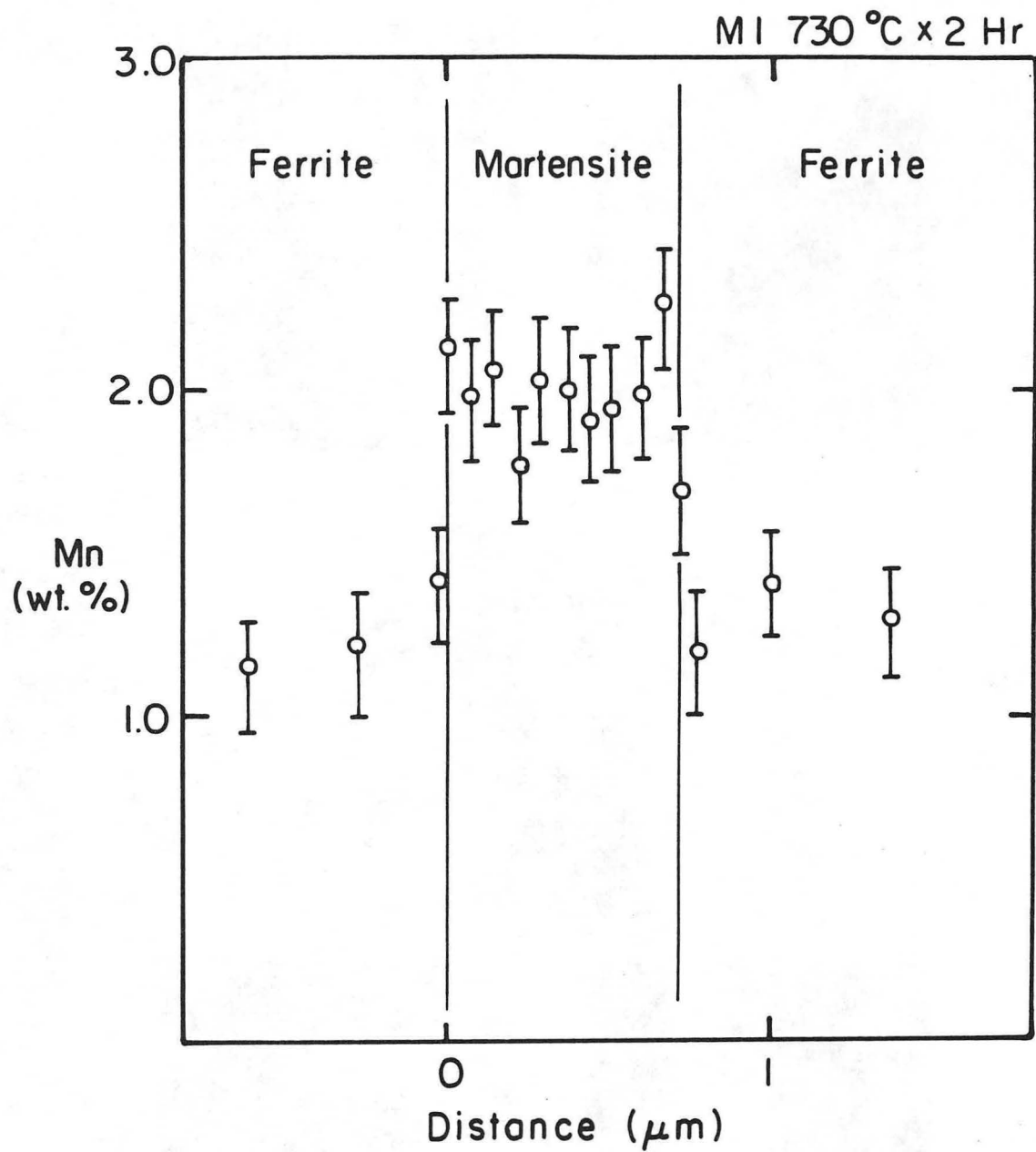
XBL 853-1570

Fig. 18



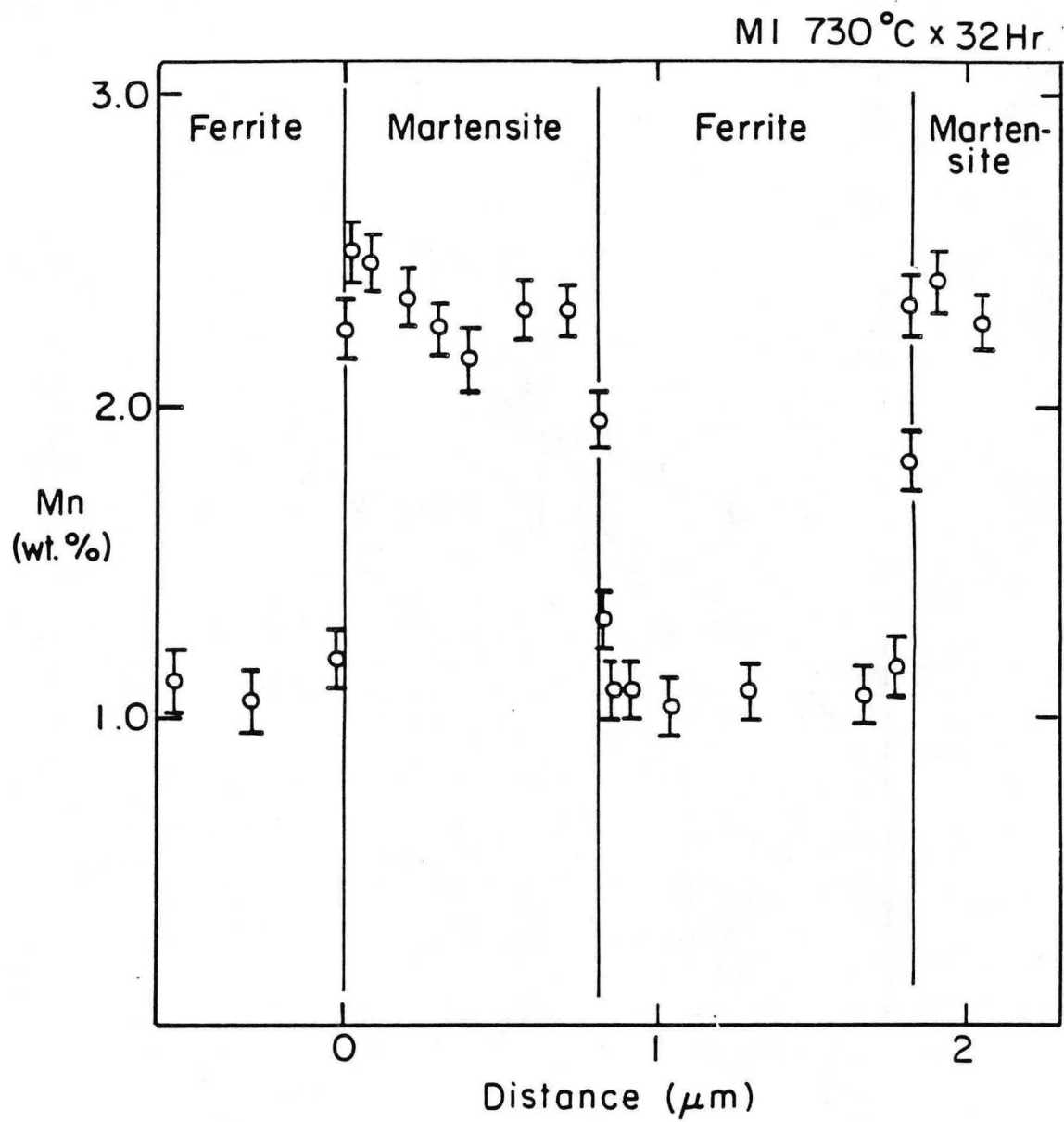
XBB 850-9420

Fig. 19



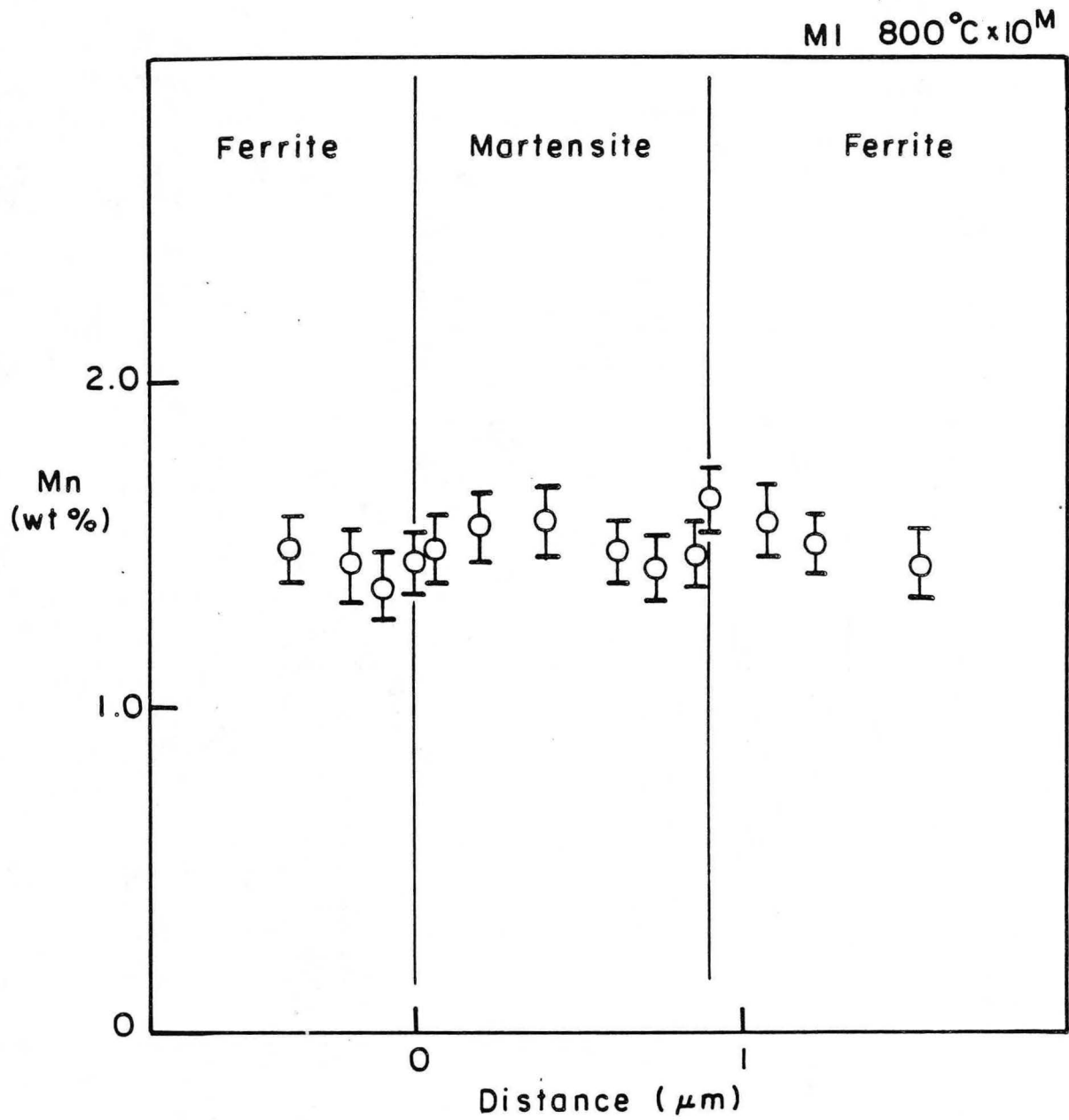
XBL 8510-6645

Fig. 20



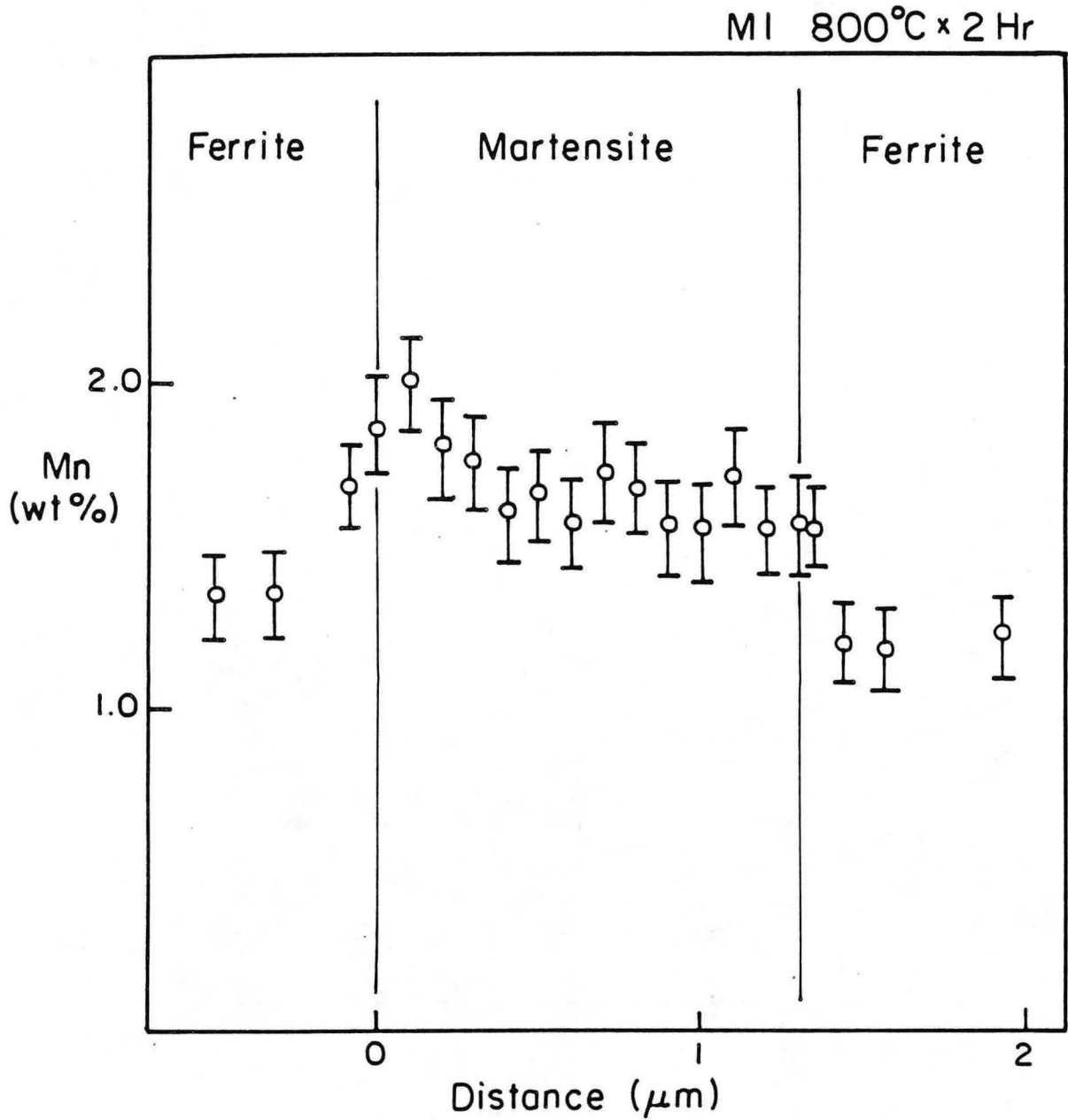
XBL8510-6644

Fig. 21



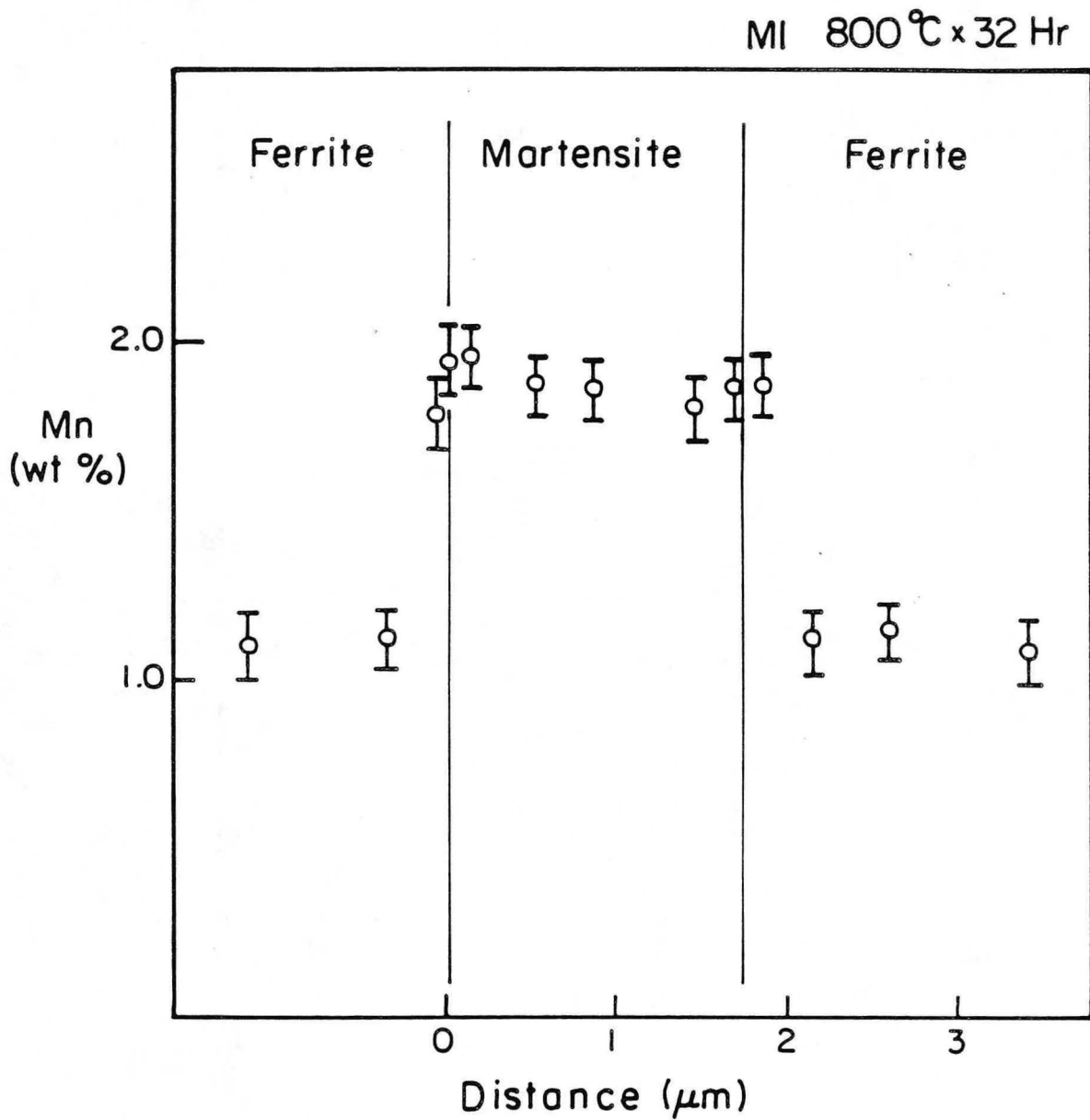
XBL 8511-6785

Fig. 22



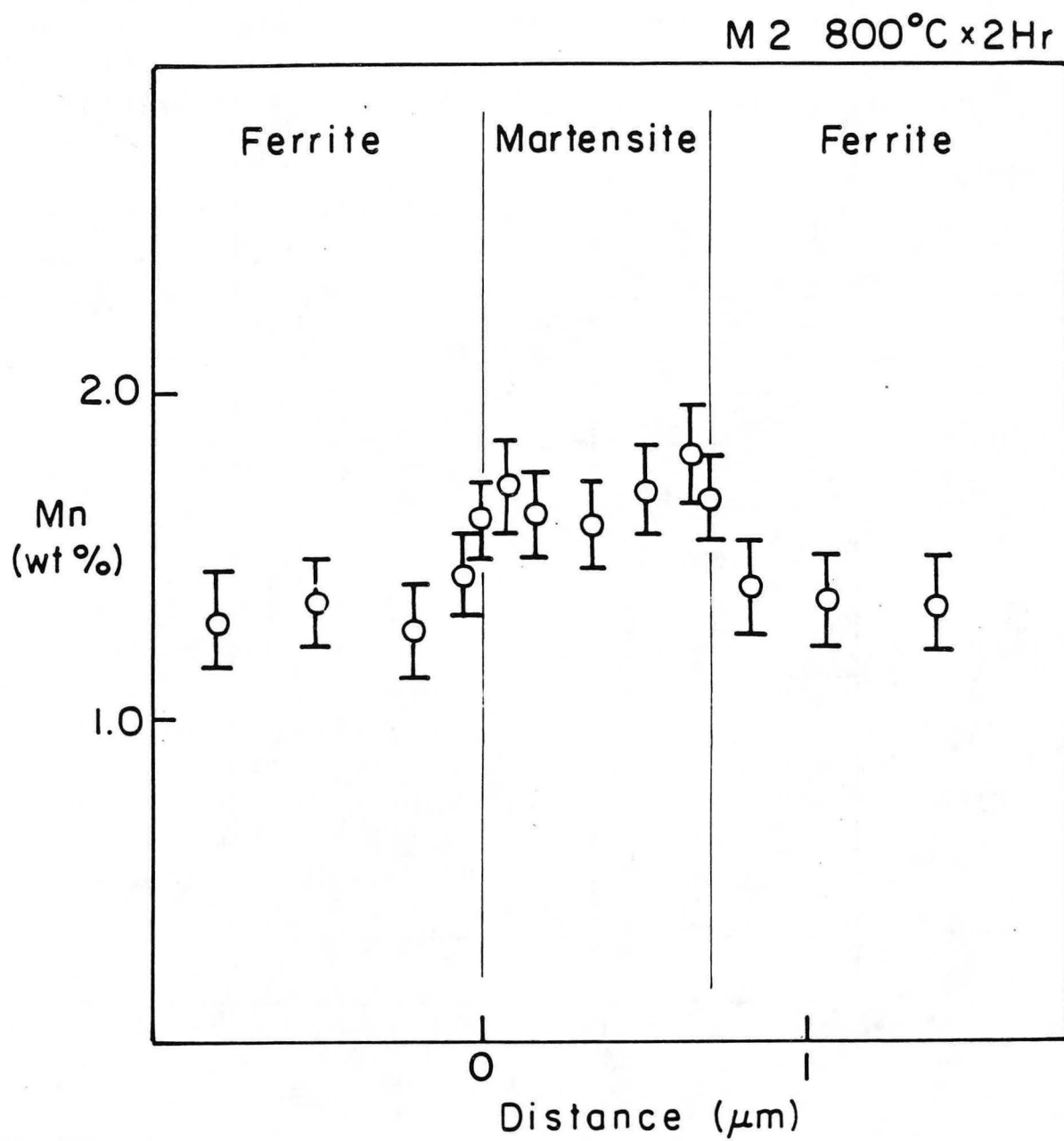
XBL 85 10-6669

Fig. 23



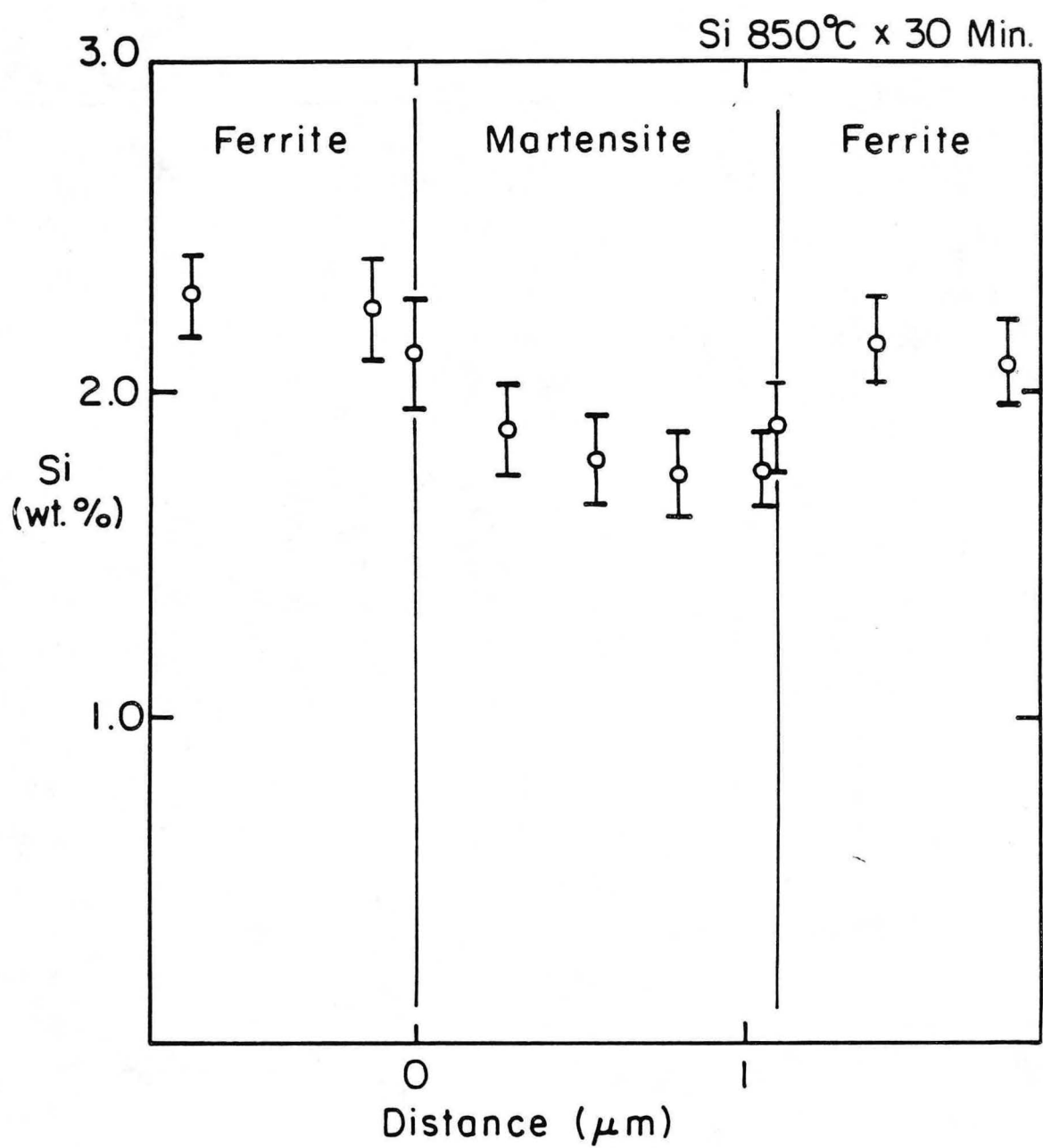
XBL 8510-6668

Fig. 24



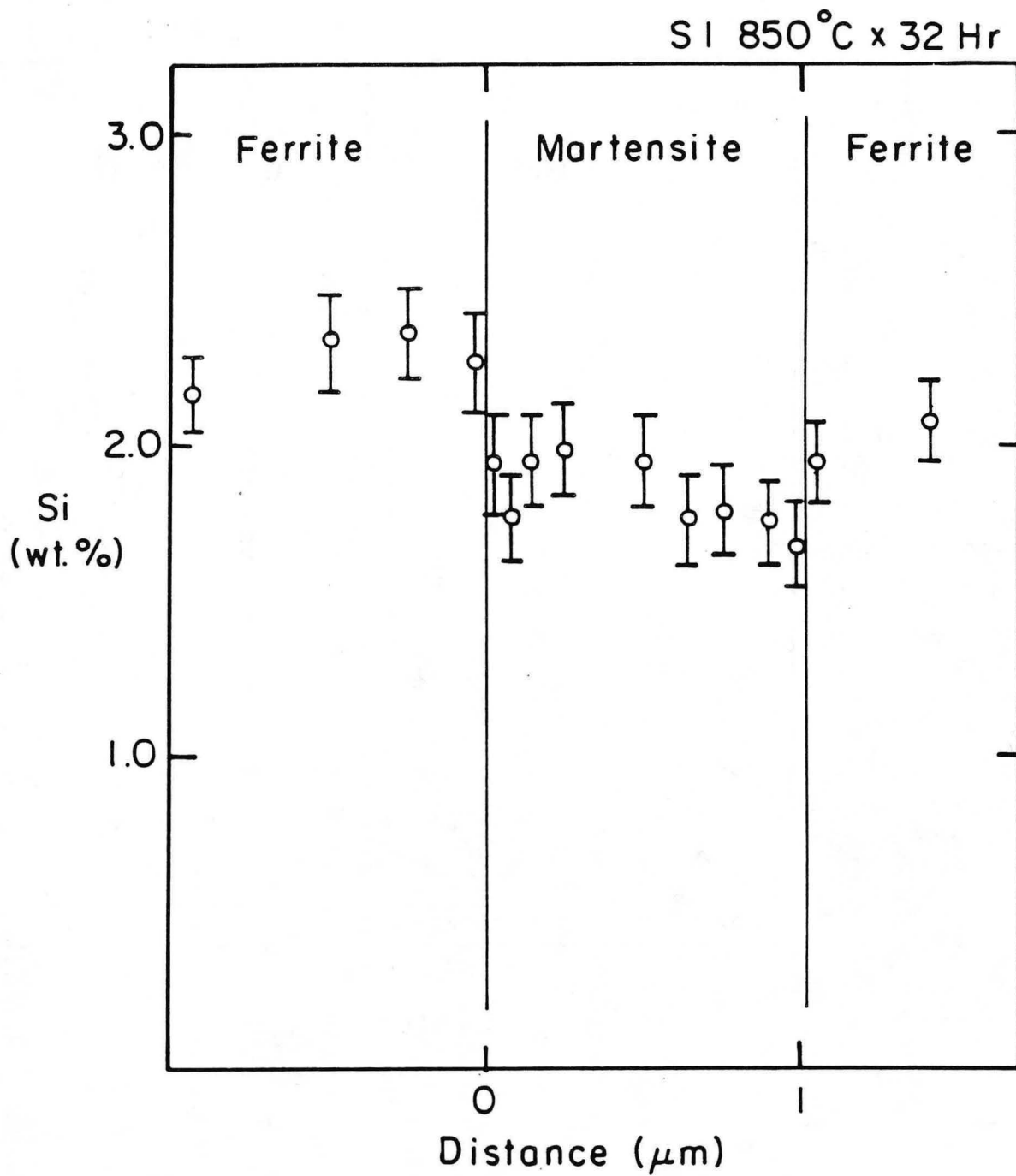
XBL 8511-6811

Fig. 25



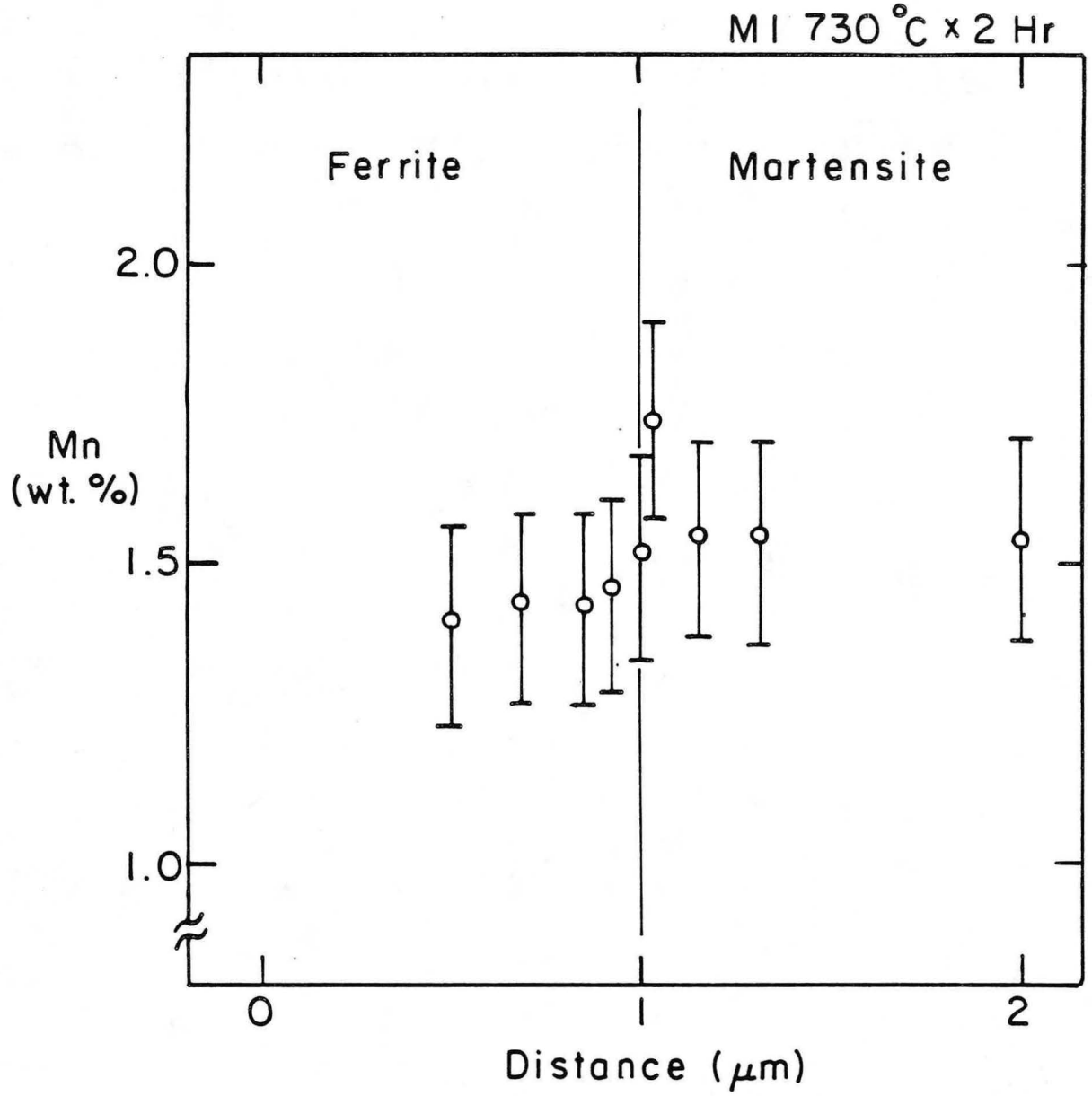
XBL8510-6643

Fig. 26



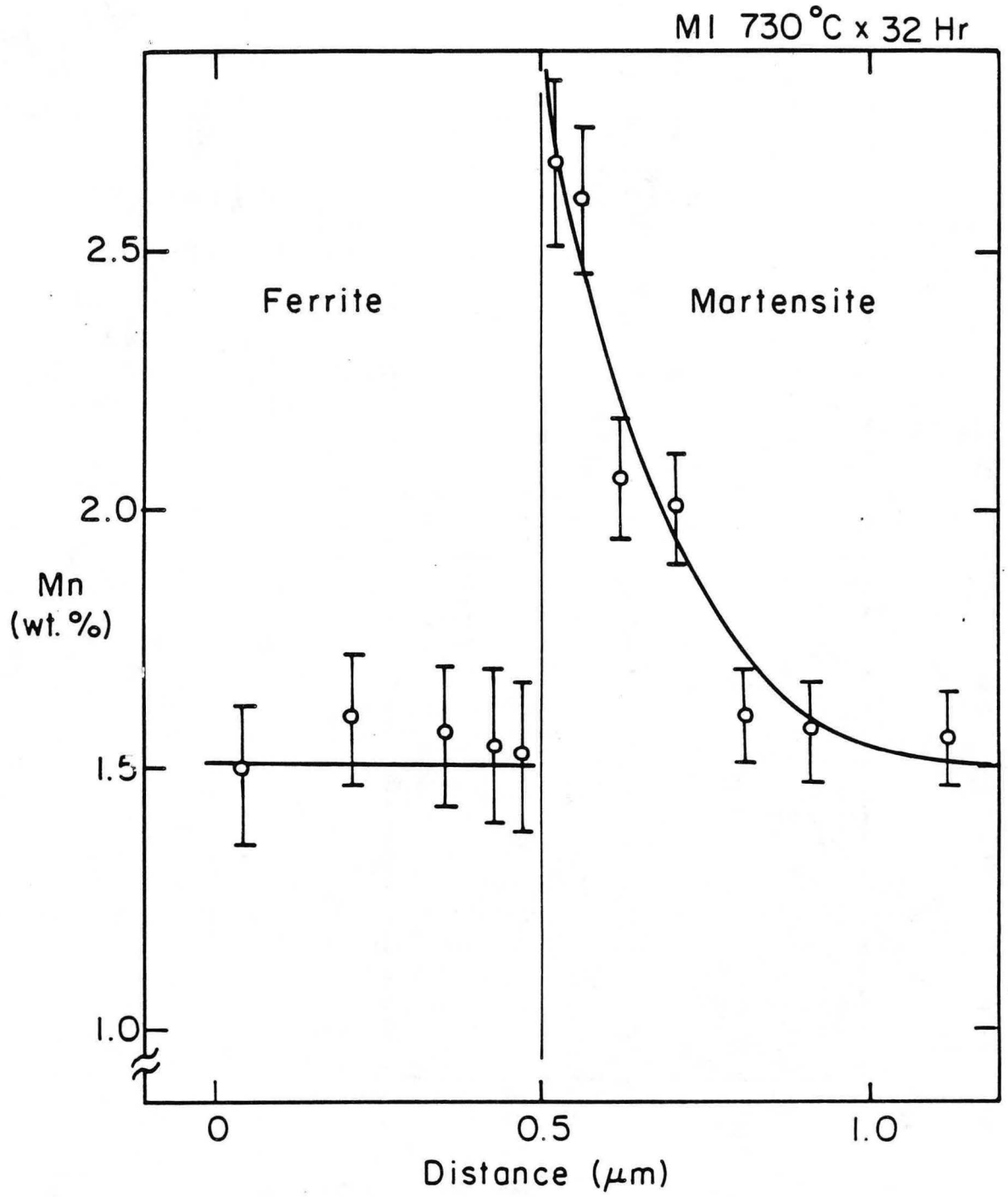
XBL 8510-6642

Fig. 27



XBL 8510-6641

Fig. 28



XBL8510-6640

Fig. 29

730°C x 2 Hr

Fe-Mn-Nb-C

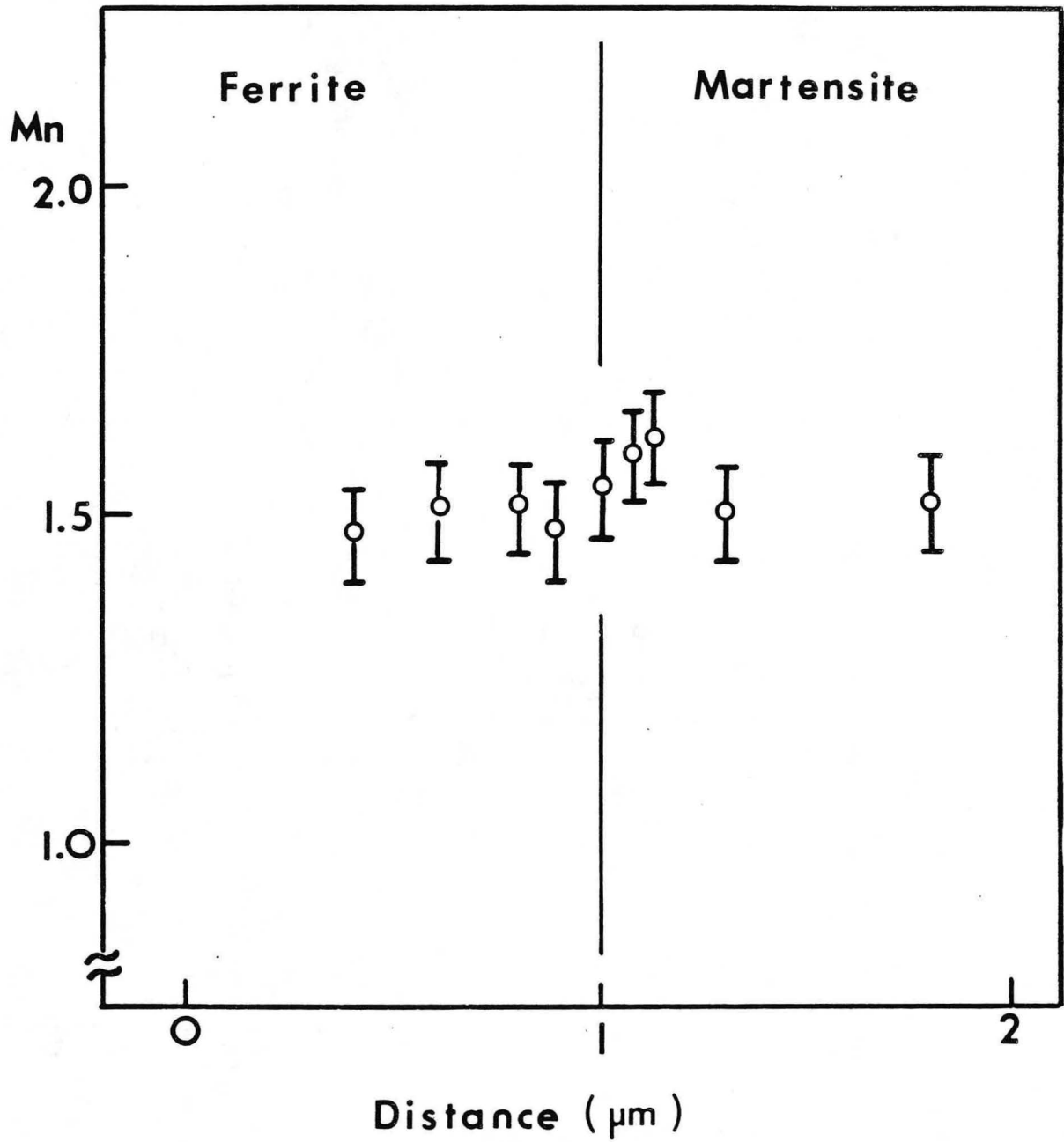
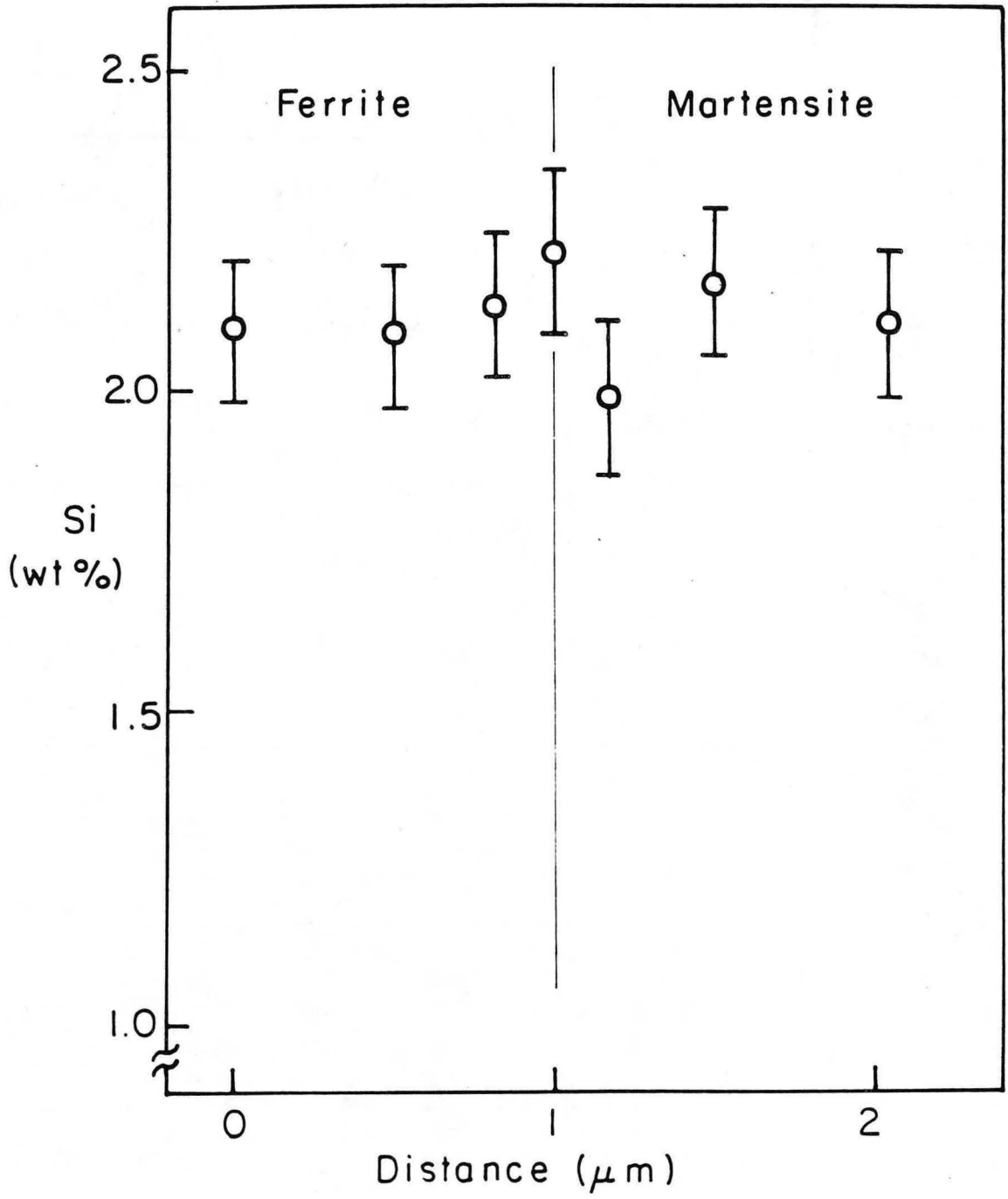


Fig. 30

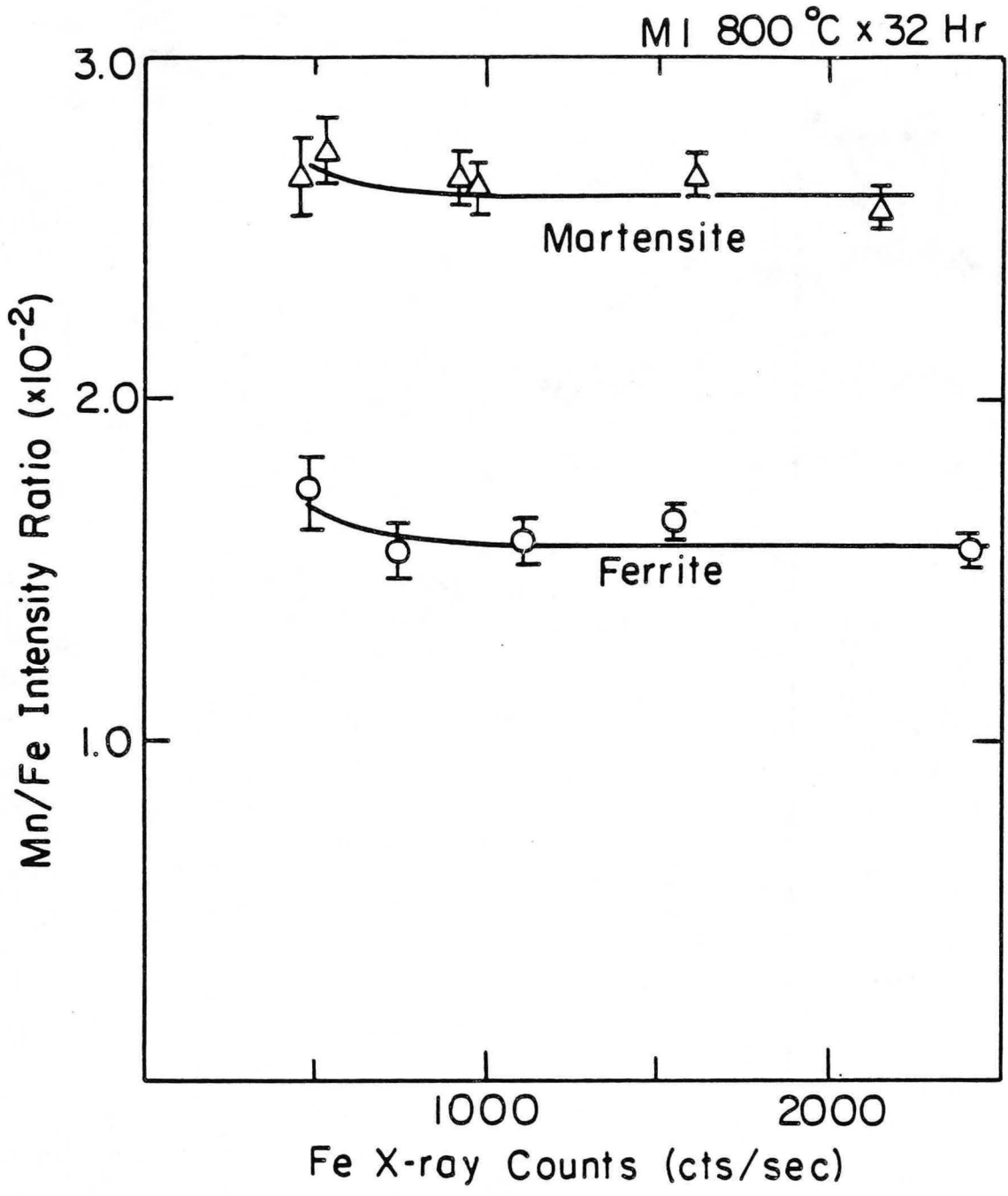
XBL 852-1348A

SI 850°C x 2 Hr



XBL 8511-6810

Fig. 31



XBL 8510-6648

Fig. 32

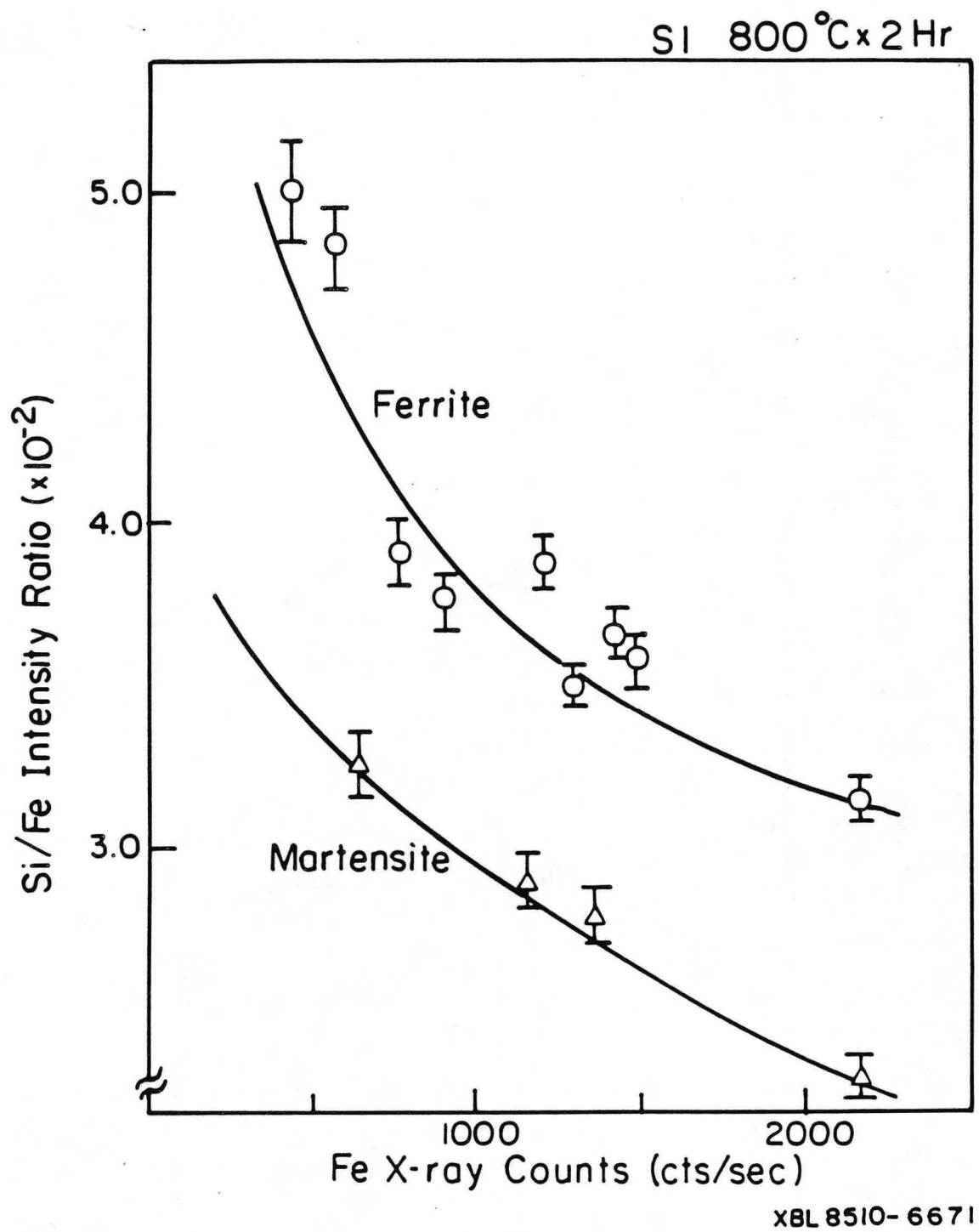
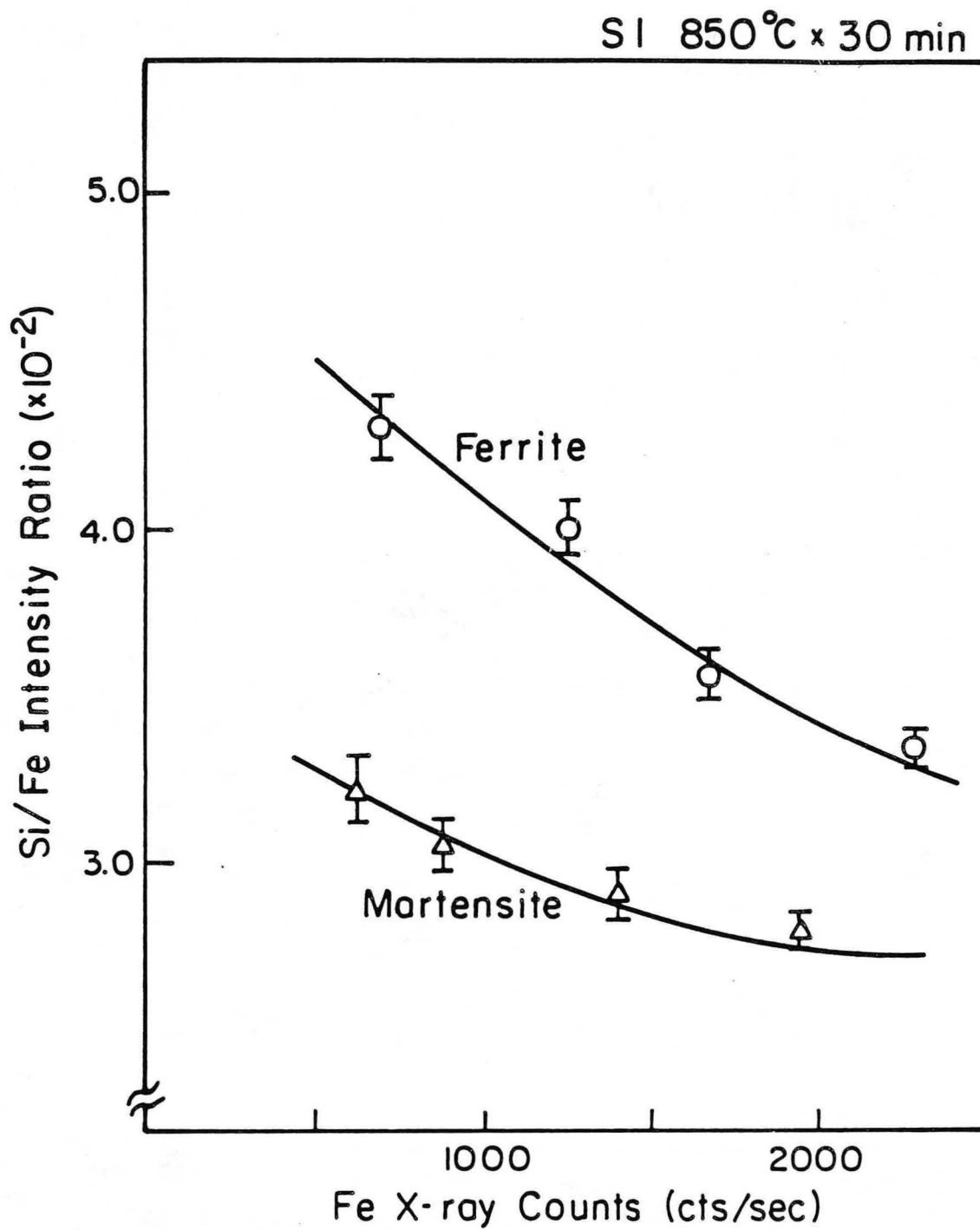


Fig. 33



XBL 8510-6672

Fig. 34

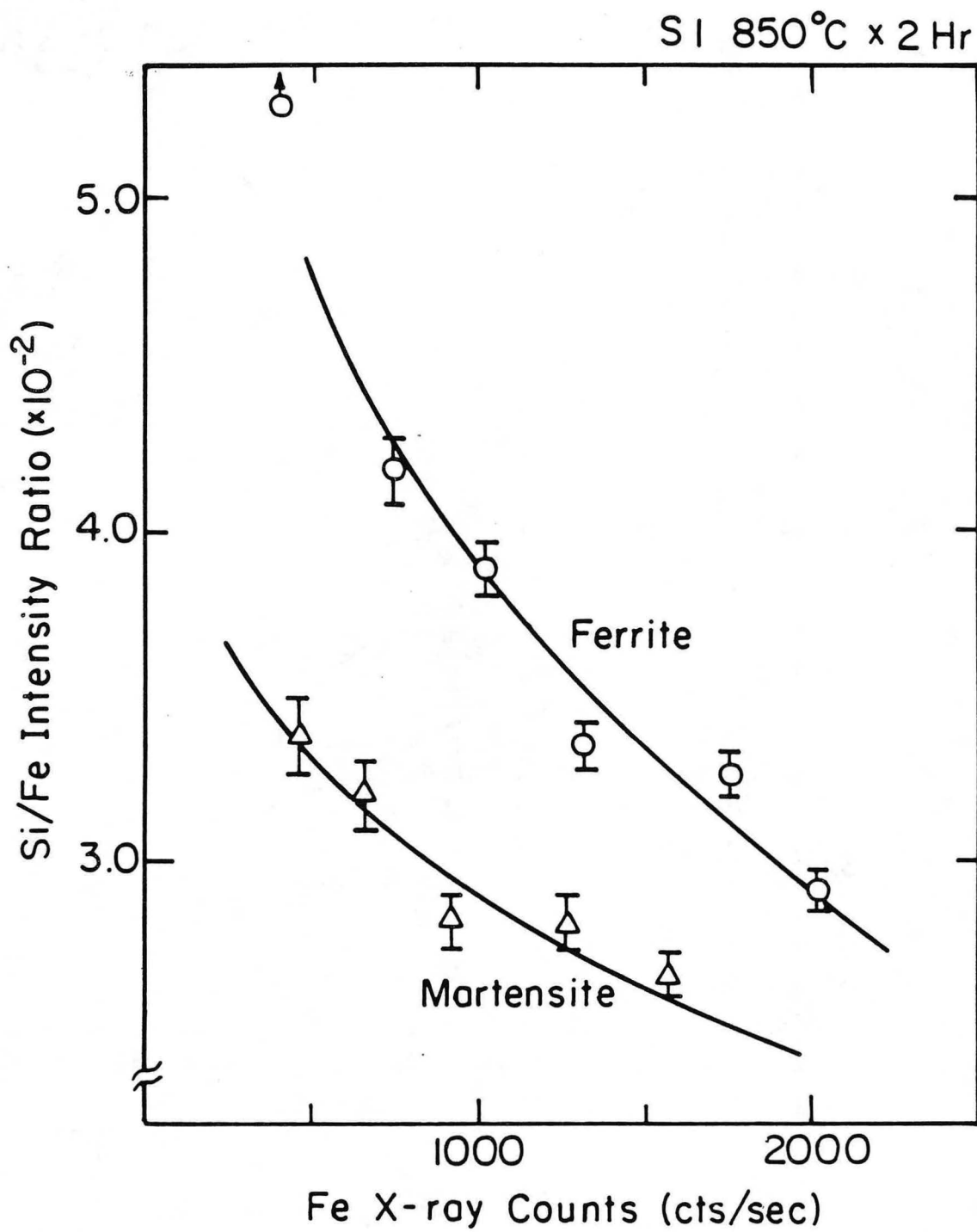
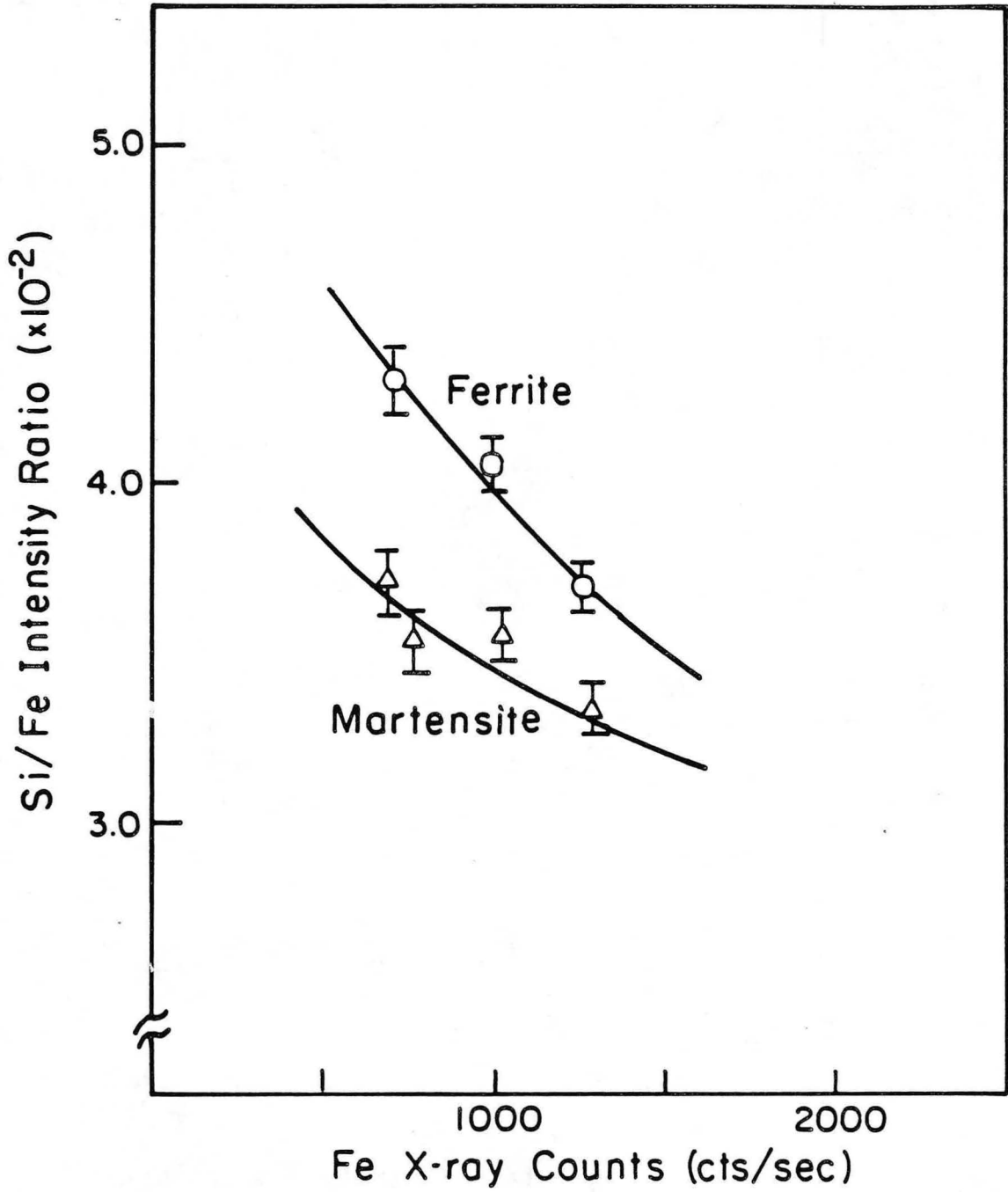


Fig. 35

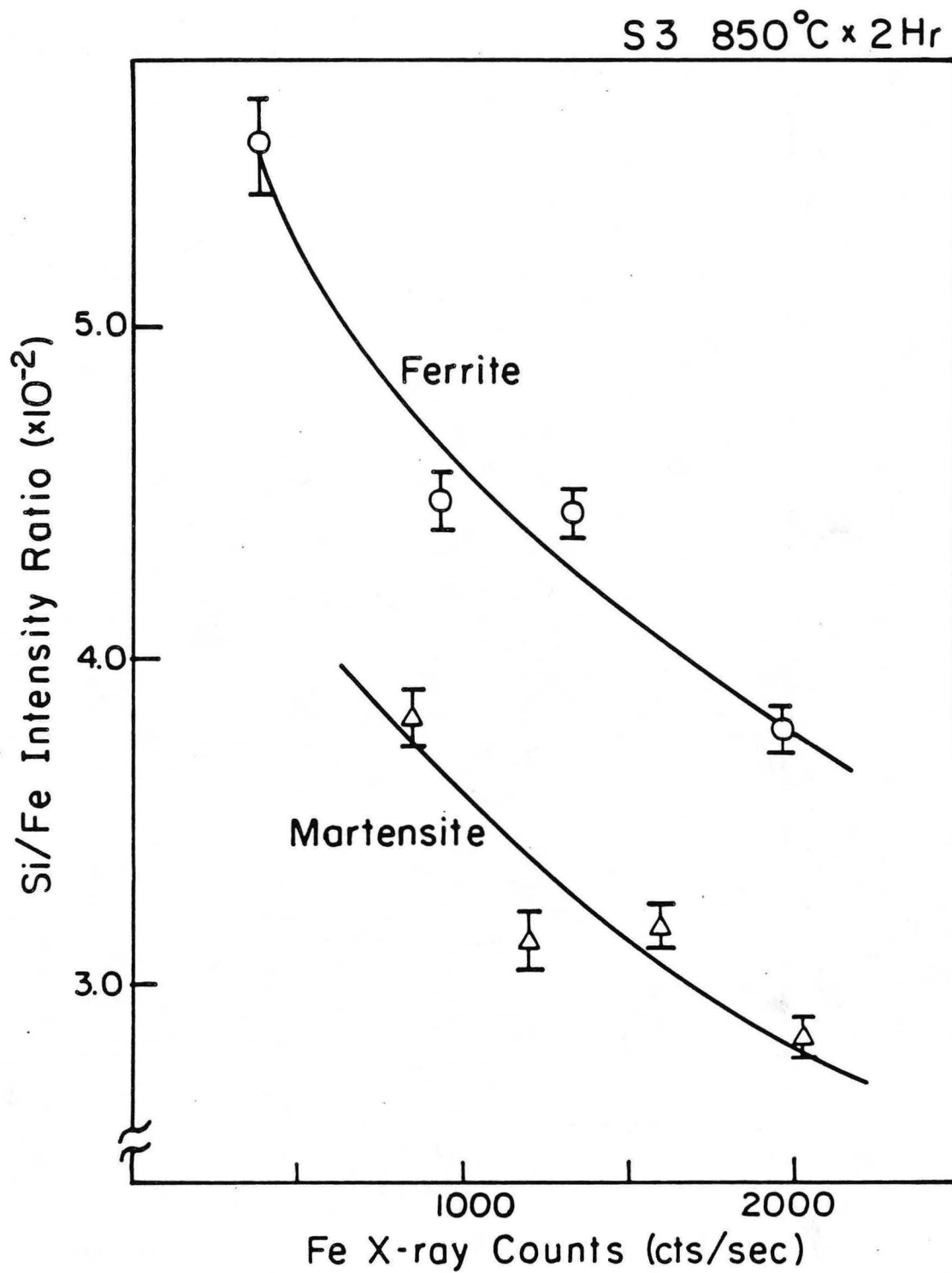
XBL 8510-6647

SI 930°C x 2 Hr



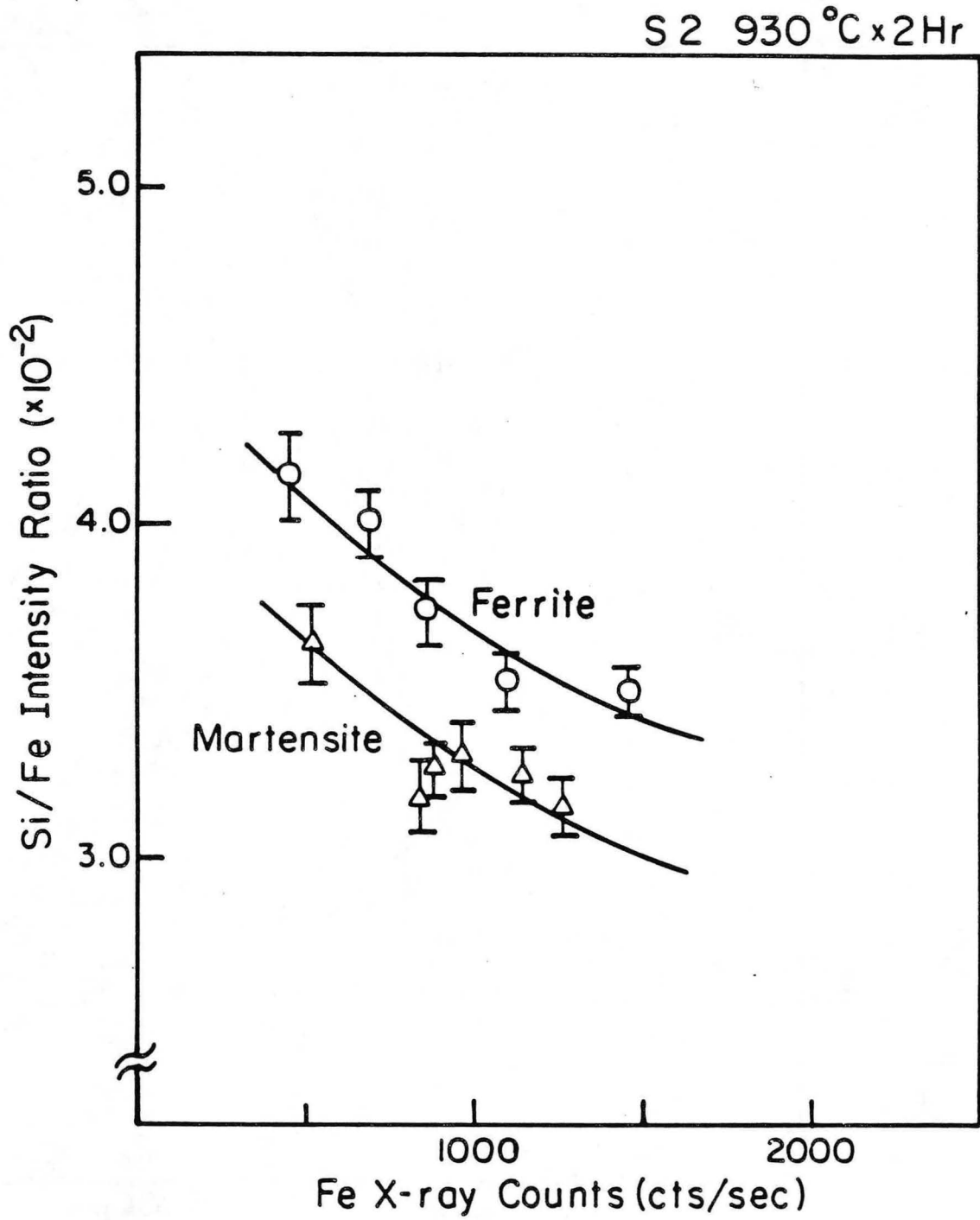
XBL 8510-6673

Fig. 36



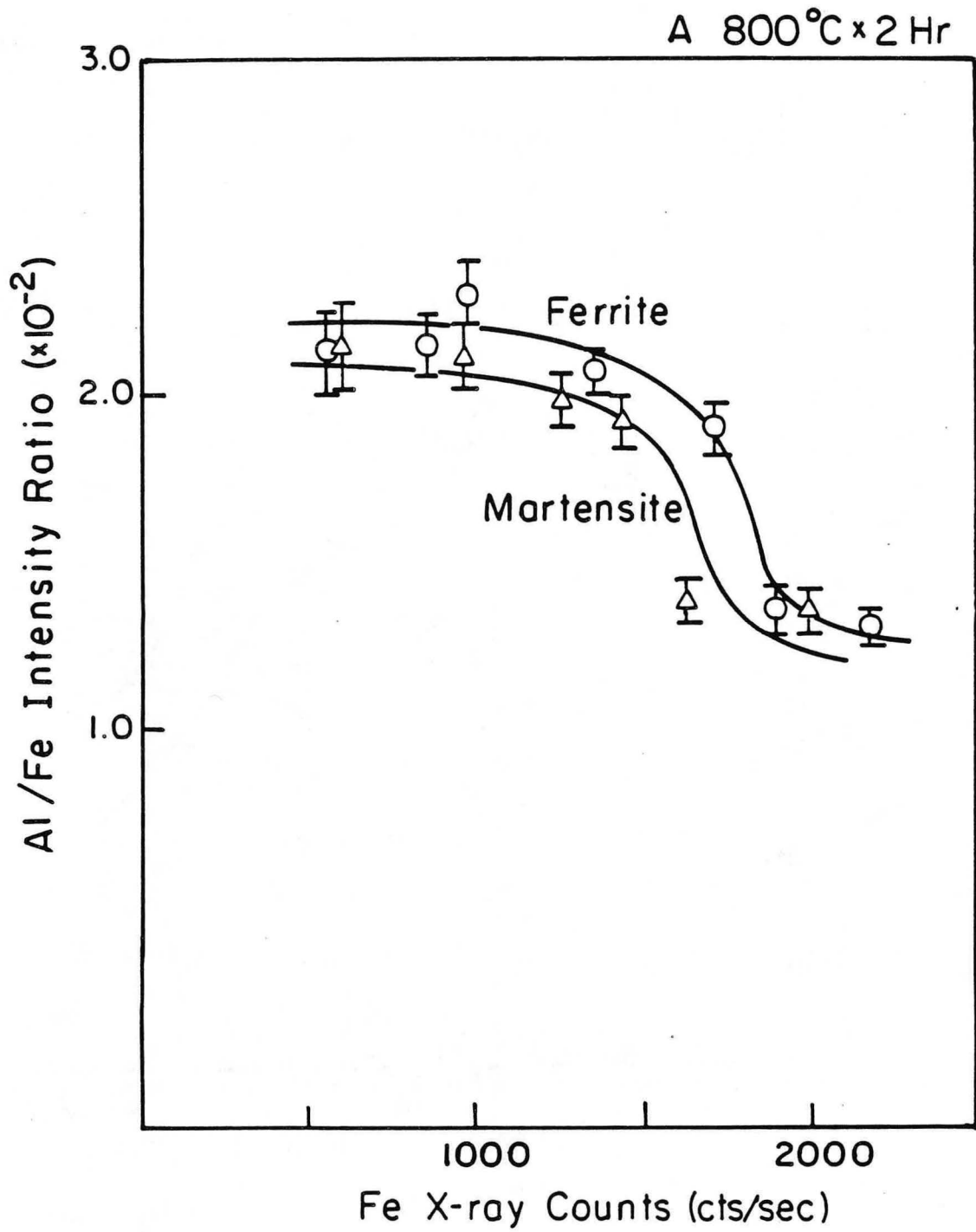
XBL 8510-6675

Fig. 37



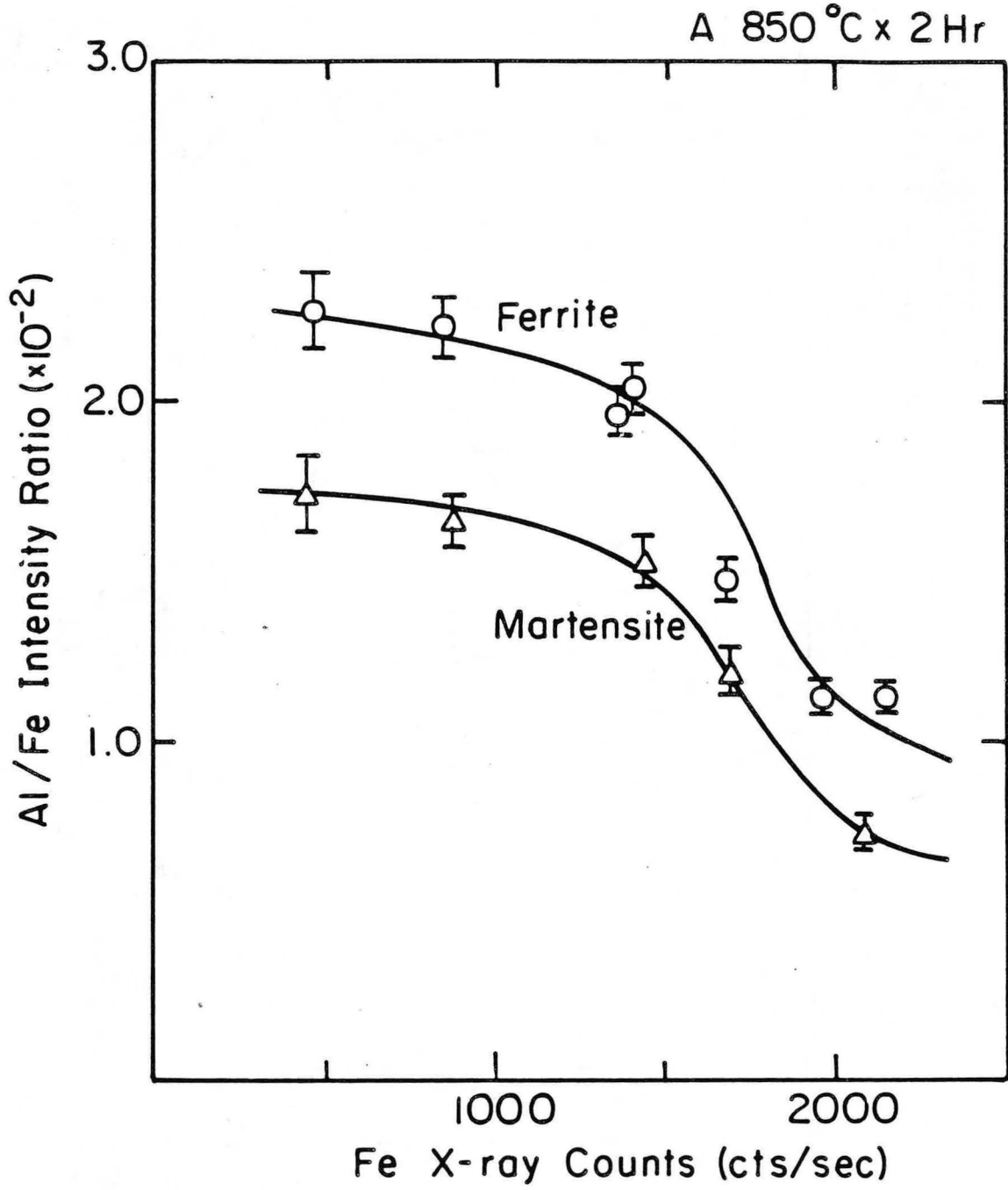
XBL 8510-6674

Fig. 38



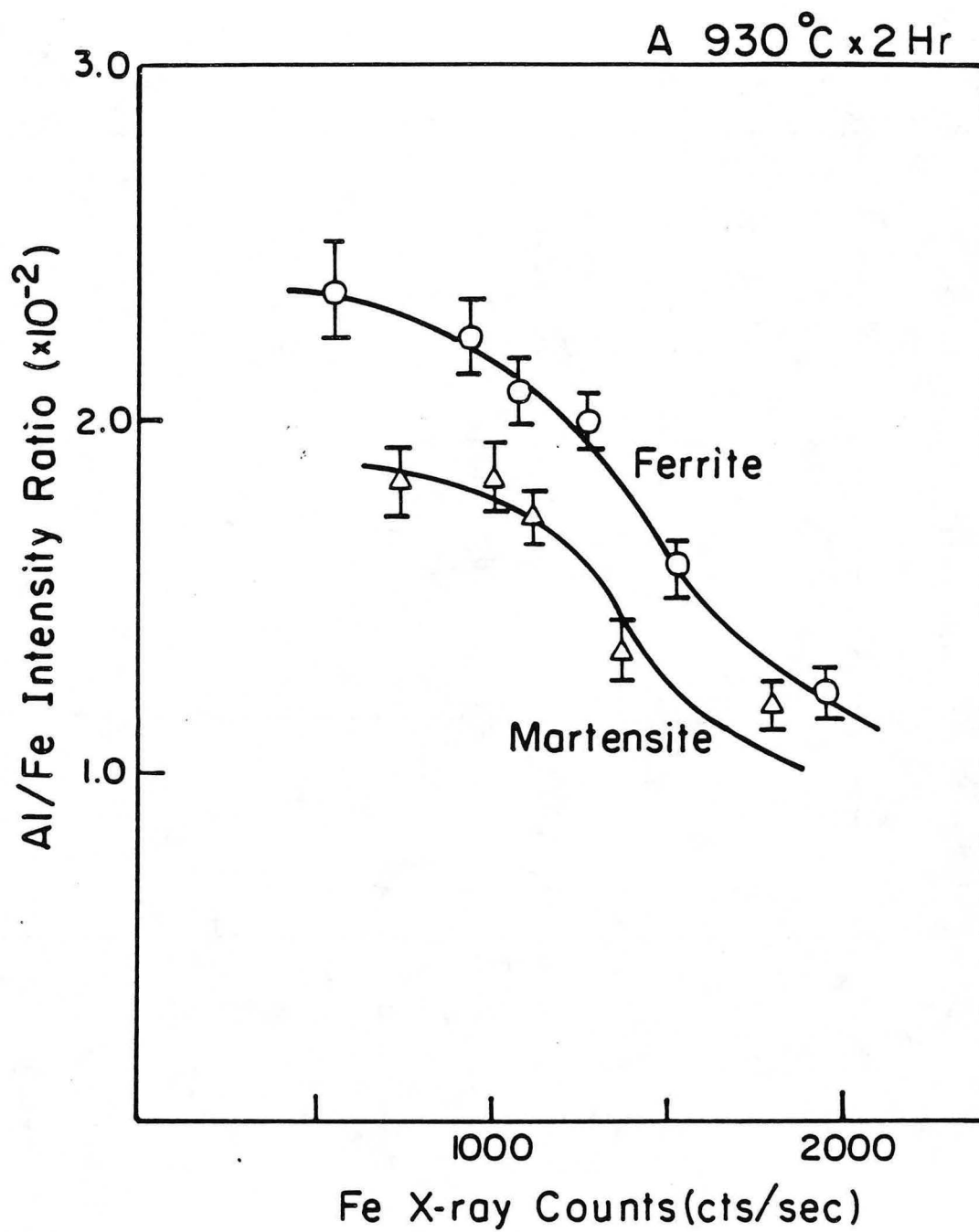
XBL8510-6670

Fig. 39



XBL8510-6646

Fig. 40



XBL 8510-6676

Fig. 41

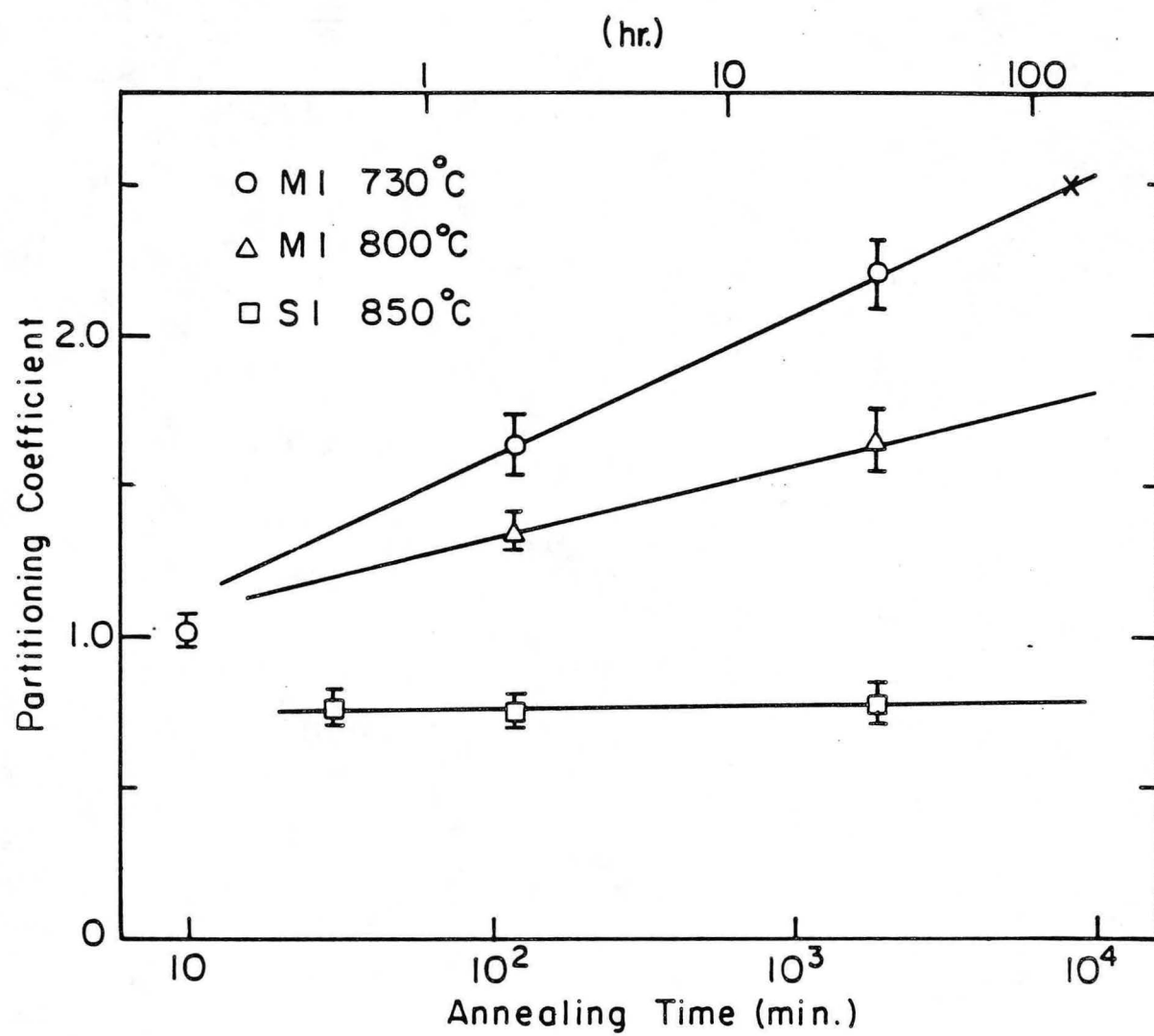
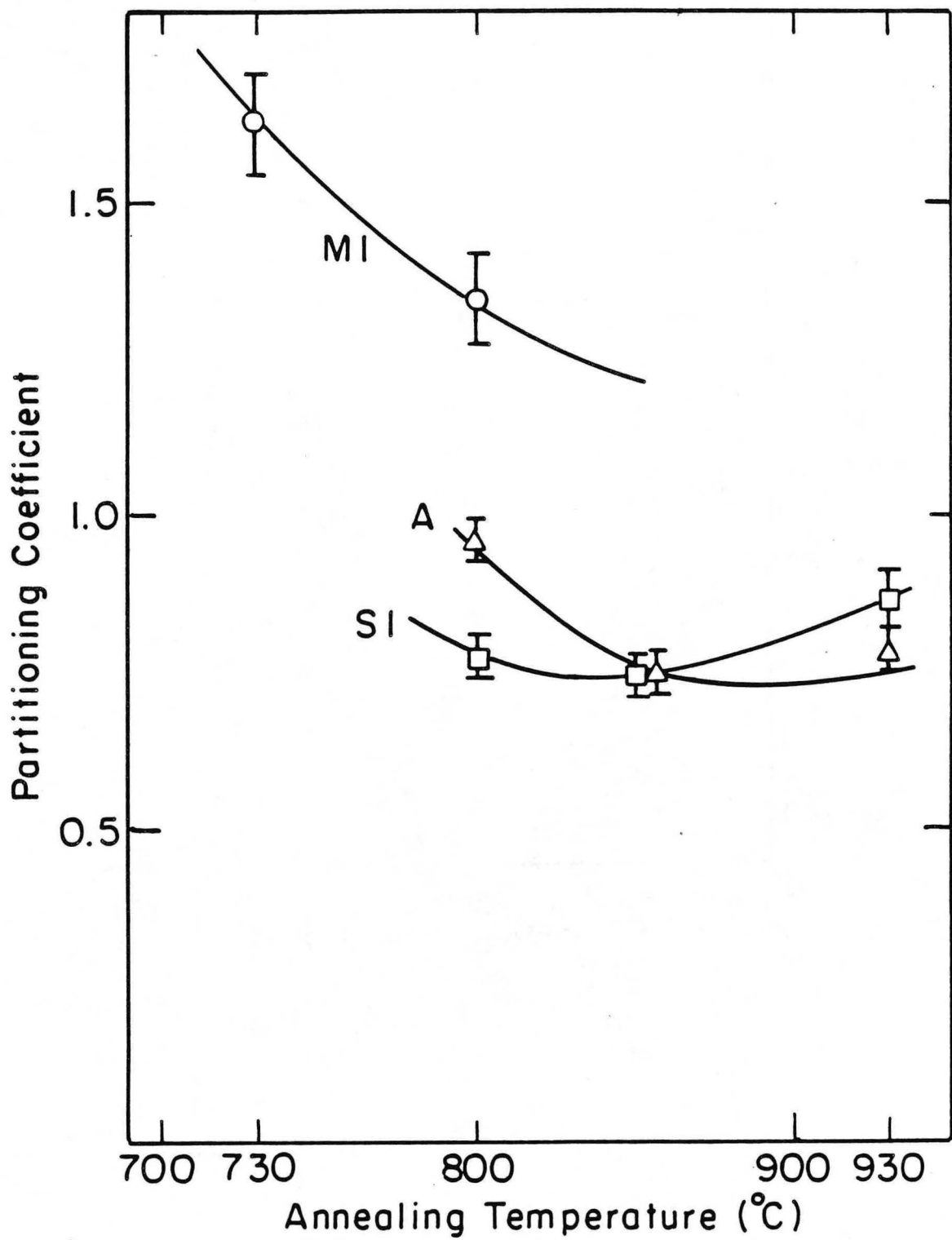


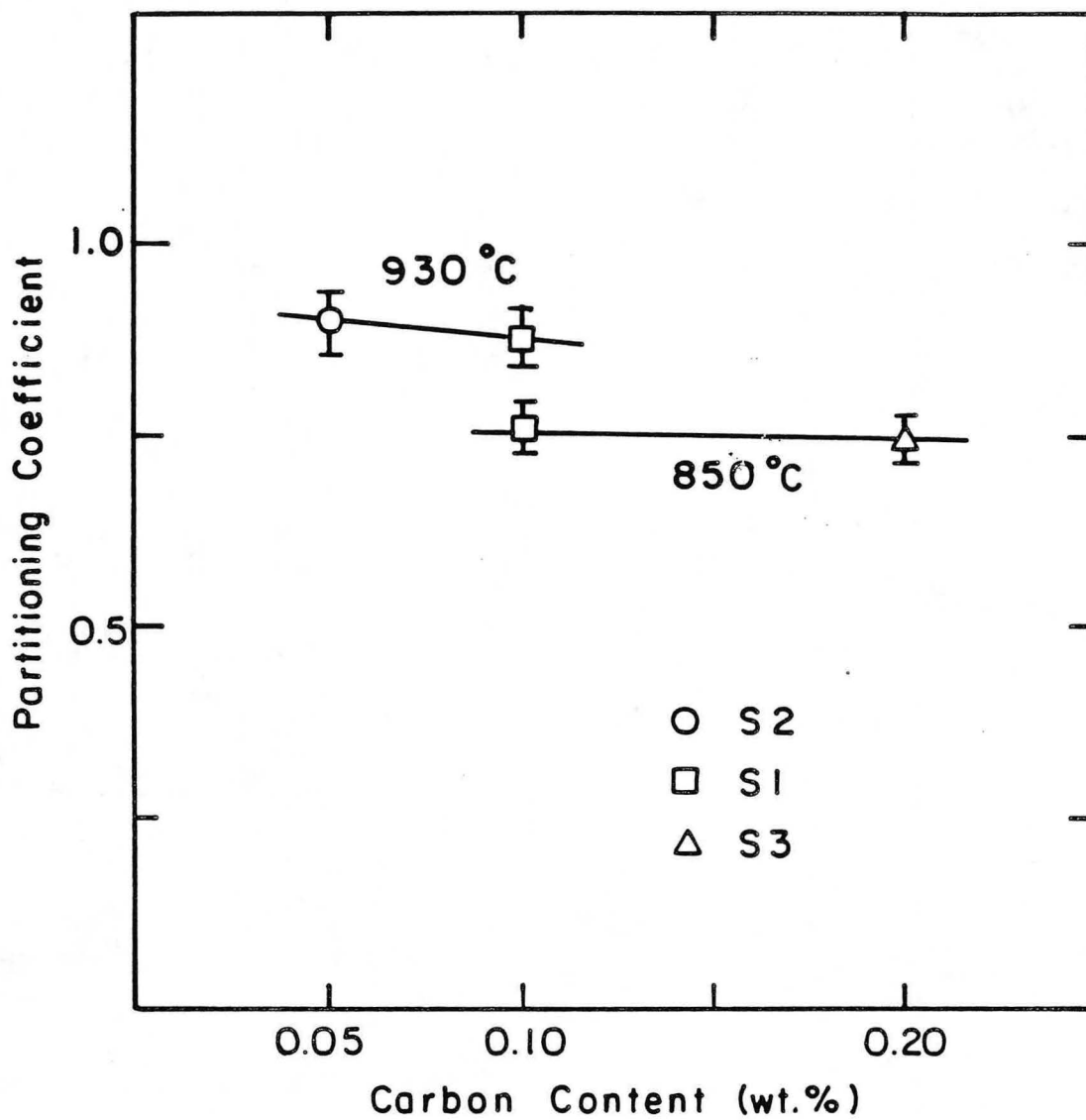
Fig. 42

XBL 8510-6638



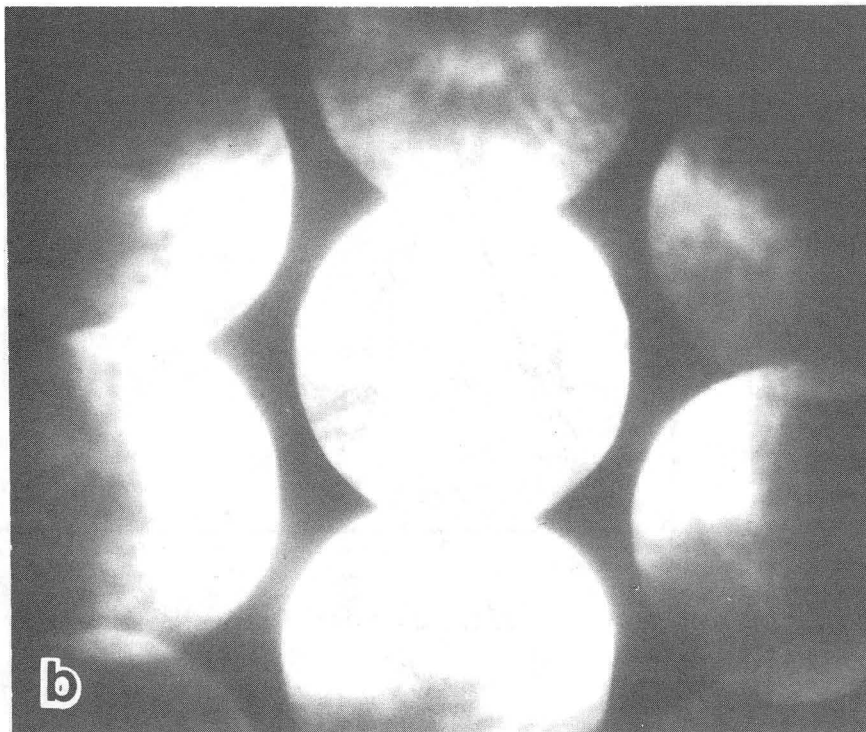
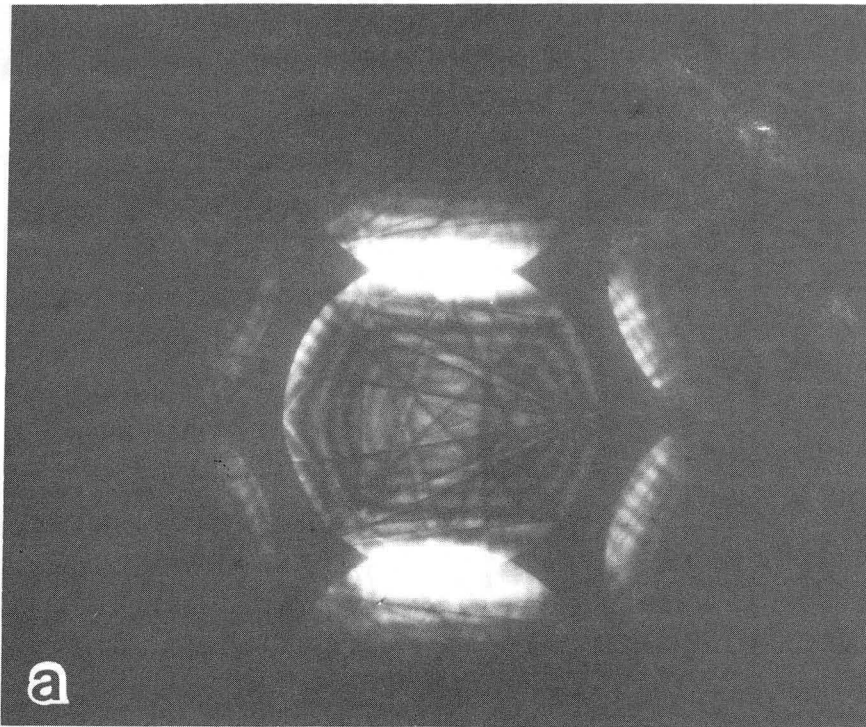
XBL 8510-6649

Fig. 43



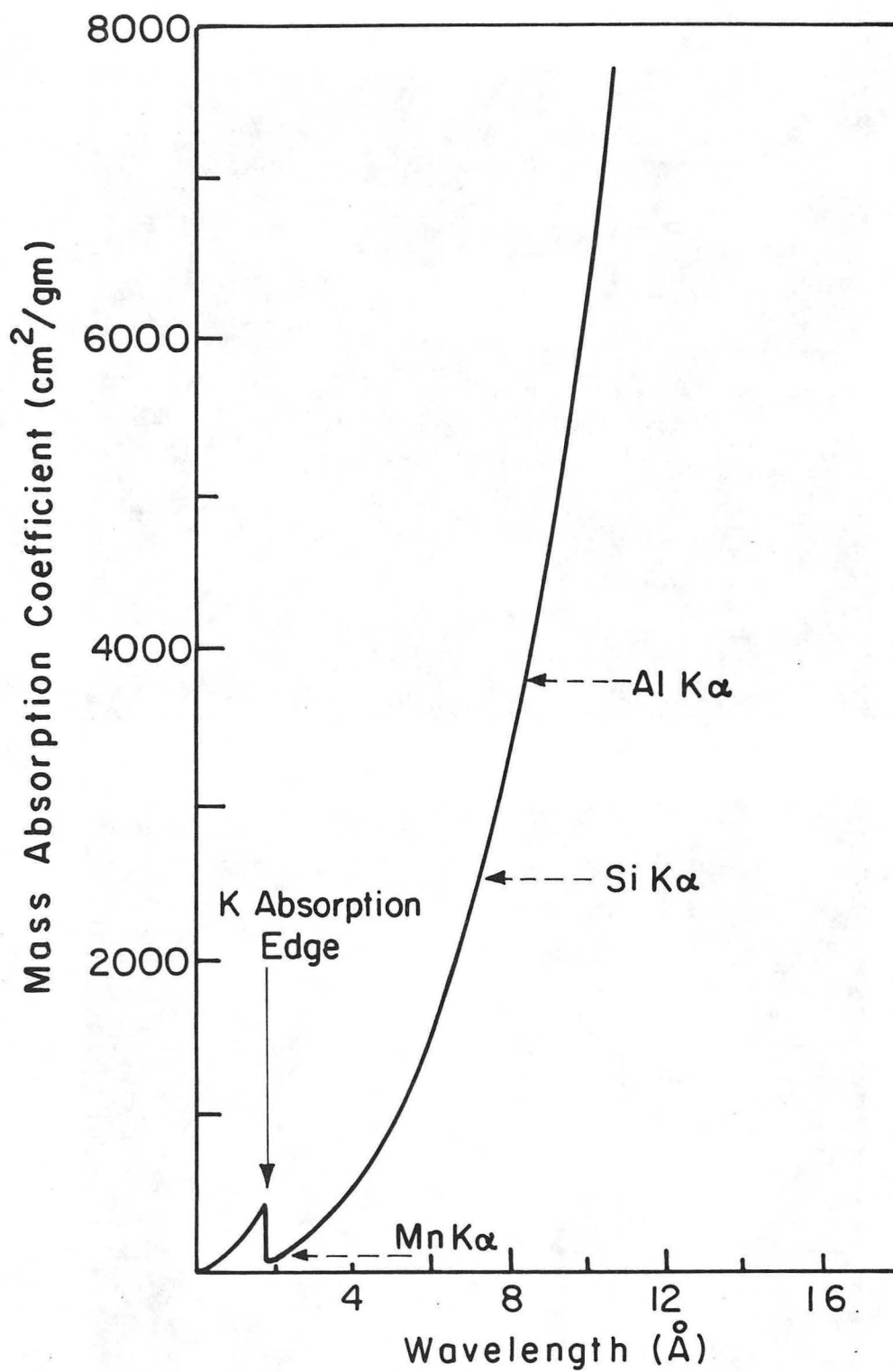
XBL 8510-6639

Fig. 44



XBB 850-9421

Fig. 45



XBL 8511-6812

Fig. 46

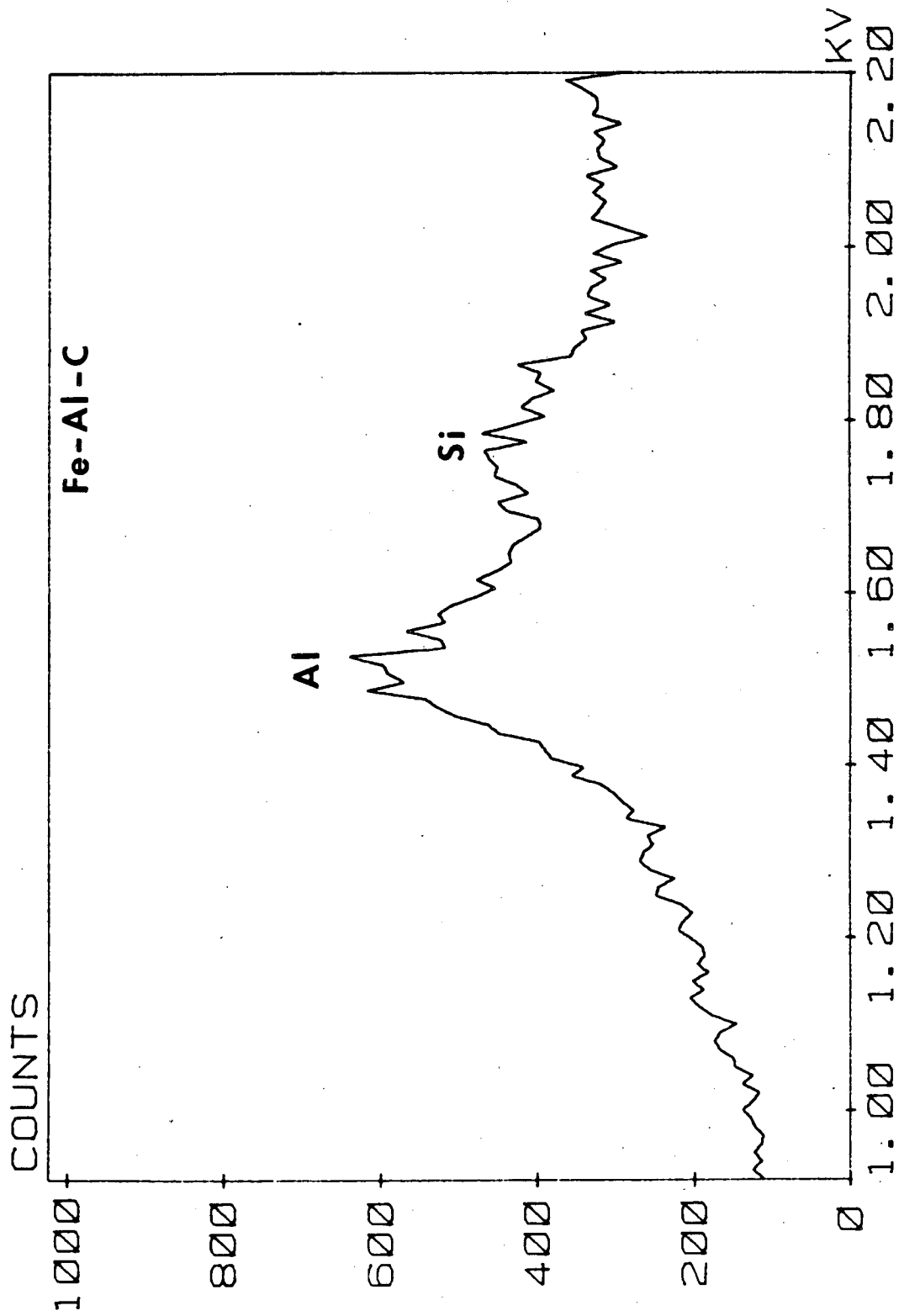
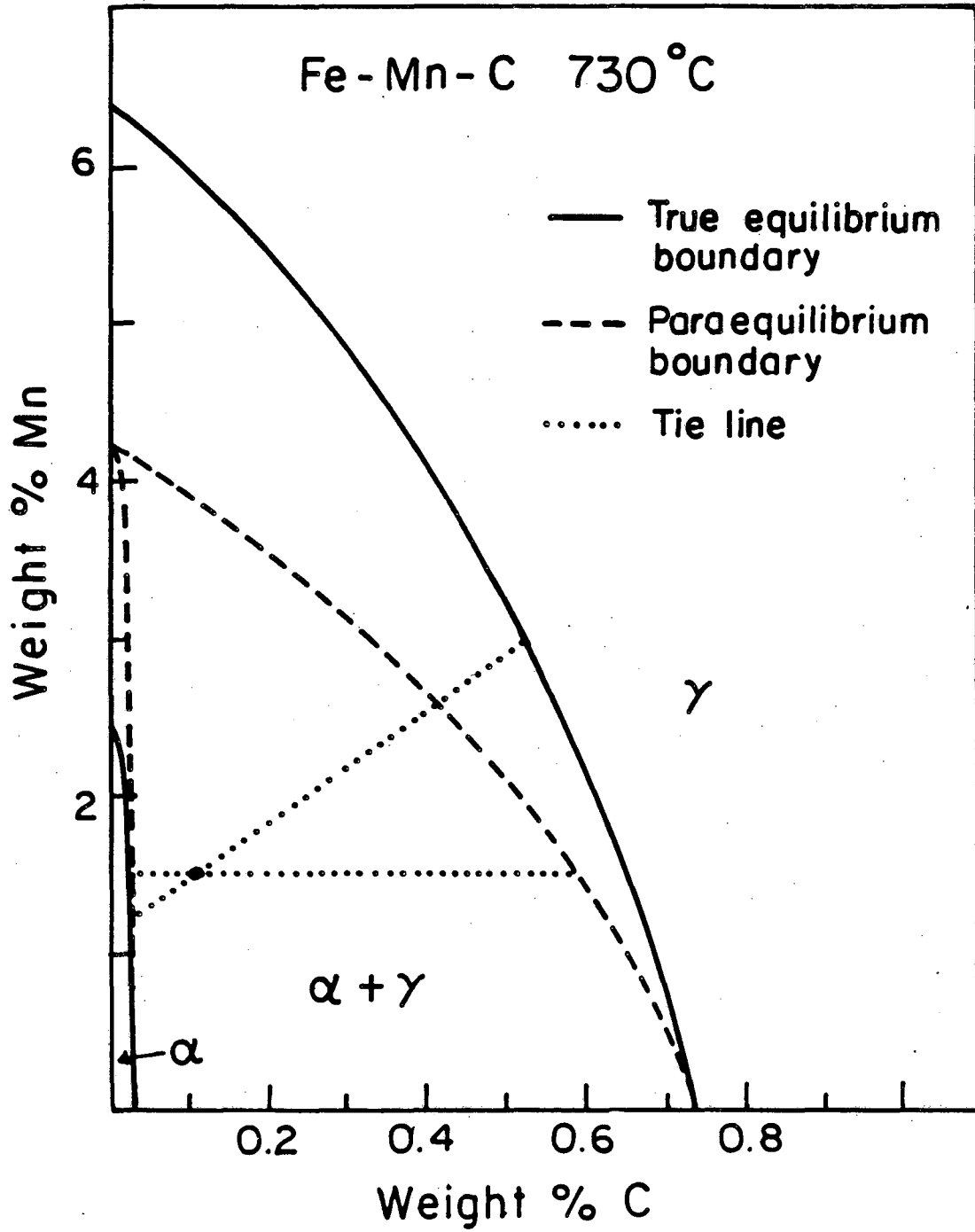


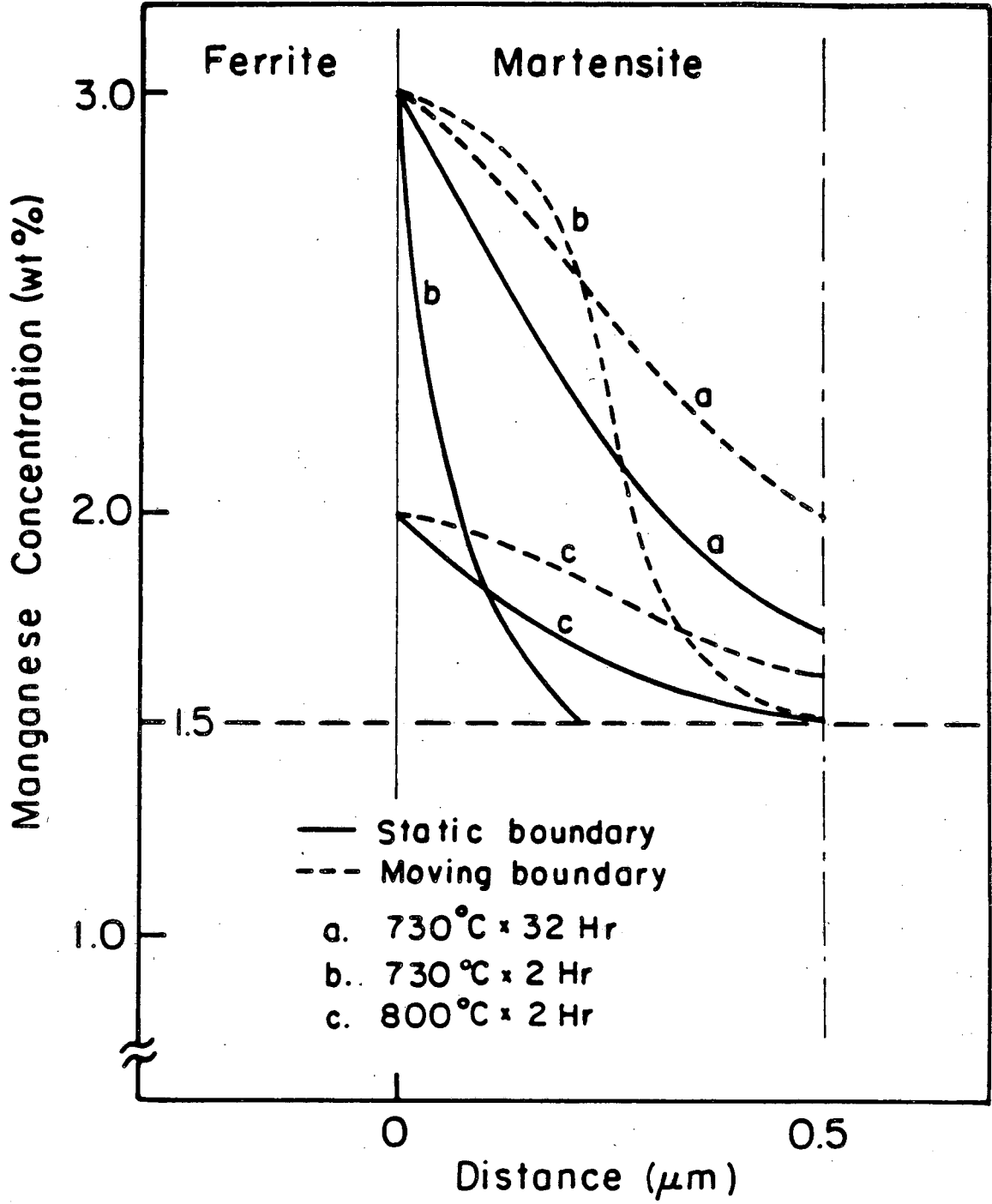
Fig. 47

XBL 8510-4212



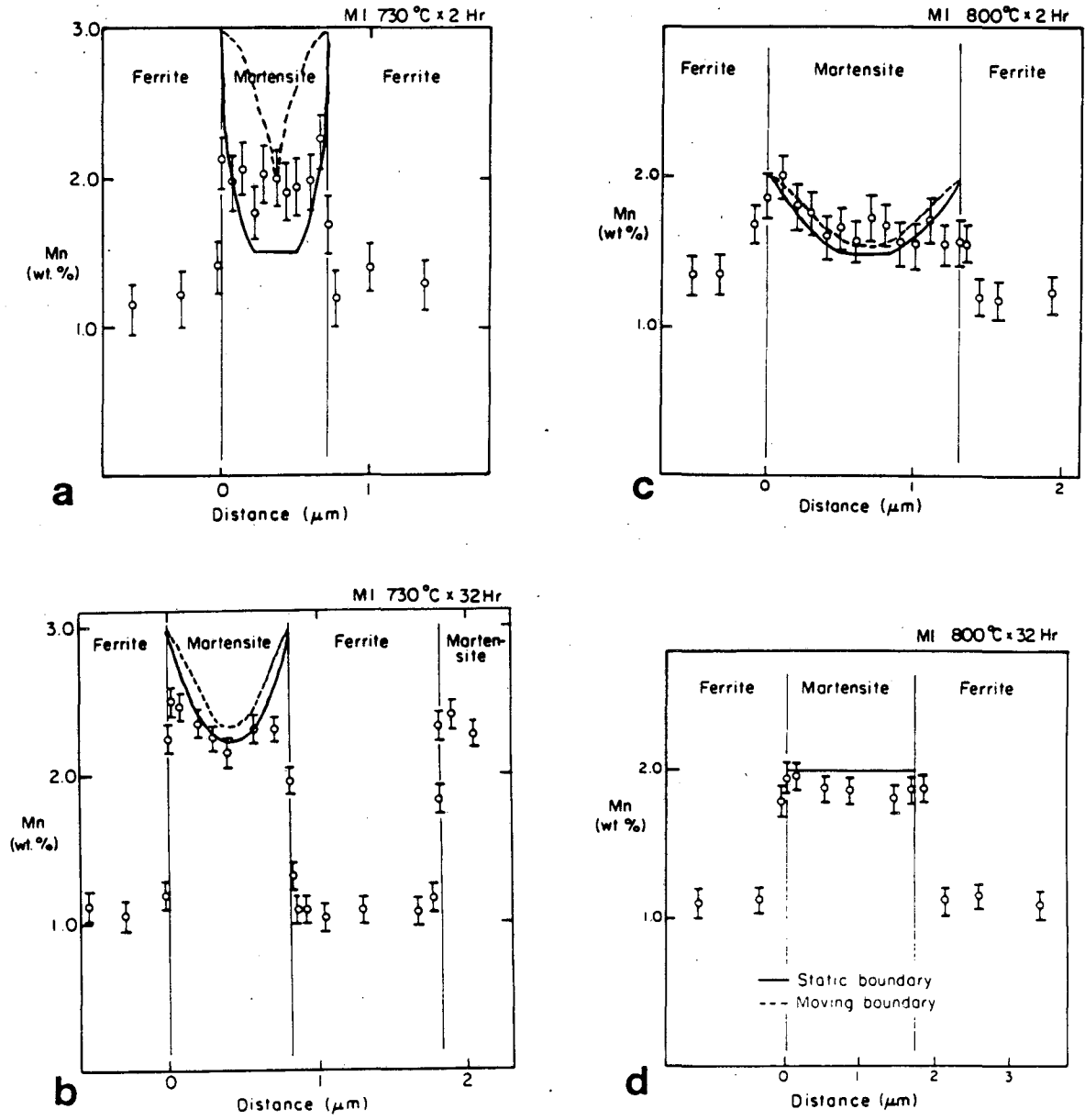
XBL 8510-6636

Fig. 48



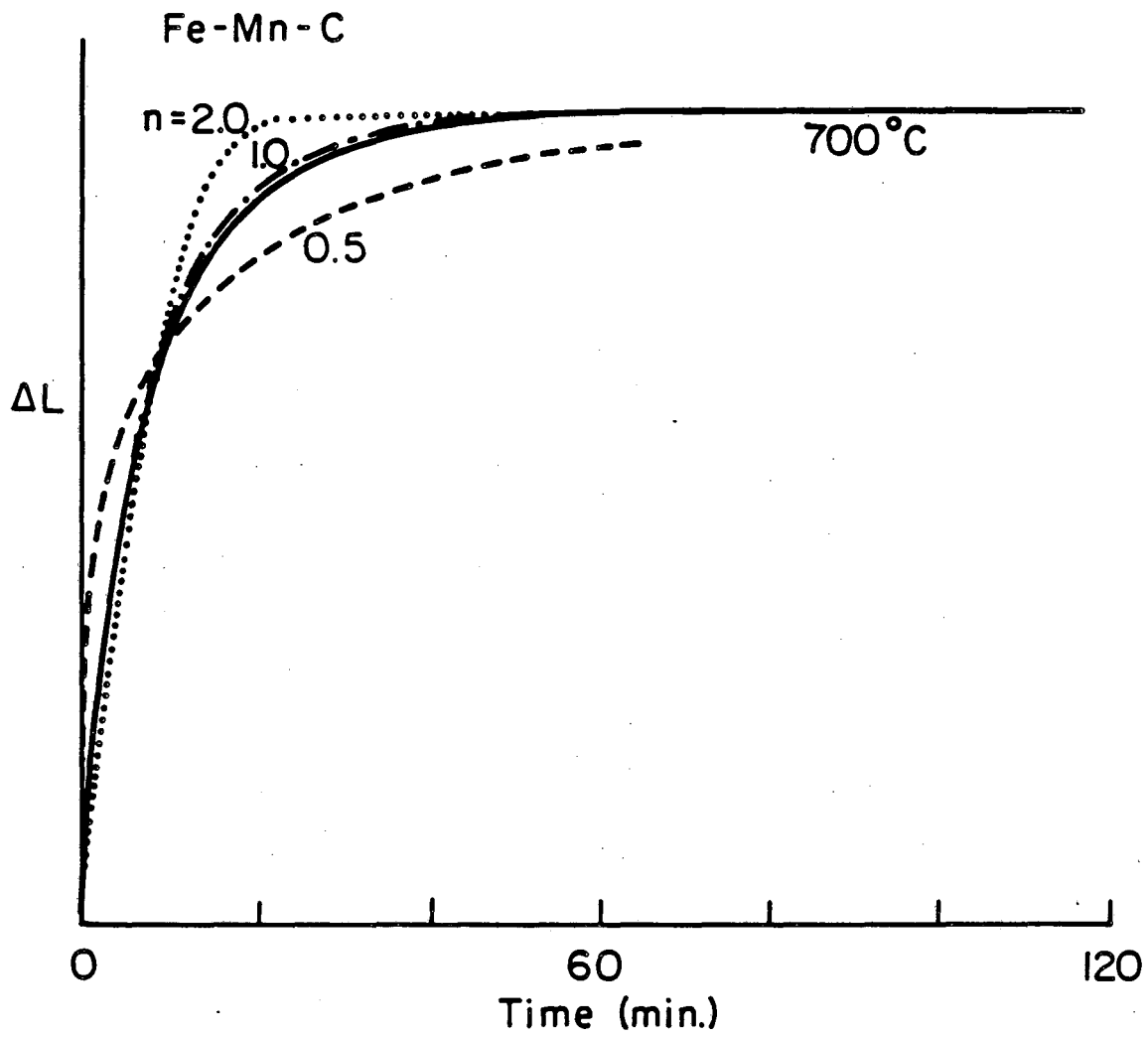
XBL 8511-6 813

Fig. 50



XBL 8510-6648B

Fig. 51

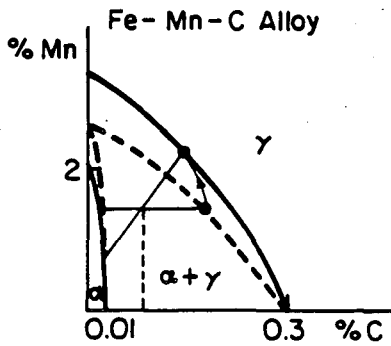


XBL 8510-6635

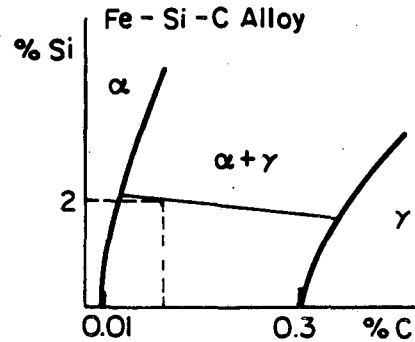
Fig. 52

Austenite Nucleation and Growth and Solute Partitioning

(Starting Microstructure: lath martensite)

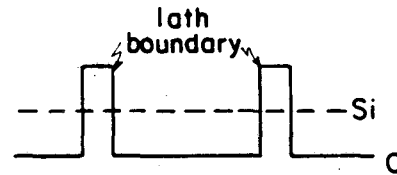
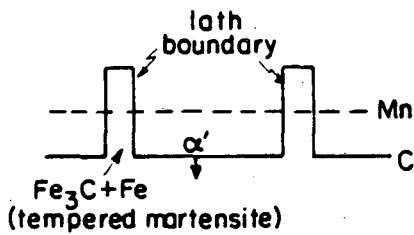


Isotherm diagrams of Fe-Mn-C system at 800°C

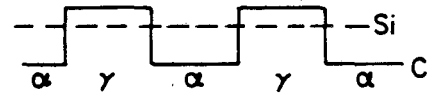
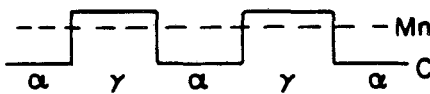


Isotherm diagrams of Fe-Si-C system at 800°C

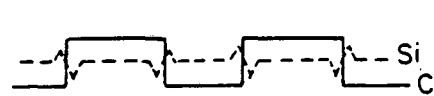
I. Nucleation of austenite



2. Austenite growth



3. Substitutional elements diffusion



4. Final equilibrium

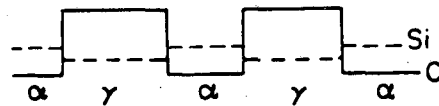
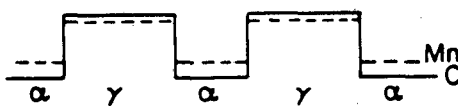


Fig. 53

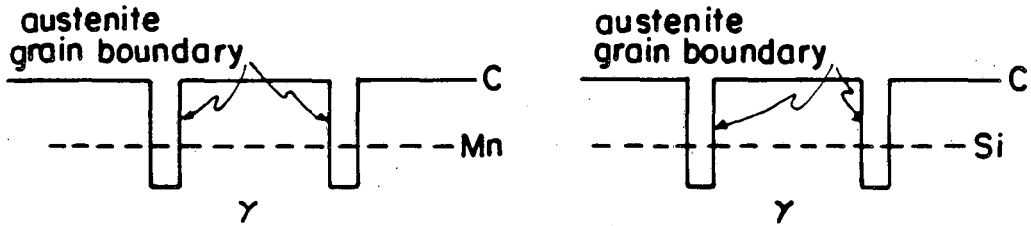
XBL8311-65888

Ferrite Nucleation and Growth and Solute Partitioning
(Step Cooling)

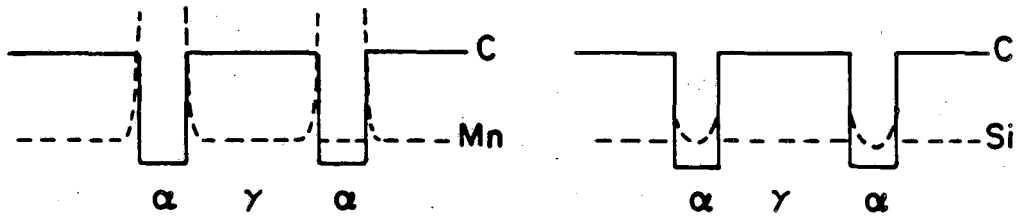
Fe - Mn - C Alloy

Fe - Si - C Alloy

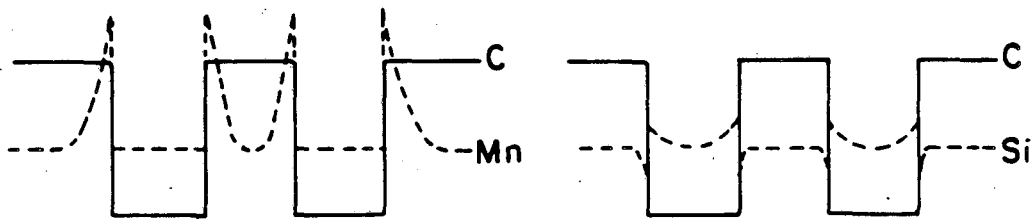
1. Nucleation of ferrite



2. Ferrite growth (I)



3. Ferrite growth (II)



4. Final equilibrium

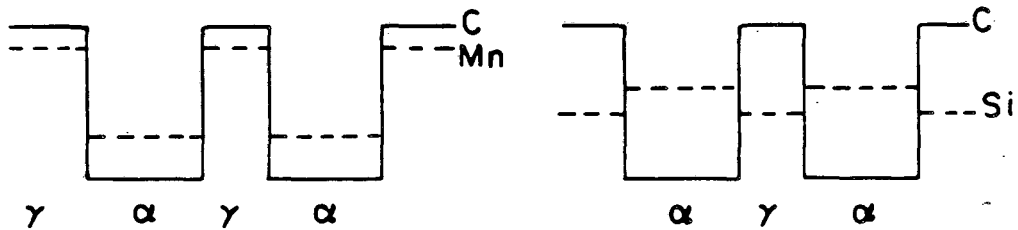


Fig. 54

XBL 8510-6717

This report was done with support from the Department of Energy. Any conclusions or opinions expressed in this report represent solely those of the author(s) and not necessarily those of The Regents of the University of California, the Lawrence Berkeley Laboratory or the Department of Energy.

Reference to a company or product name does not imply approval or recommendation of the product by the University of California or the U.S. Department of Energy to the exclusion of others that may be suitable.

*LAWRENCE BERKELEY LABORATORY
TECHNICAL INFORMATION DEPARTMENT
UNIVERSITY OF CALIFORNIA
BERKELEY, CALIFORNIA 94720*